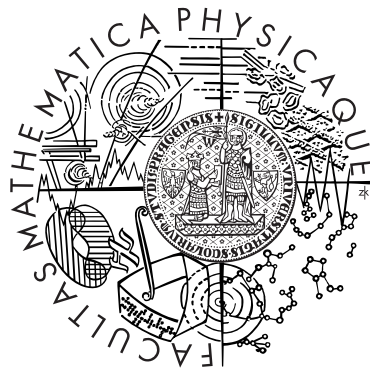Faculty of Mathematics and Physics
Charles University in Prague

Two dimensional spectropolarimetry of a sunspot

Jan Jurčák

Doctoral Thesis

June 2006

Two dimensional spectropolarimetry of a sunspot

Jan Jurčák

Astronomical Institute
Academy of Sciences of the Czech Republic
Ondřejov

Supervisor: RNDr. Michal Sobotka CSc.

Abstract

Spectropolarimetric observations of an irregular sunspot are analysed in this thesis. Two areas covering umbral cores, which are divided by light bridges and surrounded by a penumbra, were scanned in magnetically sensitive iron lines by the La Palma Stokes Polarimeter attached to the 0.5 m Swedish Vacuum Solar Telescope, configuration of instruments producing one of the best spectropolarimetric data available.

Stratifications of the temperature, magnetic field vector, and line-of-sight velocity are retrieved in the observed areas using the Stokes Inversion based on Response functions (SIR) technique, the inversion code developed at the Instituto de Astrofísica de Canarias.

The resulting values of these plasma parameters are in a good agreement with previous studies of photospheric layers of sunspots. The irregular umbras behave the same way as expected from the regular occurrences of these phenomena.

Although only parts of the penumbra were observed, the behaviour of the plasma quantities stratifications is found there in agreement with previous studies. Even better spatial resolution than in previous analyses is not sufficient to directly resolve the expected filamentary structure of the penumbra. Nonetheless, strong evidences for such configuration of the penumbra are presented supporting the theoretical simulations of the rising flux tubes by Schlichenmaier et al. (1998).

The light bridges are studied with advanced inversion technique (providing the stratifications of plasma quantities) for the first time. Known facts, like the decrease in magnetic field strength and the increase in inclination with respect to the surrounding umbrae, are confirmed along with a temperature increase in these structures. Moreover, the behaviour of these parameters with height indicate the presence of a canopy structure above the light bridges.

Acknowledgement

Contents

1 Introduction

Sunspots are the first known phenomena observed on the solar disc. If we do not consider the ancient observations, the sunspots were rediscovered by Galilei and others around the beginning of 17th century. From that time on, the sunspots were closely studied. The first important discovery about the nature of the sunspots was made by Wilson in 1769 who found that the visible radiation from the umbra and the penumbra emerges from a deeper layers than that from the quiet photosphere. At that times, it led to wrong conclusion that the central parts of the sun are dark and therefore cool. The fundamental discovery was made by Hale who measured a magnetic field in sunspots (Hale 1908). Since then, the magnetic field is considered to be the main cause of sunspot formation. Present knowledge about the sunspots is summarised in Sect. 2.

The instrumental equipment has been developing together with the understanding of sunspots phenomena. Starting with the naked-eye observations and ended nowadays with various satellite missions and ground telescopes observing in broad range of wavelengths. This thesis is based on data observed with the La Palma Stokes Polarimeter (LPSP) attached to the 0.5 m Swedish Vacuum Solar Telescope (SVST). This configuration of instruments produced one of the best spectropolarimetric data available nowadays, although similar data with higher spatial resolution should be available in near future through the Solar-B mission. This satellite will be launched in summer 2006 and will carry the 0.5 m optical telescope with the Focal Plane Package (FPP). One of the instruments included in the FPP will be the spectropolarimeter which will produce similar data sets as are analysed in this thesis. The observation and data reduction are described in Sect. 3.

All the information about the sunspot magnetic field, velocity, and temperature are retrieved from the radiation we receive from the sun. Over the time, various techniques have been used to estimate the magnitude of various plasma parameters. From the simplest estimation of line-of-sight velocity from the shift of the Stikes I profile, to one of the most advanced inversion codes: Stokes Inversion based on Response functions (SIR). The description of this inversion code is summarised in Sect. 4. The reliability of the inversion is also discussed in that section along with the examples of the response functions to various plasma parameters.

The results of the inversion are described in Sect. 5. The results are compared with previous studies of sunspots and some new conclusions are made.

2 Sunspots

The presence of intense magnetic field is the fundamental condition required for the formation of the umbra and the penumbra, two main components creating the sunspot. The convective motions, which heat the photospheric layers, are greatly reduced in the presence of the magnetic field and therefore the cool and dark area emerges on the solar surface.

The discovery of magnetic field in sunspots also explained the origin of the Wilson depression, or better to say, the depression of the unit continuum optical depth ($\tau = 1$) in sunspots. The depth, from which is the radiation coming, depends on the opacity of the photospheric layers. The main contribution to the opacity in the visible light is the H$^-$ bound-free opacity, which is proportional to the plasma temperature and gas pressure. The temperature is lower in the sunspots and accordingly is the opacity. As will be shown below, the gas pressure is smaller in the sunspots and the opacity of the plasma is thus further decreased.

The smaller value of the gas pressure in sunspots can be derived from the radial component of the magnetostatic force balance equation written in cylindrical coordinates (Solanki 2003)

$$\frac{\partial P}{\partial r} = \frac{B_z}{4\pi} \left(\frac{\partial B_r}{\partial z} - \frac{\partial B_z}{\partial r} \right),$$ (1)

where P is the gas pressure, r and z the radial and vertical coordinates, and B_r and B_z the corresponding components of the magnetic field strength. The difference between the gas pressure in the quiet sun ($P(R_s)$) and in the sunspot ($P(r)$) can be estimated from the integration of this equation

$$P(R_s) - P(r) = \frac{1}{8\pi} B_z^2(r) + \frac{1}{4\pi} \int_r^{R_s} B_z \frac{\partial B_r}{\partial z} dr = \frac{1}{8\pi} B_z^2(r) + F_c,$$ (2)

where F_c symbolises the radially integrated curvature forces. In the absence of these forces, it implies lower gas pressure in the sunspots due to the presence of magnetic pressure there.

The amplitude of the Wilson depression could be deduced using this force balance equation as was firstly proposed by Martínez Pillet & Vazquez (1993). However, they found out that the unknown curvature forces play as a big role as the gas pressure itself. This method could be used tenably only at restricted conditions which certainly do not hold in the irregular sunspot which is studied in this thesis. A full derivation of the pixel to pixel fluctuations of the local Wilson depression (an effect not considered in this thesis) must wait until a model with an assumed MHD configuration is constructed and the correct correspondence between optical depths and heights is made.

In next sections, the present knowledge of the magnetic field and of the velocity structure of sunspots is described. The nomenclature of the
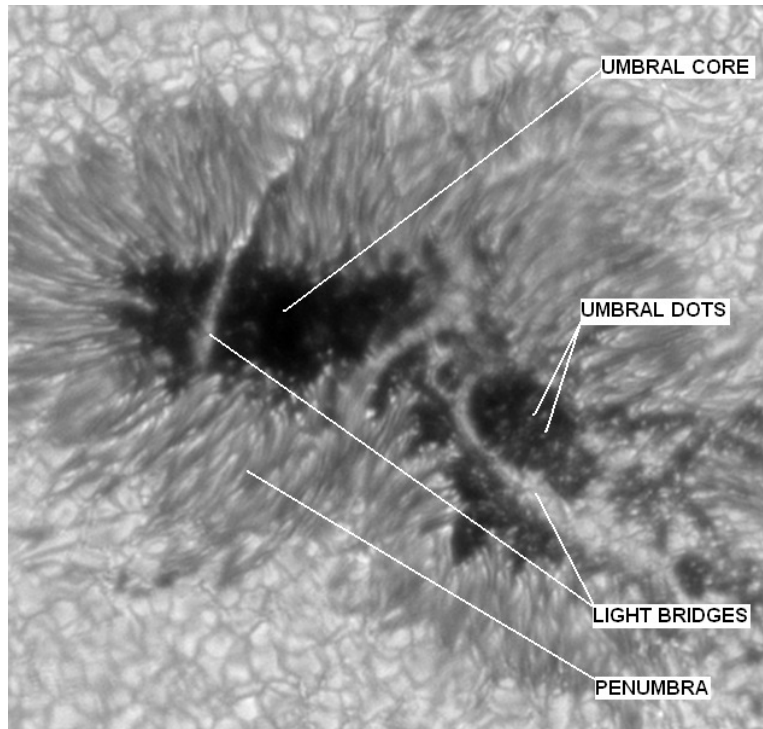
Figure 1: The basic nomenclature of the sunspot fine structure.

sunspot fine structure, which is commonly used is shortly described here (for detailed description see e.g. Sobotka 1997). In Fig. 1 the irregular sunspot analysed in this thesis is shown with the description of the fine structure. The penumbra is created from two components, dark and bright filaments. The fine structure can be usually found also in the umbra. The umbral dots are bright points visible there and the light bridges (LBs) are bright structures penetrating deep into the sunspot umbra or separating the umbra into the umbral cores.

In the following summary of the present knowledge of the sunspots, the thermal properties are not depicted. However, the thermal structure of the sunspot fine structure can be estimated from the continuum intensity, since the bright structures must have higher temperature at unit continuum optical depth. The review written by Solanki (2003) reports not only about the thermal structure of sunspots, but also describes in more details the present knowledge of sunspots.

2.1 Magnetic field of sunspots

The magnetic field of sunspots can be deduced from the Zeeman splitting of various lines. The field strength is largest near the geometrical centre of

the umbra reaching values up to 3700 G. This statement is true only in case of the regular sunspots, where the umbral centre corresponds also with the darkest part of the sunspot. Example of the magnetic field in an almost round sunspot is shown in Fig. 2. In Fig. 3, the average values of magnetic field strength and inclinations (from Fig. 2) are plotted as functions of the radial distance from the sunspot centre.

The magnetic field strength (Fig. 2 a, Fig. 3 left) is decreasing outward with no detectable jump on the umbral-penumbral boundary. The shape of the radial dependence of B has been studied by many authors, among others, Beckers & Schröter (1969) and Westendorp Plaza et al. (2001a). The shape is dependent on the sunspots size and regularity and also on the height in the atmosphere as is shown in Fig. 3 (left). The magnetic field inclination shows similar behaviour as the field strength, just in opposite sense, the field is vertical in the central parts of the umbra and almost horizontal on the outer boundary of the sunspot (Fig. 3 right).

From Figs. 2 and 3 is clear that the magnetic field continues beyond the white-light boundary of the sunspot. It forms a horizontal canopy and overlies the field-free plasma. The formation of the magnetic canopy is a result of the expansion with height of the magnetic flux tube which could be used as a simple model of regular round sunspots (see Sect. 2.3).

2.1.1 Penumbral fine structure

A simple model of the magnetic flux tube cannot be used to explain the fine structure of the magnetic field in the penumbra. The averaging process which was used to create Fig. 3 smoothed the inhomogeneities of the magnetic field strength and mainly of the inclination. The radial structures in the inclination map could be seen in Fig. 2 (b). Beckers & Schröter (1969) found differences between the inclination in bright and dark filaments. With increasing spatial resolution came other observations that support the rapid changes of inclination by 10–40° on arcsec and sub-arcsec scales (Lites et al. 1993; Title et al. 1993; Rimmele 1995a; Wiehr 2000; Westendorp Plaza et al. 2001a). The fluctuations of the magnetic field inclination is apparent, however, mentioned studies found various correlations between the inclination and brightness. Higher values of inclination in dark structures (more horizontal field there) have been found by Rimmele (1995a); Wiehr (2000); Westendorp Plaza et al. (2001a); Bellot Rubio et al. (2004) and Langhans et al. (2005). Sánchez Cuberes et al. (2005) also found similar dependence of inclination on the line-core intensity (i.e. steeper field in bright structures), but not on the continuum intensity. The positive correlation between the brightness and the inclination have been found by Title et al. (1993) and Stanchfield et al. (1997), although the dependence is very weak and the correlation coefficient does not exceed 0.2. Lites et al. (1993) determined higher inclination in bright filaments in the inner penumbra and weak corre-
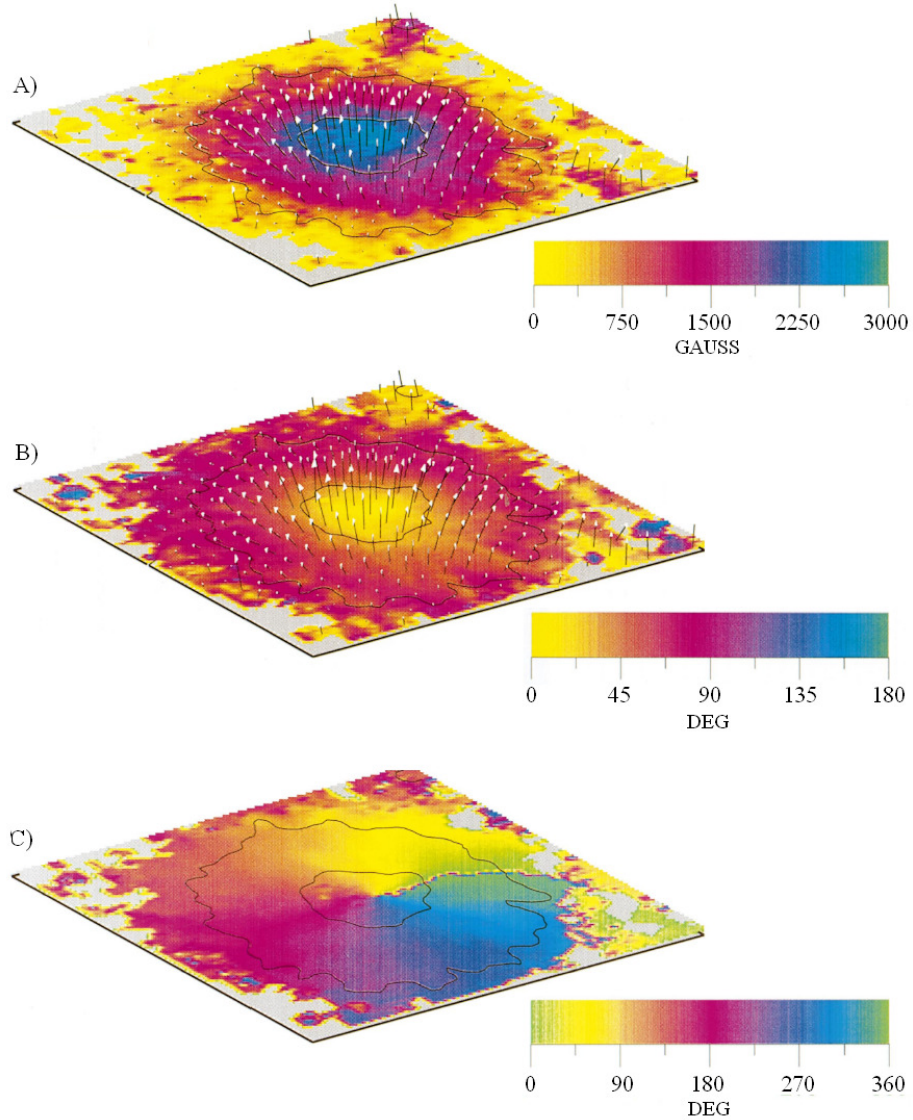
Figure 2: The magnetic properties of regular sunspot, the magnetic field strength (a), inclination (b), and azimuth (c). The arrows indicate the course of magnetic field vector and the length is proportional to its amplitude. Solid lines represent the umbra-penumbra and penumbra-quiet sun boundaries. Figures are taken from Westendorp Plaza et al. (2001a) by permission.

lation in the sense that inclination is higher in dark structures in the outer penumbra.

The situation becomes even more confusing if the dependence of the magnetic field strength on the continuum intensity or on the inclination is investigated. Some authors found no strong fluctuations in B either because of
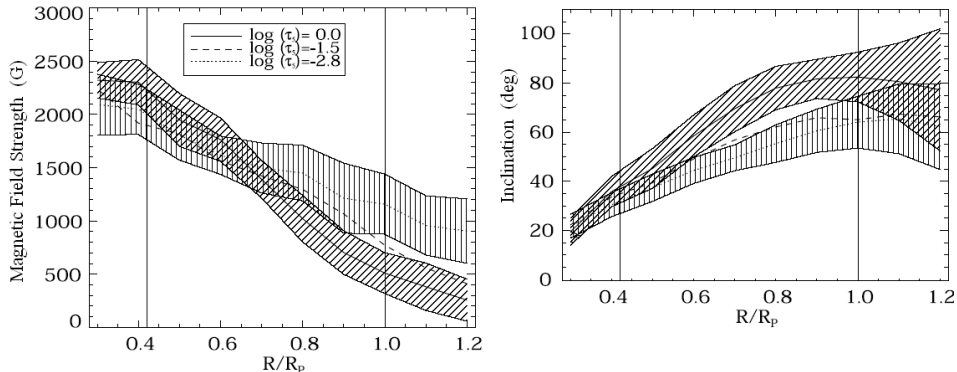
Figure 3: The azimuthal averages of magnetic field strength (left) and inclination (right) at three optical depths in the atmosphere at given distances from the sunspot centre. The vertical lines represent the umbral and penumbral boundaries. Shaded areas show the rms variations of the parameters at the upper and lower layers. Kindly provided by Westendorp Plaza (Westendorp Plaza et al. 2001a).

employed technique or because of insufficient spatial resolution (Lites et al. 1990; Schmidt et al. 1992; Rimmele 1995a). Title et al. (1993) observed the fluctuations in magnetic field strength, but interpreted them as fluctuations in inclination. Other authors found the fluctuations of magnetic field strength. Beckers & Schröter (1969) and Wiehr (2000) provide evidences for higher values of B in dark filaments. Westendorp Plaza et al. (2001a), however, argue for the opposite dependence, i.e. stronger field is associated with warmer gas. Sánchez Cuberes et al. (2005) found stronger magnetic field in bright structures in the line-core intensity but not in the continuum intensity.

Regarding to the connection between the inclination and the magnetic field strength, Lites et al. (1993) and Stanchfield et al. (1997) found that the less inclined field (with respect to the local vertical) is slightly stronger (by 100–200 G). The possible complexity of the problem is shown in Fig. 4, where the dependence of the correlation coefficient between the magnetic field strength and inclination on the depth in the atmosphere and on the position in the penumbra is plotted.

Langhans et al. (2005) described penumbra as consisting of two components. They found more vertical and stronger magnetic field in bright filaments, where the difference in strength of the magnetogram signal appears to peak in middle penumbra and decrease toward the outer penumbral boundary. The most advanced two magnetic components inversion of penumbral profiles has been made by Bellot Rubio et al. (2004). They separate the penumbra into two components, the background field interlaced with the system of more inclined flux tubes. They found that the magnetic field of

15
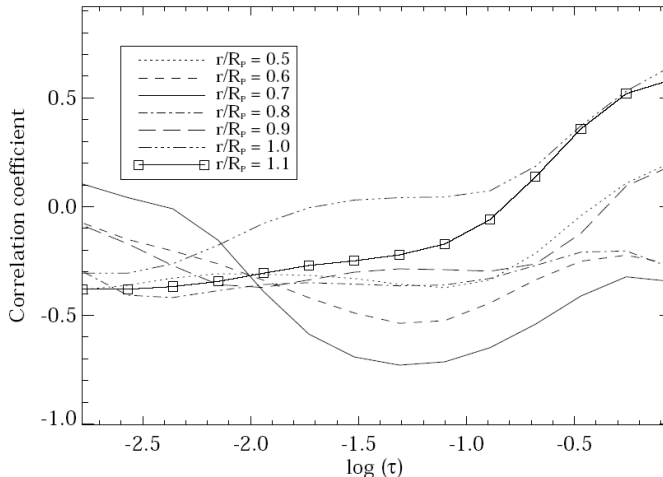
Figure 4: Variation of the correlation coefficient between the magnetic field strength and inclination with the depth in the atmosphere and for different azimuthal paths. Kindly provided by Westendorp Plaza (Westendorp Plaza et al. 2001a).

the background component remains relatively vertical all the way from the inner to outer penumbra with maximum inclination about 60°. The inclination of the magnetic field in the flux tubes changes from 70° near the umbra to 100° on the outer penumbral boundary, i.e. the tubes go upward in the inner penumbra, become horizontal and finally dive. Borrero et al. (2004) found similar results even from the one-component inversion. See this work for comparison between the one- and two-component inversion of the penumbral photosphere. This configuration of the penumbra magnetic field is called uncombed structure. See Sect. 2.3 for proposed physical models producing this magnetic field configuration and empirical argumentation in favour of this uncombed structure.

2.1.2 Umbral fine structure

The observations of umbral dots suggest that the magnetic field strength is weaker there. The lowest magnetic field was found by Beckers & Schröter (1968) reaching 10% of B in the surrounding umbra and having opposite polarity. However, Wittmann (1971) argued that Beckers & Schröter (1968) misinterpreted magnetooptical effects as the umbral dot contribution. Various values of the magnetic field decrease have been found by other authors depending on the used lines and position of the dot in the umbra, ranging from 50% of the umbral field strength up to no reduction of B (Kneer 1973; Buurman 1973; Pahlke & Wiehr 1990; Schmidt & Balthasar 1994; Tritschler & Schmidt 1997; Socas-Navarro et al. 2004). Schmidt & Balthasar (1994)

16

point out that the small reduction of the magnetic field strength can be just an apparent decrease, because magnetic field strength is decreasing with height and bright (and therefore hot) umbral dots emitted the radiation from higher layers than the surrounding umbra (due to the temperature dependence of the opacity). See the review by Sobotka (2003) and references therein for the problem of magnetic "invisibility" of umbral dots. The stratification of the magnetic field strength found by Socas-Navarro et al. (2004) suggests the canopy structure above the field free material which may be the cause of the umbral dots. See Sect. 2.3 for more details about the possible origin of umbral dots.

Previous papers report about weaker magnetic field in light bridges and also about higher values of inclination there. The decrease of the magnetic field strength and the change of inclination is dependent on the width of a light bridge, i.e. Beckers & Schröter (1969) found the decrease of 300 G in the weak light bridge and an increase in inclination around 5°. Rüedi et al. (1995) found a difference of B between the light bridge and the surrounding umbra around 1000 G and maximum difference of inclination around 70° in the LB centre. Leka (1997) found a range of decreases in the magnetic field strength from 300 G to over 1200 G and increased inclination by at least 10° in 11 different light bridges studied in her paper.

2.2 Velocity field of sunspots

The velocity structure of sunspots is somehow similar to the magnetic field structure. The umbra is very easy to describe on the contrary to penumbra which is much more complicated.

The umbra exhibits steady and strong magnetic field in which the plasma is frozen. Therefore no significant motions are observed in the unperturbed umbra. The umbra is usually used as a zero reference point (see Rimmele 1995b, and references therein) if no quiet region of solar photosphere or no distinct terrestrial atmospheric lines could be used for this purpose.

The dominant signature of the dynamical behaviour of the penumbra is the Evershed effect named after its discoverer (Evershed 1909). The Evershed effect consists of a blueshift of the photospheric spectral lines in the discward part of the penumbra and a corresponding redshift in the limbward part of the penumbra (Dere et al. 1990; Rimmele 1994, 1995b; Schmidt & Schlichenmaier 2000; Westendorp Plaza et al. 2001b; Bello González et al. 2005). Such orientation of the flow is valid at the photospheric layers, the flow of an opposite orientation with larger velocities is observed in the chromosphere. The magnitude of the velocity increases from the inner parts of the penumbra to its outer edge, where it stops abruptly according to e.g. Wiehr et al. (1986) and Title et al. (1993). On the other hand, Börner & Kneer (1992); Rimmele (1994) and Rimmele (1995b) found evidences for Evershed velocities extending beyond the white-light boundary of the sunspot.

17
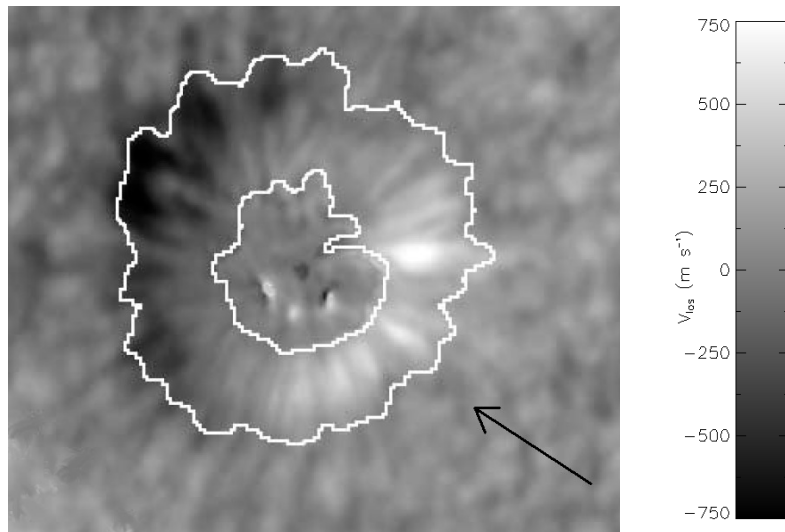
Figure 5: Time-averaged Doppler velocity image of a regular sunspot (from Georgakilas & Christopoulou (2003)). The umbral and penumbral boundaries are marked by the white lines and the arrow points to the disc centre.

An example of the Evershed flow in the regular sunspot is shown in Fig. 5, where almost no velocities are recognisable in directions perpendicular to the centre-limb direction. This suggests that the flow is nearly horizontal in the photosphere with inclination (defined with respect to the local vertical) larger than $80°$ (Dere et al. 1990; Börner & Kneer 1992; Schlichenmaier & Schmidt 2000). This is unexpected since the plasma flow should follow the orientation of the magnetic field vector which is more vertical in the penumbra (see Sect. 2.1). This discrepancy can be explained by the uncombed structure of the magnetic field, which is described in Sect. 2.1 and is theoretically depicted in Sect. 2.3.

2.2.1 Penumbral fine structure

Rimmele (1995b); Schlichenmaier & Schmidt (2000); Schmidt & Schlichenmaier (2000) and Tritschler et al. (2004) found upflows 300–600 m s^{-1} in the inner penumbra and downflows of about 200–400 m s^{-1} in the outer penumbra. On the contrary, Shine et al. (1994) deduced small upflows (200–400 m s^{-1}) near the outer penumbral boundary. Such small values of the vertical velocities could be heavily influenced by the error in the zero-level velocity, which is typically uncertain by 200 m s^{-1} or even more.

As is said above the plasma flow should follow the orientation of the magnetic field vector, therefore the observations of Rimmele (1995b); Schlichenmaier & Schmidt (2000); Schmidt & Schlichenmaier (2000) and Hirzberger et al. (2005) confirm the shape of the magnetic flux tubes derived by Bellot

Rubio et al. (2004) from the two-component inversion of the penumbral profiles. Bellot Rubio et al. (2004); Borrero et al. (2004) and Langhans et al. (2005) also found that the Evershed flow is connected with the horizontal flux tubes with lower magnetic field strength.

If the Evershed effect is really restricted to horizontal flux tubes, than rapid change of velocity must be seen on small scales. Observations which confirm this expectation were studied by many authors (Beckers & Schröter 1969; Wiehr et al. 1984; Title et al. 1993; Shine et al. 1994; Rimmele 1995a; Westendorp Plaza et al. 2001b; Langhans et al. 2005). They found a correlation between the velocity of the Evershed flow and the dark filaments. However, there are some studies that have not found any significant correlation between the brightness and the flow velocity (e.g. Lites et al. 1990). On the other hand, Hirzberger et al. (2005) found the correlation between the flow channels and the bright penumbral filaments. The results are not dependent only on the technique which is used for the derivation of the line-of-sight velocities, but mainly on the absorption lines which are used. For example, the velocity measured in the line cores (highest layers of the atmosphere) correlate with the intensity fluctuations measured in the line core, but not with the continuum intensity.

2.2.2   Umbral fine structure

The measurements of velocity fields in the umbral dots is problematic, since these structures are on the resolution limit of the current spectrographs. The umbral dots are either at rest or exhibit small upflows up to 400 m s^{-1} with respect to the surrounding umbra (Lites et al. 1991; Rimmele 1997; Tritschler et al. 2004). Faster upflows were reported by Rimmele (2004) (1 km s^{-1}), although Socas-Navarro et al. (2004) infirm this result. Recent study by Socas-Navarro et al. (2004) found very small upflows in several umbral dots from 0 to 200 m s^{-1} with typical uncertainties around 100 m s^{-1}.

Concerning the light bridges, there are no systematic findings. Beckers & Schröter (1969) found blueshifts with respect to the umbral velocities, Rüedi et al. (1995) found redshifts, and Leka (1997) found either blueshifts or redshifts in the light bridges studied in her paper. Convective elements similar to the granulation with upflows in bright granules and downflows in dark lanes are observed in granular light bridges (Rimmele 1997). In comparison with photospheric granulation, cell sizes and velocities of light bridge granulation are smaller and lifetimes longer, which may be a consequence of remaining weak magnetic field. Observations of evolution and horizontal motions of bright granules in light bridges also indicate the existence of convective motions (Hirzberger et al. 2002).

2.3 Models

This work is based on the analysis of observations and no computation of sunspot models are made here. The short description of various models presented here serves only as a comparison for observational results. See Solanki (2003) and references therein for detailed description of theoretical sunspot models.

2.3.1 Global sunspot models

As was already said, sunspots are thought to be vertical flux tubes intersecting the solar surface. Such models, aim of which is to reproduce the global properties of sunspots, are computed in the magnetohydrostatic approximation. Such assumption is satisfactory for the overall structure of the magnetic field since the changes in mature sunspots are slow (see Jahn 1997, for further arguments in favour of the static description).

The global models of sunspots differ in one basic assumption, if the sunspot is monolithic below the solar surface (Cowling 1957) or if it breaks up into many small flux tubes (cluster or so-called spaghetti model, Parker 1975). The solar layers below the unit continuum optical depth cannot be directly observed, but the investigations using the technique of local helioseismology favour a cluster model (Chen et al. 1997; Zhao et al. 2001). The complex fine structure of the penumbra also suggest that the magnetic field is concentrated into many small flux tubes. Arguments for the cluster model are presented by Choudhuri (1992) and arguments in favour of the monolithic model come from Spruit (1981).

The first quantitative model of sunspot magnetic field was introduced by Schlüter & Temesváry (1958) who prescribed the radial dependence of the magnetic field vector at given geometrical height and assumed it to be the same at all heights, except for a scaling to describe the expansion of the field lines with height (therefore it is also called self-similar model). This allows to separate the vertical and radial components of the magnetic field strength and only an ordinary differential equation for $B_0(z)$ needs to be solved. The results are dependent on the particular choice of so-called shape function $f(r/R(z))$, which is usually considered to be a Gaussian shape function. This model was very successful in reproducing the observed distribution of the magnetic field strength and therefore studied by many authors. Disadvantage of this kind of models is the problem with reproducing the continuum intensity. These models usually create a bright ring on the umbra-penumbra boundary, which intensity may be influenced by the choice of the shape function (see Murphy 1990). Other limitations of self-similar models are discussed by Steiner et al. (1986).

Osherovich (1982) included to the self-similar models the field lines that return to the solar surface just outside the visible sunspot. However, this

model is not supported by the observations, the return flux in the close surrounding of sunspots is small (Solanki et al. 1992; Lites et al. 1993) and recent studies suggest not negligible amount of return flux in the penumbra itself (Westendorp Plaza et al. 2001a; Bellot Rubio et al. 2004; Borrero et al. 2004). The continuum intensity predicted by the return flux models is not much better than that predicted by the standard self-similar models. Only by reducing the Wilson depression to improbable low value of 250 km, Murphy (1990) derived the continuum intensity qualitatively comparable with the observations at the disc centre, near the limb the unrealistic bright rings appeared nevertheless.

Other group of models is based on the simplification of the force balance equation. If the terms describing the influence of the gas and gravity are neglected, the force balance equation reduces to

$$\nabla \times \mathbf{B} = \alpha \mathbf{B}. \tag{3}$$

A potential field is obtained if the force-free parameter α is set to zero. The problem is that the purely potential field predict no natural boundary of the sunspots and must be artificially bounded by the magnetopause. The pressure difference $\triangle p$ and its derivative must be matched to the external atmosphere at the magnetopause. Such model was computed by Simon & Weiss (1970) for the first time. Their results could give a suitable description of magnetic field in pores, but are not able to simulate the magnetic field of the sunspots.

The first force-free model was computed by Schatzmann (1965) who used constant α. The solution approximately described the radial dependence of magnetic field strength, indicating that the constant value of α is sufficient for the modelling of the visible layers of simple sunspots (Martens et al. 1996). This model was used by Martens et al. (1996) who added terms describing the flutedness (the small-scale structure of the penumbra). Similar approach has been applied by Neukirch & Martens (1998). The results obtained with these models reproduce the observations of Beckers & Schröter (1969) and Title et al. (1993), but need to be compared with observations of broad-band circular polarisation, because such observations contain information on the vertical structure of flutted fields (Sanchez Almeida & Lites 1992; Solanki & Montavon 1993; Martínez Pillet 2000).

Pizzo (1986) computed set of two-dimensional models, where the hydrostatic equilibrium is hold along each field line. Such models are more advanced than the self-similar or return-flux models and the results come closer to the observations. For example, the continuum intensity distribution is well described by this model. However, the presence of magnetic boundary suggested by the observations (Beckers & Schröter 1969; Solanki & Schmidt 1993) is not confirmed by this model.

Simon & Weiss (1970) used for the first time the model bounded by the current sheet at the magnetopause. The shape of the magnetopause they

used was just an approximate solution of the free boundary problem which was generally solved by Wegmann (1981). This solution was applied by Schmidt & Wegmann (1983) to the sunspots, in this case the current sheet bounded a potential field. This model does not describe the presence of the penumbra. Jahn (1989) includes the body currents to the area corresponding to the penumbra. Combined current sheet and body current models give results similar to the distribution of magnetic field observed in sunspots. The inclination angles predicted by this model are in a good agreement with the measurements analysed by Bellot Rubio et al. (2004). However, the thermal structure has no distinct difference between the umbra and the penumbra. Therefore, Jahn & Schmidt (1994) simplified the previous model and replaced the body currents by the second current sheet on the umbra-penumbra boundary. The resulting thermal structure is more realistic, but the disadvantage is the emergence of the jump in the magnetic field strength at the umbra-penumbra boundary. Such jump is in discrepancy with the observations.

2.3.2 Penumbral models

The complex fine structure observed in the penumbra by many authors (e.g. Beckers & Schröter 1969; Lites et al. 1993; Title et al. 1993; Rimmele 1995a; Wiehr 2000; Westendorp Plaza et al. 2001a; Bellot Rubio et al. 2004; Borrero et al. 2004; Langhans et al. 2005) requires more detailed models than those presented in the previous section.

At first, the empirical model introduced by Solanki & Montavon (1993) and developed by Martínez Pillet (2000) is described. They constructed uncombed structure in the penumbra from the horizontal flux tubes embedded in a more vertical background field. Such configuration of the penumbral magnetic field was suggested to explain the observed net circular polarisation. The Evershed flow is carried mainly by the horizontal flux tubes in this empirical model, but some flow must be also carried by the background field. Otherwise the centre- and limb-side net circular polarisation curves would be the same but with different signs, what is in discrepancy with the observations (Martínez Pillet 2000). Recent analysis of observations found evidences for such configuration of the magnetic field (Bellot Rubio et al. 2004; Borrero et al. 2004; Langhans et al. 2005).

Jahn (1992) proposed that the complex magnetic fine structure of the penumbra is caused by the convective exchange of the flux tubes. There exist two physical scenarios which suggest the possible origin of the convective motions in the penumbra.

First, a flux tube is initially positioned at the penumbra–quiet sun boundary. It is heated by the field-free convection and rises developing a flow along the tube that points upward beneath the photosphere and outward above the photosphere. The part of the flux tube emerging above

the surface is filled with hot gas and therefore appears bright. The intersection of the flux tube and the photosphere is moving towards the umbra and could be interpreted as the penumbral grain which could also move in this direction (Sobotka et al. 1999). The part of the flux tube above the surface cools down by radiative losses and becomes more horizontal and the outward flow resembles the observed Evershed effect. Up to this point, the scenario has been confirmed by the two-dimensional simulations made by Schlichenmaier et al. (1998). The loss of buoyancy and the expected dive of the flux tube has not been produced by the simulations. In this scenario, the flux tube is embedded in the background field taken from the model by Jahn & Schmidt (1994). This background field is in rest and according to Martínez Pillet (2000) such configuration could not properly explain the discrepancy between the shape of the centre- and limb-side net circular polarisation curves.

Second scenario has been suggested by Wentzel (1992). He starts with the homogeneous inclined field. By producing a density inversion he causes the flux tube to fall and become horizontal over most of the penumbra. Higher density in the fallen flux tube causes a horizontal outflow that resembles the Evershed effect. However, this scenario has not yet been studied in detailed numerical simulation.

The first mechanism which was suggested to explain the penumbral velocity field is called the siphon flow model by Meyer & Schmidt (1968). The authors considered an existence of a flux tube which footpoints have different field strength. If the first footpoint is located in the penumbra and the second in area with stronger magnetic field strength (e.g. umbra of another spot), than due to horizontal pressure balance the flow is started and kept by the imbalance in the gas pressure. Such model could also explain the inverse Evershed effect at higher layers of the atmosphere. However, the length of the loops produced by the siphon flow model is too short compared to the size of the penumbra. The longest tubes could not exceed roughly 3000 km (Degenhardt 1991) which is still less then the width of a large penumbra. The recent observations show downflows in the outer part of the penumbra (Bellot Rubio et al. 2004; Borrero et al. 2004; Langhans et al. 2005), it would mean that both footpoints supporting the siphon flow are located in the penumbra. Since the field strength is decreasing outwards, the flow should be directed towards the umbra as implies the pressure balance argument. If the Evershed flow is really driven by the siphon flow then it is probable that the pressure difference between the footpoints is not caused by the difference in the magnetic field strength, but through the temperature and density difference, as in the model by Schlichenmaier et al. (1998).

2.3.3 Umbral dots models

The explanation of the existence of umbral dots depends on the considered global model of the flux tube, i.e. if the monolithic or cluster model is considered. The model by Wentzel (1992), which was suggested to explain the formation of the uncombed structure of the penumbra, could also explain the presence of the umbral dots and is not dependent on the subsurface structure of the sunspot.

Weiss et al. (1990) simulated the umbral dots as tops of the magneto-convective structures inside the monolithic magnetic flux tubes. The umbral dots suggested by this model have weaker magnetic field and show upflow motions. Such behaviour is really observed in umbral dots, but is also predicted by models based on the cluster configuration.

In the spaghetti model, the umbral dots are considered to be intrusions of field-free gas rising and pushing numerous thin flux tubes aside (Parker 1979; Choudhuri 1986). With amount of rose materials rises also the pressure from above which should close the protrusion of hot gas. Choudhuri (1986) derived that at the continuum layer the field-free area should be detectable, but 200 km above that level the field is practically homogeneous again (Degenhardt & Lites 1993a,b). The spatial resolution of the spectropolarimetric measurements is not sufficient to found the field-free area, but see Socas-Navarro et al. (2004) for observational arguments in favour of this configuration.

The only known semi-empirical models of the light bridges were proposed by Sobotka (1989), who derived lower temperature in the light bridges compared to the mean penumbral model by Kjeldseth-Moe & Maltby (1969). In the article by Spruit & Scharmer (2006), the authors proposed the explanation of the fine structure of the penumbra as the field-free gaps and interpreted light bridges as wider representation of the same effect. They also refer to the 3D radiative magnetohydrodynamic simulation of the light bridge computed by Nordlund & Stein (2005), which are not yet published.

3   Observations and data reduction

On May 13, 2000 two areas in an irregular sunspot in an active region NOAA 8990 were observed with the La Palma Stokes Polarimeter (LPSP, Martínez Pillet et al. 1999) attached to the spectrograph of the 0.5 m Swedish Vacuum Solar Telescope (SVST) (Scharmer et al. 1985). The SVST was operated on the island of La Palma by the Institute for Solar Physics of the Royal Swedish Academy of Sciences in the Spanish Observatorio del Roque de los Muchachos of the Instituto de Astrofísica de Canarias. The diffraction resolution limit of the telescope was $0.32''$ at $\lambda = 630$ nm and $0.25''$ at $\lambda = 500$ nm. The data analysed in this thesis were obtained by Valentin Martínez Pillet and Michal Sobotka.

The optical scheme of LPSP attached to SVST is shown in Fig. 6. The linear polariser (TCsC) and the instrumental polarisation unit (ICsC) are components serving for the instrumental calibration. The important parts of the Analyser sub-System (AsS) are two ferroelectric liquid crystals (FLCs). The orientation of the optical axis in FLC has two possibilities and changes in response to the voltage ramps. Two FLCs with two possible orientations of optical axes produced four modulation states (each with different linear combinations of the Stokes parameters) with polarisation efficiencies (see Martínez Pillet et al. 2001) of $\epsilon_Q = 0.38$, $\epsilon_U = 0.41$, and $\epsilon_V = 0.57$. For each slit position, 20 accumulations with 33.3 ms exposure time for each of
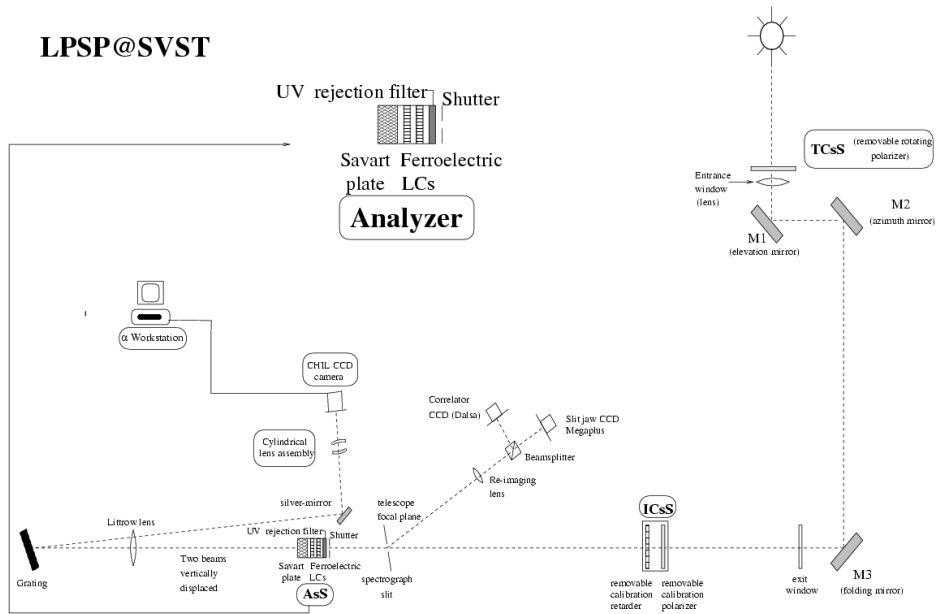

Figure 6: The optical layout of the La Palma Stokes Polarimeter attached to the Swedish Vacuum Solar Telescope. Kindly provided by Martínez Pillet.
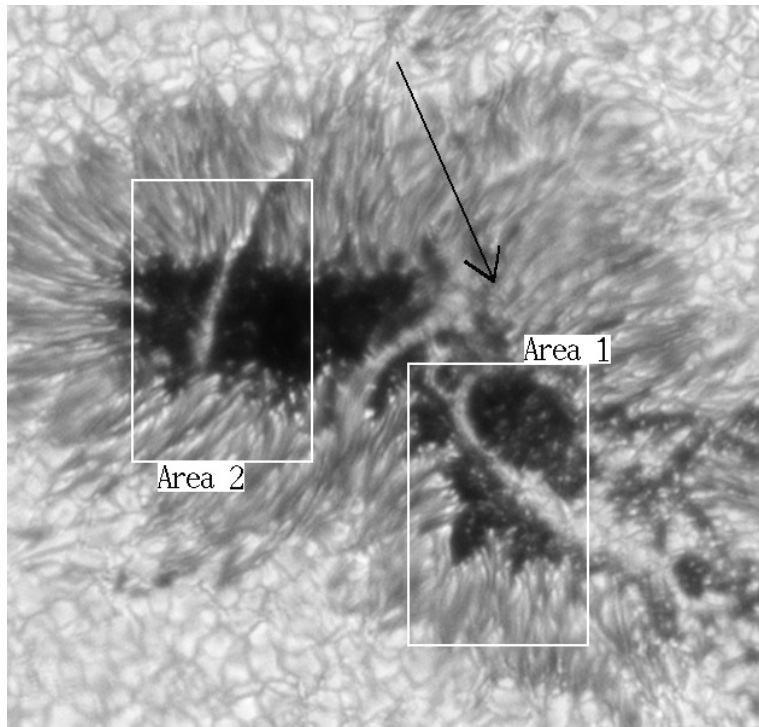
Figure 7: White-light image of the leading sunspot in NOAA 8990 with marked areas under study. The arrow points to the north direction.

the four modulation states were taken to increase the signal-to-noise ratio. This setting gives 3 s exposure time for one position of the spectrograph slit with S/N ratio of the reduced data equal to 600 for the linear polarisation profiles (Q, U) and 800 for the circular polarisation profile (V). The telescope instrumental polarisation is fully accounted for, as explained by Martínez Pillet et al. (2001).

As mentioned above, the object of the observations was an irregular leading sunspot in active region NOOA 8990. The spot was located near the disc centre, at heliocentric position 14° N and 17° W (heliocentric angle $\mu = 0.907$). One of the white-light images recorded simultaneously with the spectral scans is shown in Fig. 7. Two areas marked in the figure were scanned in the magnetically sensitive lines Fe I 630.15 nm (Landé factor $g = 1.67$) and Fe I 630.25 nm ($g = 2.5$). The scans were taken at 9:03 and 9:13 UT for the first and second area respectively.

The pixel size of the white-light imaging camera working at $\lambda = 525$ nm was $0.083''$, the resulting resolution including the seeing was around $0.3''$, and the exposure time was 11 ms. The pixel size of the spectropolarimetric camera was $0.078''$. The width of the spectrograph slit was equivalent to $0.32''$ and the scanning step was $0.24''$. The resulting spatial resolution,

including the effect of the seeing, is about $0.7''$ for the spectropolarimetric observations.

The resulting field of view (one area approximately of $13'' \times 19''$) was composed of 80 slit positions in steps of $0.24''$. The steps were made by the tip–tilt mirror that was always in closed loop with the sunspot-tracker camera during these two scans.

Flat-fields were created separately for each polarisation modulation state because they display different interference patterns. The flat-field data are used to derive the line curvature produced by the spectrograph and passed to the real data for its correction. After the dark-field subtraction, the flat-field division, and the line curvature correction, the data are demodulated with a matrix inferred from the polarisation calibration optics used by the polarimeter. Finally, the Mueller matrix is corrected with the convention of positive Q orientated parallel to the solar rotation axis. Data reduction ends with an ad-hoc correction for crosstalk with intensity that forces the continuum portions of Stokes Q, U and V to zero. The data preprocessing was made by Valentín Martínez Pillet.

Regarding the white-light image in Fig. 7, the nomenclature of various parts of studied areas, which is used in next sections, is clarified here. The area 1 and area 2 are also called first and second area respectively. Umbra in the first area can be called first umbra, similarly the second umbra is the umbra in the area 2 and accordingly are called the penumbras. The light bridges in the areas are called first and second light bridge, abbreviations are LB1 and LB2 respectively.

4 Inversion code

The inversion code SIR (Stokes Inversion based on Response functions) is used to analyse the observed data. The SIR code was developed at the Instituto de Astrofísica de Canarias (Ruiz Cobo & del Toro Iniesta 1992). It is a one-dimensional inversion code working under the assumption of local thermodynamic equilibrium (LTE) and hydrostatic equilibrium. Other limitations and assumptions are described in the article by Bellot Rubio (1999) which was written as a user guide to this inversion code. See also the survey studies by Ruiz Cobo (1998) and Westendorp Plaza et al. (2001a,b).

The inversion code returns the stratification of temperature (T), magnetic field strength (B), inclination (γ_{LOS}), azimuth (ψ_{LOS}), and line-of-sight velocity (v_{LOS}). More about the input and output parameters is written in Sect. 4.4.

4.1 Theoretical background

SIR is using the radiative transfer equation (RTE) for polarised light in the line-forming region (see del Toro Iniesta 2003)

$$\frac{d\mathbf{I}}{d\tau} = \mathbf{K}(\mathbf{I} - \mathbf{S}), \tag{4}$$

where $\mathbf{I}$ samples the Stokes profiles I, Q, U, and V, $\mathbf{K}$ is the propagation matrix (including the absorption and dispersion components), and $\mathbf{S}$ is the source function vector. In our simplified case (LTE assumed), the source function is not equal to zero only for the Stokes I profile and is dependent only on the temperature T, thus $\mathbf{S} = (B_\nu(T), 0, 0, 0)$, where $B_\nu(T)$ is the Planck's function. The formal solution of RTE can be written as

$$\mathbf{I}(0) = \int_0^\infty \mathbf{O}(0, \tau)\mathbf{K}(\tau)\mathbf{S}(\tau)d\tau, \tag{5}$$

where $\mathbf{I}(0)$ is the intensity at the surface of the atmosphere and $\mathbf{O}(0, \tau)$ is the evolution operator (Landi Degl'Innocenti & Landi Degl'Innocenti 1985; del Toro Iniesta 2003).

4.1.1 Response functions

The emerging intensity and shape of the Stokes profiles $\mathbf{I}(0)$ depend on the initial model of the atmosphere $\vec{x}$. A small change of the initial plasma parameters $\delta\vec{x}(\tau)$ (e.g. temperature, velocity, magnetic field strength or orientation) at the optical depth τ causes the change of the propagation matrix and the source function. At first approximation, these changes can be written as

$$\delta\mathbf{K}(\tau) = \sum_{i=1}^m \frac{\partial\mathbf{K}}{\partial x_i}\delta x_i(\tau) \qquad \text{and} \qquad \delta\mathbf{S}(\tau) = \sum_{i=1}^m \frac{\partial\mathbf{S}}{\partial x_i}\delta x_i(\tau), \tag{6}$$

where m is the total number of the parameters. The associated changes in intensities follow the transfer equation formally identical to RTE (4)

$$\frac{d\delta\mathbf{I}}{\delta\tau} = \mathbf{K}(\delta\mathbf{I} - \delta\mathbf{S}) + \delta\mathbf{K}(\mathbf{I} - \mathbf{S}), \tag{7}$$

where the second order terms are neglected. Following the analogy, the emergent change of intensity is

$$\delta\mathbf{I}(0) = \int_0^\infty \mathbf{O}(0,\tau)\left[\mathbf{K}(\tau)\delta\mathbf{S}(\tau) - \delta\mathbf{K}(\tau)(\mathbf{I} - \mathbf{S})\right]d\tau. \tag{8}$$

Taking into account the equations (6), the response function (RF) of the parameter i is defined as

$$\mathbf{R}_i(\tau) = \mathbf{O}(0,\tau)\left[\mathbf{K}(\tau)\frac{\partial\mathbf{S}(\tau)}{\partial x_i} - \frac{\partial\mathbf{K}(\tau)}{\partial x_i}[\mathbf{I}(\tau) - \mathbf{S}(\tau)]\right] \tag{9}$$

and the equation (8) can be rewritten as

$$\delta\mathbf{I}(0) = \sum_{i=1}^m \int_0^\infty \mathbf{R}_i(\tau)\delta x_i(\tau)d\tau. \tag{10}$$

See Ruiz Cobo & del Toro Iniesta (1992, 1994) or del Toro Iniesta (2003) for detailed derivation. The inversion code is named after these functions, because their role is crucial as is shown in the next section.

4.1.2 The inversion process

The scheme of the inversion process in case of a one-component model atmosphere is shown in Fig. 8. In the following paragraphs, the inversion process is described according to this scheme.

The emergent Stokes spectrum is derived from the equation (5) using the initial model of atmosphere, the atomic parameters, and the abundances given in the input files. The synthetic profile $\mathbf{I}$ is then convolved with the gaussian profile, which simulates the effect of the macroturbulence (Bellot Rubio 1999), and with the instrumental profile, if this one is known (MAC and IPS in Fig. 8). Obtained synthetic spectrum ($\mathbf{I}^*$) is then mixed with the stray-light profile ($\mathbf{I}^{str}$) given by the user. The portion of the stray light is given by the parameter s (stray-light factor), which value is fitted during the inversion. Resulting synthetic spectrum $\mathbf{I}^{syn}$ is then compared with the observed spectrum ($\mathbf{I}^{obs}$) and the merit function (χ^2) is computed.

$$\chi^2(\vec{x}) \propto \sum_{k=1}^4 \sum_{j=1}^n [I_k^{obs}(\lambda_j) - I_k^{syn}(\lambda_j, \vec{x})]^2, \tag{11}$$
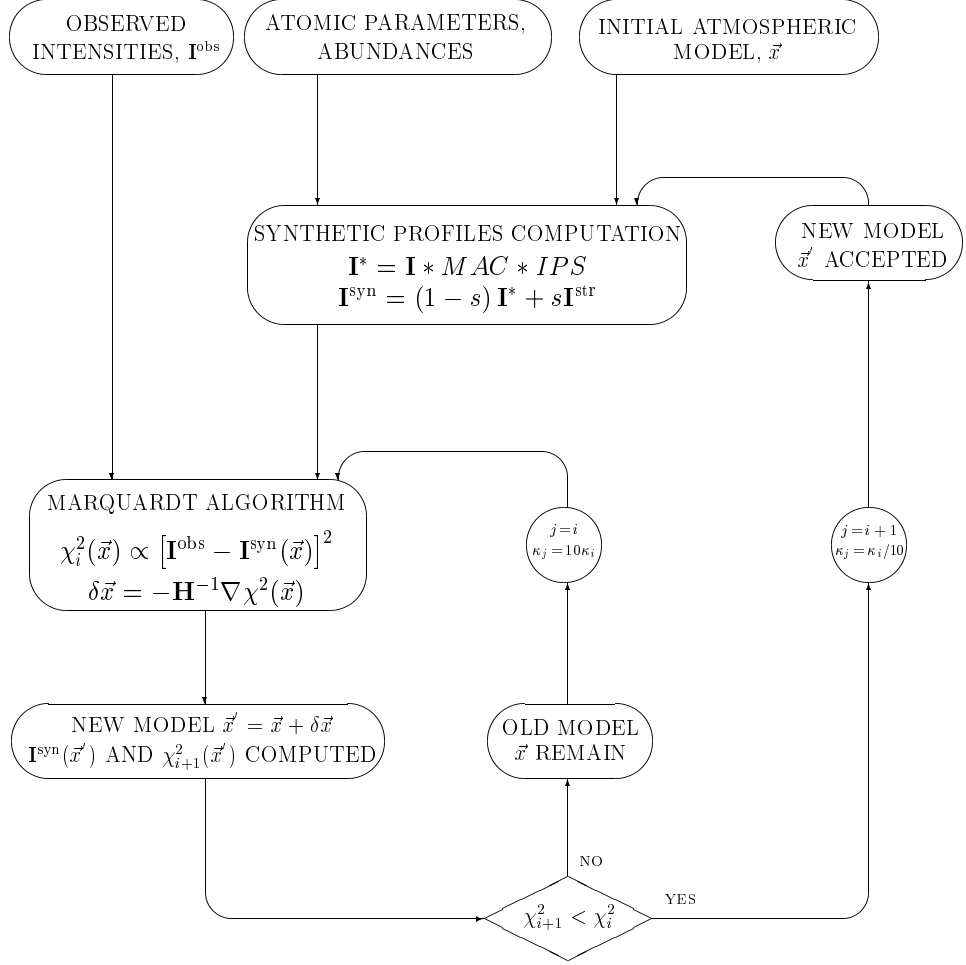
Figure 8: The scheme of the inversion process. Adapted from Koza (2003).

where k samples the 4-component vector of Stokes profiles and n is the total number of wavelength points (λ_j).

The goal of the inversion code is to minimise the merit function, therefore we need to change the initial model of the atmosphere $\vec{x}$ by $\delta\vec{x}$ to move in the space of the free atmospheric parameters closer to the global minimum. Close to the minimum, the merit function of the new model can be approximated by the Taylor series of the old merit function, so that

$$\chi^2(\vec{x} + \delta\vec{x}) \simeq \chi^2(\vec{x}) + \delta\vec{x}(\nabla\chi^2 + \mathbf{H}\delta\vec{x}), \tag{12}$$

where $\nabla\chi^2$ represents the partial derivative of the merit function and $\mathbf{H}$ is a so-called curvature matrix. It is one half of the Hessian matrix containing the second partial derivatives of the merit function ($H_{ij} = 1/2 \; \partial^2\chi^2/\partial x_i\partial x_j$). The components of the curvature matrix and $\nabla\chi^2$ are expressed as the

functions of RFs (Ruiz Cobo & del Toro Iniesta 1992), thus the role of RFs in this inversion code is emphasised. SIR uses a Marquardt algorithm which implies that if we are close to the minimum then we can move to it by simply equating the term in brackets in equation (12) to zero and thus

$$\delta \vec{x} = -\mathbf{H}^{-1} \nabla \chi^2, \tag{13}$$

where $\mathbf{H}^{-1}$ is the inverse of the curvature matrix. The situation is more complicated if we are far from the minimum. In this case, a parameter κ must be introduced to control the speed of convergence. The magnitude of this parameter depends on the distance from the minimum and can be up- and down-scaled according to the change between $\chi^2(\vec{x})$ and $\chi^2(\vec{x} + \delta \vec{x})$ (see the scheme in Fig. 8 and del Toro Iniesta (2003) for the detailed theoretical description of this method).

The computation of the equation (13) is not trivial especially because of the large dimension of the curvature matrix. The inversion of large matrixes is a difficult numerical task and is also computationally demanding. To decrease the size of the curvature matrix, we do not compute the perturbation $\delta \vec{x}$ at all optical depths of the model, but only at few grid points called nodes. The perturbation at remaining depths is approximated by the cubic-spline interpolation between the equidistantly distributed nodes.

The number of nodes is given by the user for each atmospheric parameter and could be increased when the new cycle of the inversion is started. The number of cycles is also defined by the user and the inversion code proceed to the next cycle if no significant variation of χ^2 occurs in few last iterations. This option also stops the inversion process and returns the resulting model of the atmosphere if there is no additional cycle to proceed.

4.1.3 Error estimation

Bellot Rubio (1999) has shown that the error of the plasma parameter x_i at the optical depth τ is

$$\sigma_{i(\tau)}^2 \propto \frac{\chi^2}{\sum_{j=1}^n R_i^2(\lambda_j, \tau)}, \tag{14}$$

where χ^2 is the merit function and R_i is the response function of the plasma parameter x_i. Only the approximate relation is presented here to show that the uncertainties are proportional to the merit function and to the inverse of the response function, therefore poor fits have larger errors and parameters that have little influence on the emergent intensity show the largest uncertainties.

The precise form of the equation (14) is shown by e.g. del Toro Iniesta (2003) who also described the assumptions and limitations required for the derivation of this equation. For example, this equation is valid only if all

model parameters are independent, so changes of one parameter do not influence the remaining plasma quantities. The reliability of the equation (14) was tested using the Monte Carlo simulations and it was found out that the uncertainties are well estimated (Westendorp Plaza et al. 2001a).

4.2 Ranges of line sensitivity

The response functions can be also derived in a more simple way which takes on the other hand a long time. The synthetic Stokes profiles are derived from the input model of atmosphere, one of the parameters is changed in a small range of optical depths and a new Stokes spectrum is computed. Then the ratios between the differences of the new and old synthetic spectra and the perturbation of the parameter are computed. These ratios are in fact the response function of that parameter at the optical depth where the parameter was changed. This process has to be repeated for all optical depths to retrieve the absolute RF to that plasma parameter. It is clear then, that RFs behave the same way as partial derivatives of the spectrum with respect to the physical quantities. Therefore, within the linear approximation, RFs give the sensitivities of the emerging Stokes profiles to perturbations of the plasma parameters of the atmosphere. If the value $R_i(\tau, \lambda)$ is close to zero, then the change of the plasma parameter δx_i at the optical depth τ does not influence the emerging intensity at the wavelength λ. The uncertainty of the parameter x_i at the optical depth τ will be large, if $R_i(\tau)$ is close to zero at all wavelength points of all Stokes profiles of all inverted lines. This statement is just the description of the equation (14).

Regarding the importance of the response functions in the inversion code SIR, the examples of RFs to temperature, magnetic field strength, and velocity are shown. Because the propagation matrix and the source function is dependent on the plasma parameters, RFs are dependent on the atmospheric model (i.e. they are different at each pixel of the inverted area). To present some typical RFs, the average models of different areas were made. In Fig. 9 the average stratifications of temperature, magnetic field strength, and velocity of the limbward penumbras (blue lines), umbras (violet lines), narrow light bridges (orange lines), and broad light bridge (red lines) are shown together with the areas from which these average stratifications were obtained.

In Figs. 10, 11, and 12, the response functions to temperature, magnetic field strength, and velocity are shown. Each of these figures contains four panels: RFs of the I profile to the appropriate plasma parameter (upper left), RFs of Q (upper right), RFs of U (lower left), and RFs of V (lower right). Each panel contains eight shaded figures, the left columns correspond to the RFs of Fe I 603.15 nm and the right to Fe I 603.25 nm, the first rows are RFs of the average umbral model (violet lines in Fig. 9), the second rows correspond to the penumbral model (blue lines in Fig. 9), and the third
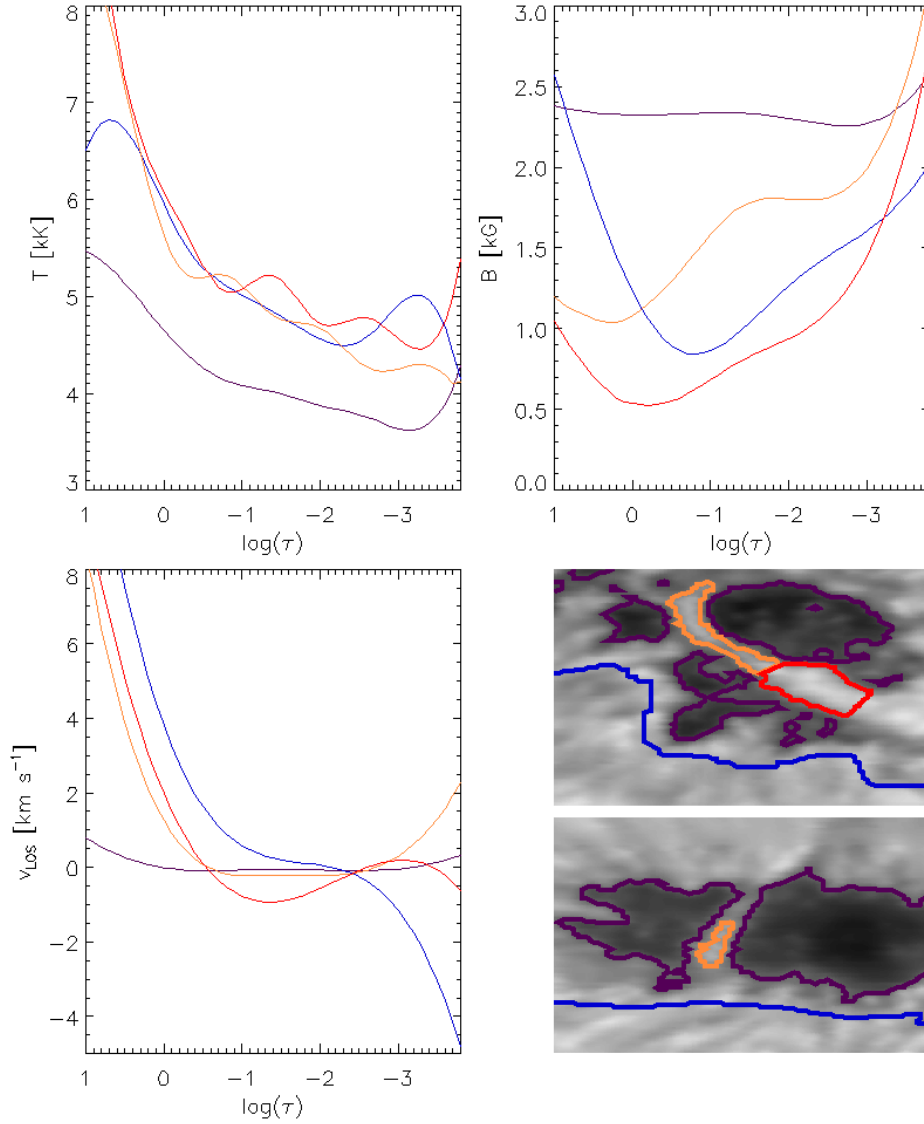
Figure 9: The average stratifications of temperature, magnetic field strength, and velocity from the limbward penumbras (blue), umbras (violet), narrow LBs (orange), and broad LB1 (red).

and fourth rows are RFs of the narrow and broad light bridge respectively (orange and red lines in Fig. 9). On the x axis is the wavelength, where the white tick marks correspond to the line centres. On the y axis is the logarithm of the optical depth in the range from 1 to -3.8 and the dotted line corresponds to the unit optical depth ($\log \tau = 0$).

The units of the response functions are the direct inverse of their corresponding quantities, because they are normalised to the continuum intensity
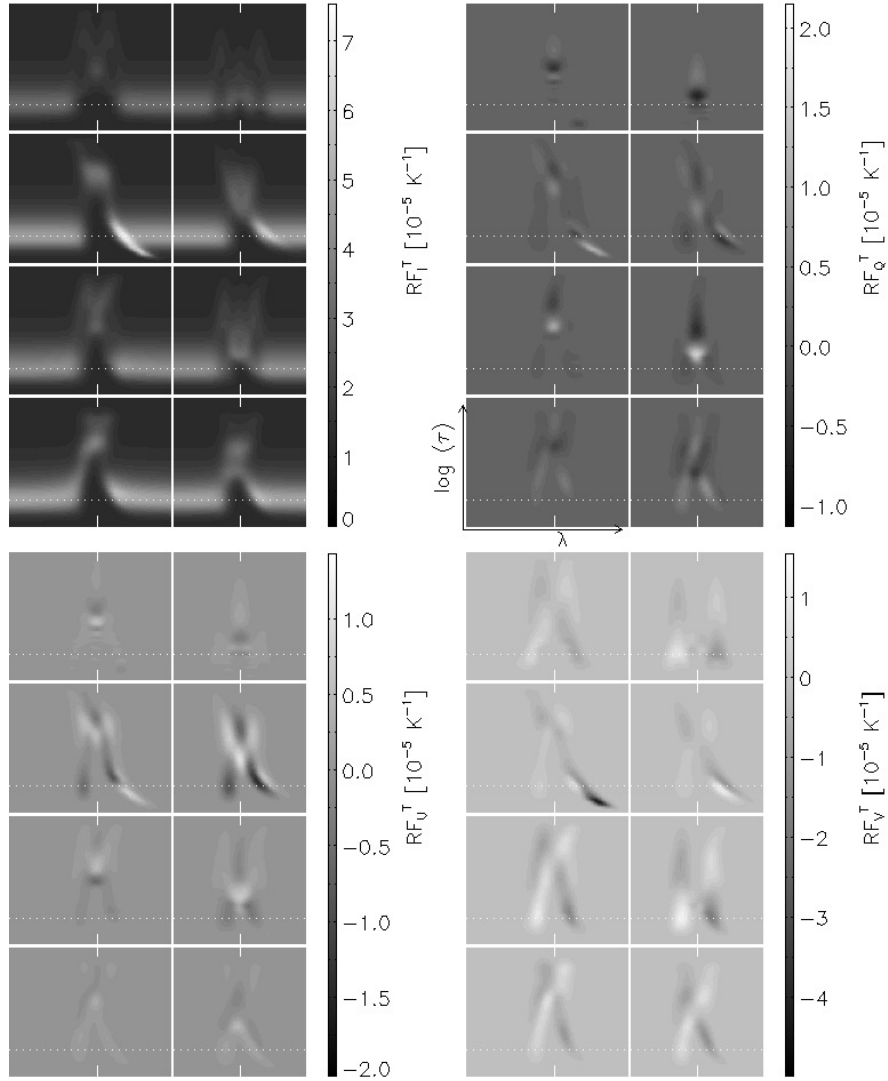
Figure 10: The absolute response functions to temperature. The four panels correspond to the different Stokes profiles (I upper left, Q upper right, U lower left, and V lower right). Each panel contains response functions of Fe I 630.15 (left column) and 630.25 nm (right column) and of four different models of atmosphere (first row – the umbral model, second row – the penumbral model, third and fourth row – the models of narrow and broad light bridges respectively). See detailed description in the text.

of the Harvard Smithsonian Reference Atmosphere (HSRA, Gingerich et al. 1971) at the disk centre at the central wavelength of each spectral line (similarly to the observed Stokes profiles entering the inversion code SIR and to the resulting synthetic profiles).
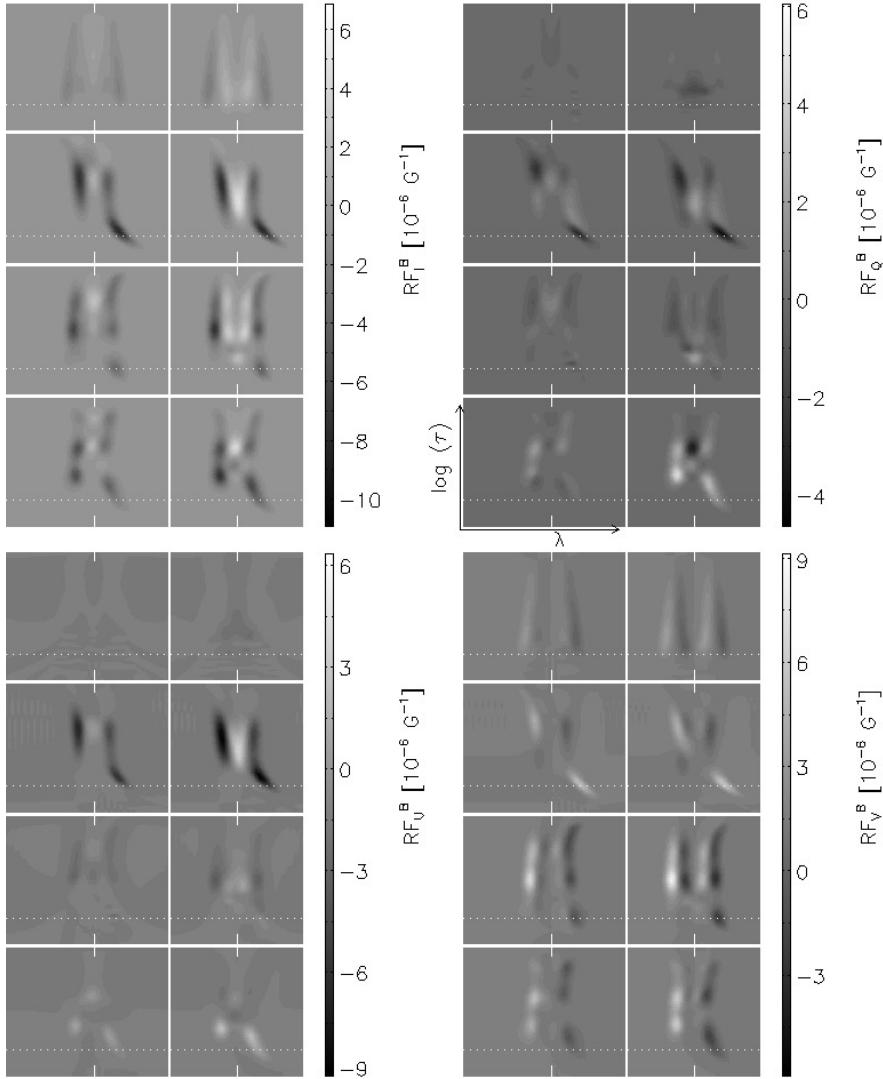
Figure 11: Same as Fig. 10 but for magnetic field strength.

If the magnitudes of RFs to the different plasma parameters need to be compared, the relative response functions are easily defined as

$$\mathbf{R}_i^*(\tau) = \mathbf{R}_i(\tau) x_i(\tau). \tag{15}$$

It means, that the (absolute) RF computed from the equation (9) is multiplied by the appropriate value of the plasma parameter x_i at the optical depth τ resulting into dimensionless (relative) RF.

The examples of relative response functions are shown in Figs 13 and 14. These figures are practically RFs to temperature of the average umbral model (Fig 10 top rows) visualised in 3D plots. In reality, relative RFs to

35
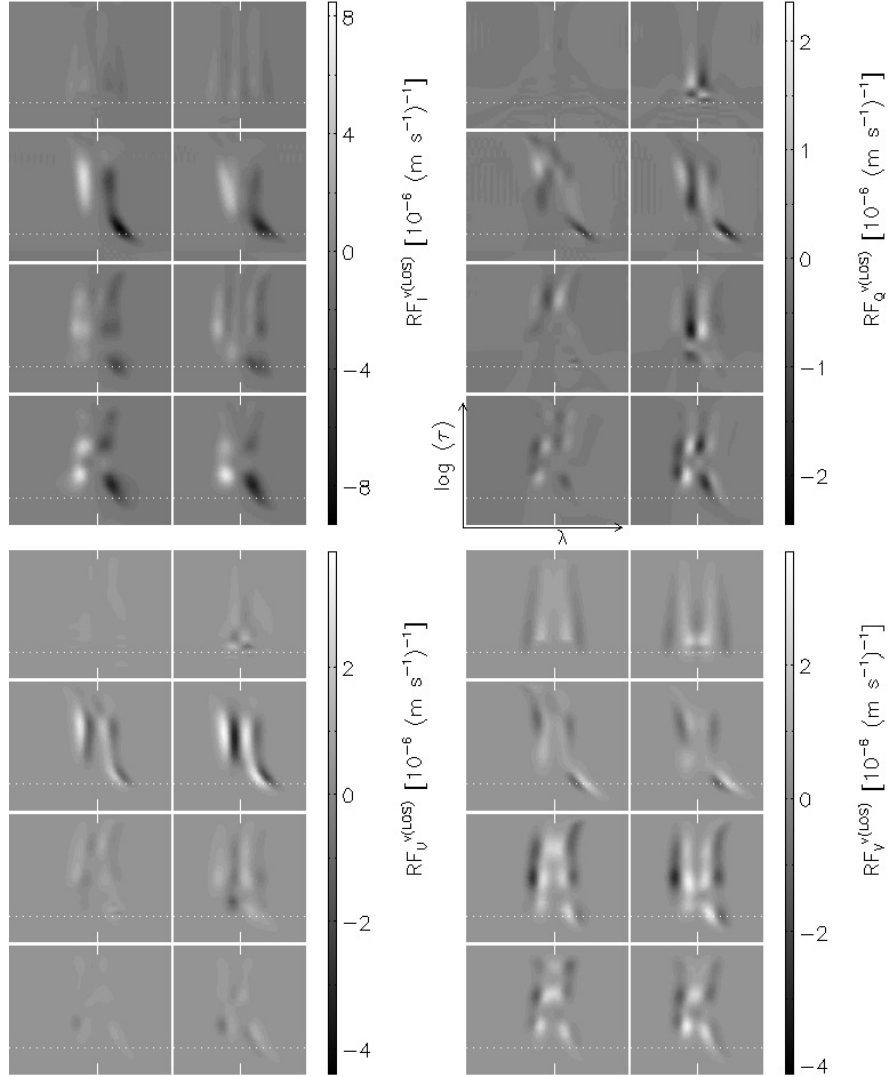
Figure 12: Same as Fig. 10 but for velocity.

temperature, magnetic field strength, and velocity are compared and the highest absolute value of RF at each coordinate of wavelength and optical depth is plotted. On the xy plane of these 3D figures is marked which RF is the biggest at these coordinates; light gray corresponds to the temperature, and dark gray to the magnetic field strength. The absolute values of relative RFs to velocity are everywhere smaller than the RFs to temperature or magnetic field strength. The contours in the xy plane serve for better orientation in the plot.

It is clear, that the temperature is the most important plasma parameter for the emerging shape and intensity of the Stokes profiles. This statement is
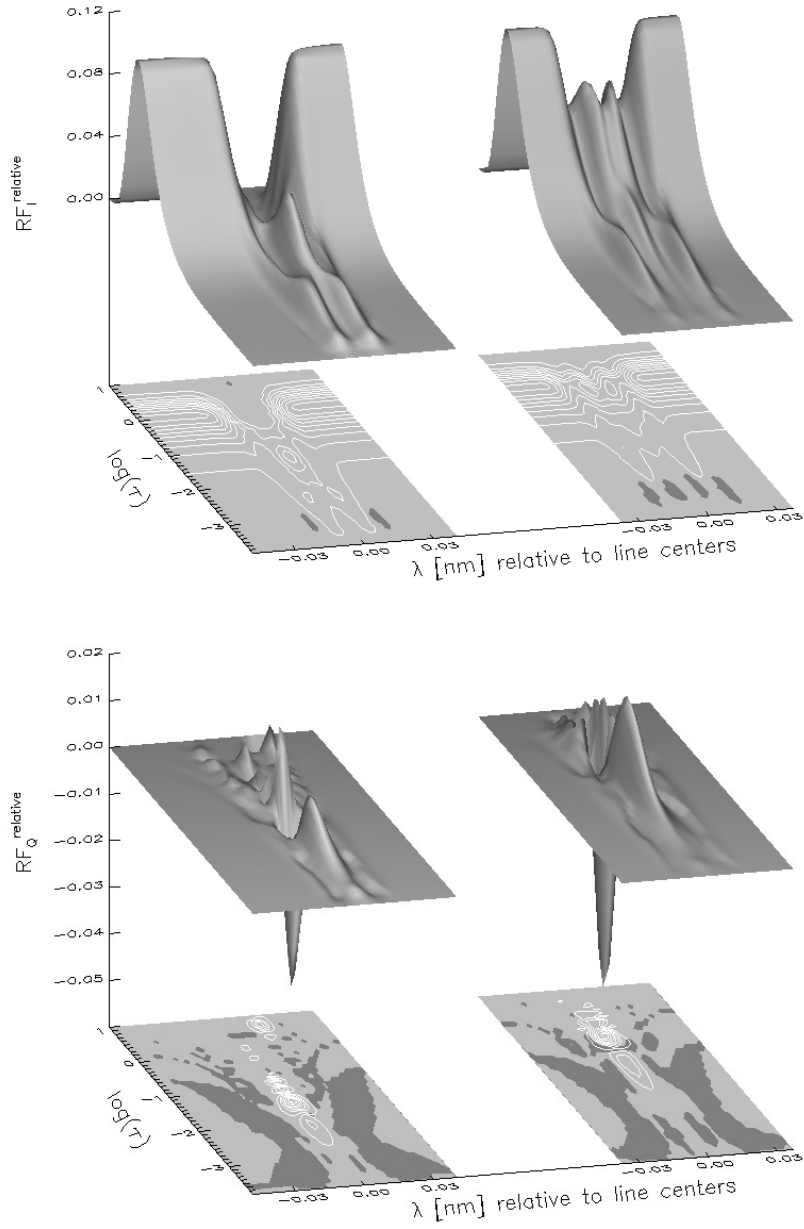
Figure 13: The relative response functions of Stokes I and Q. See the text for details.

true not only for the average umbral model visualised in Figs 13 and 14, but also for the other three average models in Figs. 10, 11, and 12. The reason is that the absolute RFs to temperature are one order higher than RFs to the other two parameters and that the magnitude of magnetic field strength

37
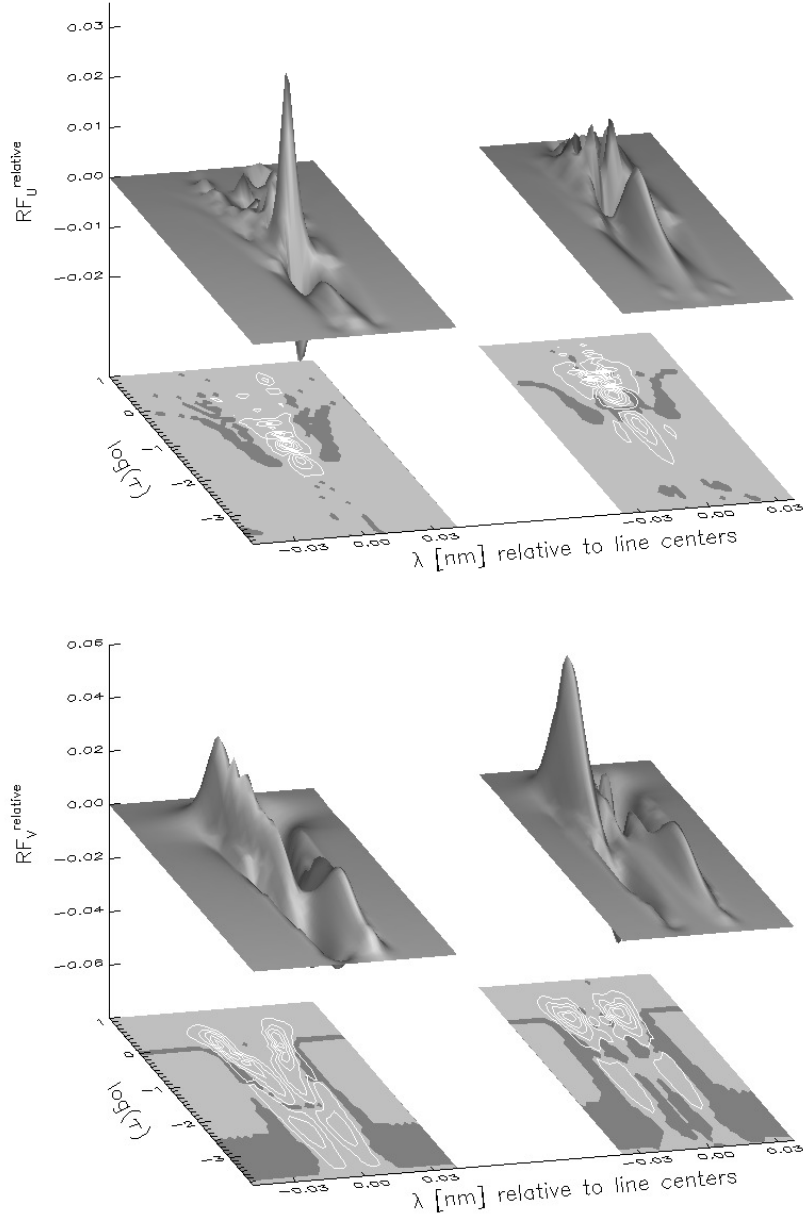
Figure 14: Same as Fig. 13 but for Stokes U and V.

(evaluated in G) or velocity (m s^{-1}) is not higher than the magnitude of temperature (evaluated in K) in the sunspot photosphere. Therefore, the relative RF obtained by the multiplication of these values must be biggest for temperature at almost all depths and wavelengths for all shown atmospheric models.

The difference between RFs to temperature and RFs to other parameters is caused mainly by the LTE assumption. In this case, the source function $\mathbf{S}$ depends only on the temperature, thus the first term in brackets on the right side of the equation (9) is zero for all other parameters (Ruiz Cobo & del Toro Iniesta 1994). The factor $(\mathbf{I} - \mathbf{S})$ in the second term can be considered as a weighting factor dependent on the optical depth. If the thermodynamic equilibrium prevails beneath the photosphere, then the difference between the Stokes spectrum and source functions diminishes at lower layers. Therefore, the response functions to temperature have the slowest trend to zero at large depths and the temperature is practically the only parameter that can be determined at the sub-continuum layers. RFs to other parameters are significant below the unit continuum optical depth only in the presence of the velocity gradient (see Figs. 11 and 12).

The response functions to temperature and to magnetic field strength have the same wavelength symmetry as the appropriate Stokes profiles, i.e. RFs of I, Q, and U are even functions and RFs of V are odd functions. The RFs to velocity have the opposite wavelength symmetry. This becomes clear, if we imagine the role of the temperature and velocity on the shape of the Stokes I profile. The increase in temperature means also the increase in the emerging intensity, which would be the same in both line wings. On the other hand, the presence of velocity shifts the line core and breaks down the symmetry of the line, it means that one of the line wings becomes darker and the other brighter.

Moreover, the presence of the velocity gradients infracts not only the symmetry of the line profiles, but also the symmetry of the response functions. Therefore, the 3D representation in Figs. 13 and 14 corresponds to the average umbral model, because these RFs are the most symmetric. However, RFs of the umbral model are more complicated than RFs of other atmospheric models because of higher magnetic field strength in the umbra. This can be seen e.g. in the upper left panel of Fig. 10, where RFs of the umbral model in the highest row are broader and more complex than RFs of the broad light bridge model in the lowest row (if the asymmetry is neglected).

Many others conclusions, similar to that already pointed out, could be made just by studying RFs shown in Figs. 10, 11 and 12 and comparing them mutually to acknowledge not only the effects caused by the change of various plasma quantities, but also the role of the atmospheric model on the shape of the response function.

4.3   Reliability of the inversion

In the article by Ruiz Cobo & del Toro Iniesta (1992), which introduced the inversion code SIR, the authors proved that the results are confident. Many other studies confirmed the reliability of the inversion code SIR (Ruiz Cobo
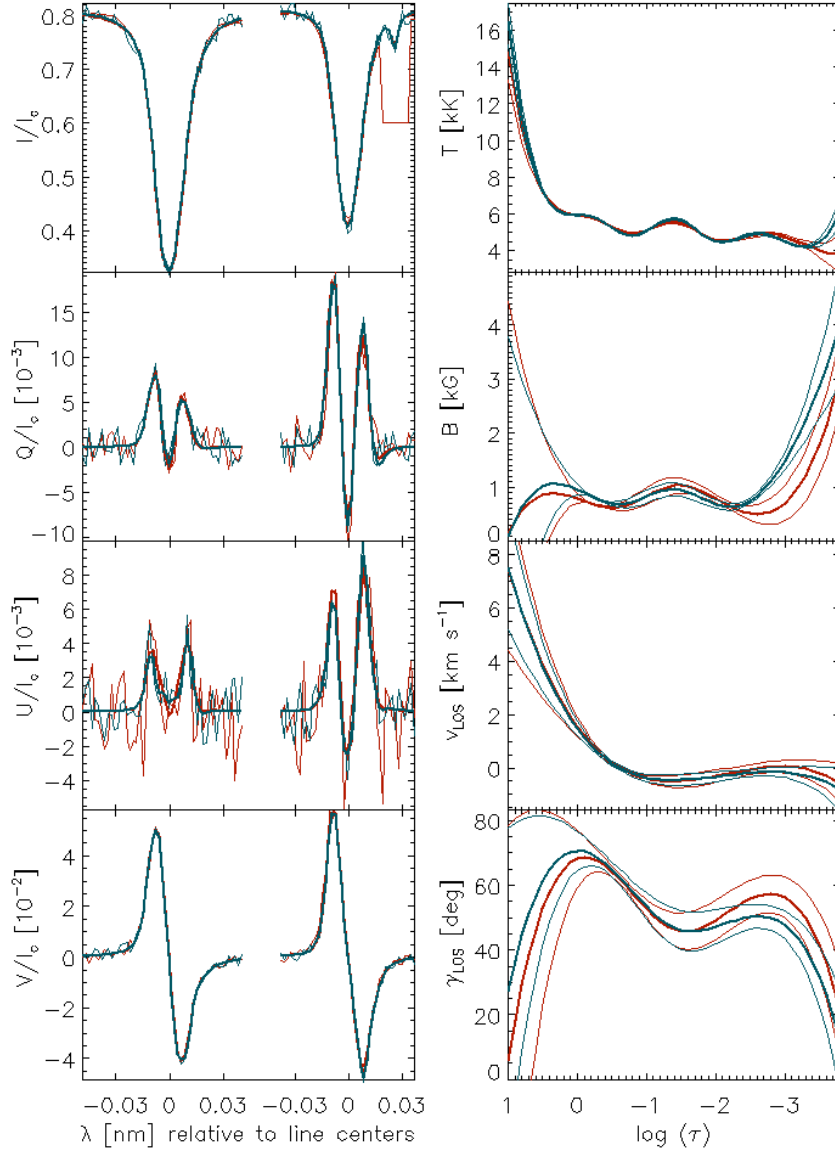
Figure 15: Two profiles differing in noise (thin lines in the left part) were fitted resulting into similar atmospheric models (thick lines in the right part). See the text for detailed description.

1998; Westendorp Plaza et al. 2001a,b).

Two different simple tests are presented here to show that the resulting model of atmosphere is almost independent on the initial model and that the noise does not influence the retrieved model of atmosphere significantly.

In the left part of Fig. 15, the observed Stokes profiles from the broad part of the first light bridge (thin red lines) were inverted, resulting into the
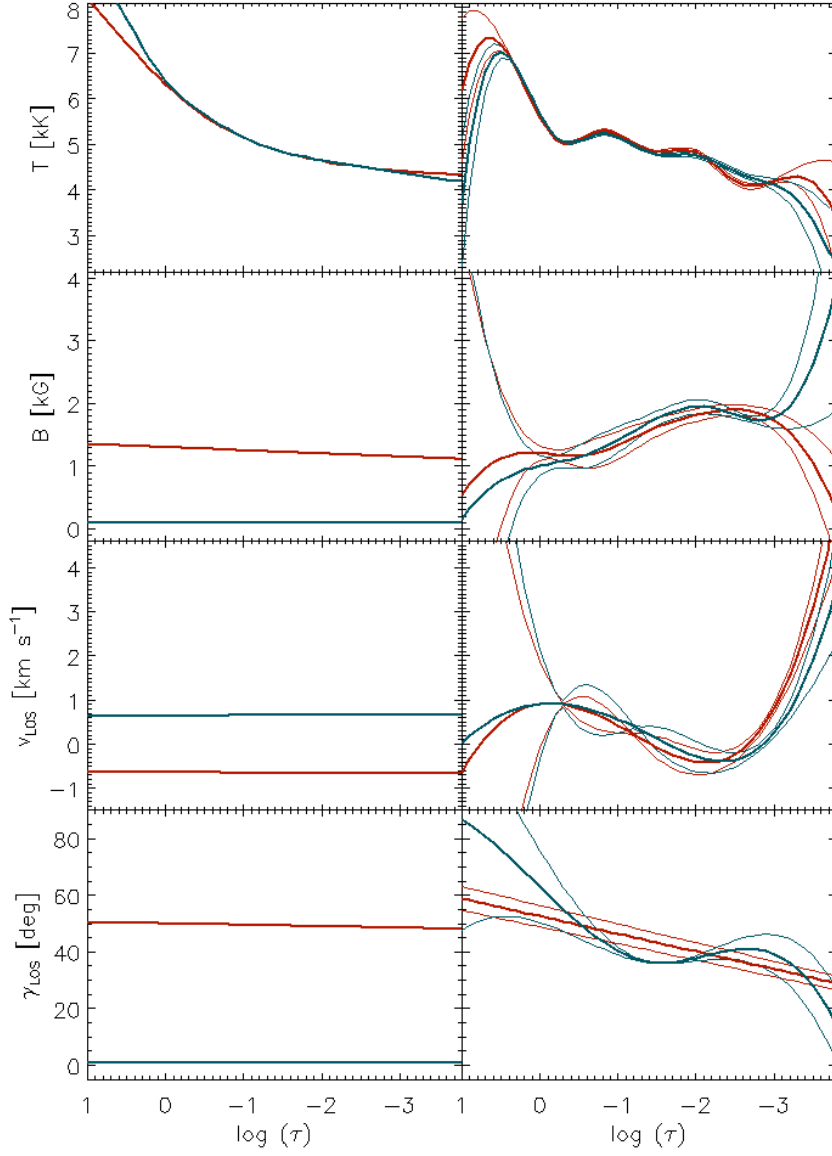
Figure 16: Two different starting models of atmosphere (red and blue lines in the left part) were used together with the same set of observed Stokes profiles resulting into similar atmospheric models (thick lines in the right part). See the text for details.

atmospheric model from which the stratifications of temperature, magnetic field strength, velocity, and inclination are shown in the right part of Fig. 15. The thick red lines represent the inverted values and the thin red lines show the error limits of these parameters. The synthetic Stokes spectrum of this atmospheric model is represented by the thick red lines in the left part of

Fig. 15. If the SIR code is applied to this synthetic spectrum, the resulting stratifications of plasma parameters will be exactly the same. Therefore, a random noise was added to this synthetic spectrum and these noisy Stokes profiles are represented by the thin blue lines. The resulting stratifications of the plasma parameters inverted from these noisy Stokes profiles are represented by the blue lines in the right part of Fig. 15 and the synthetic profiles are represented by the thick blue lines in the left part of Fig. 15 where the thin blue lines show the corresponding error limits.

The synthetic profiles are almost the same. The difference is biggest in the Stokes U profile, which is also the most noisy one. The resulting stratifications of the plasma parameters are very similar, what proves the reliability of the inversion and the small influence of the noise. The differences between the stratifications are in the ranges of errors almost everywhere except the higher layers of the atmosphere, where RFs to the plasma parameters are diminishing. The sensitivity of the Stokes profiles to appropriate plasma parameters can be estimated from the ranges of errors, i.e. the temperature is the most accurately predicted parameter, the magnetic field strength and velocity have similar ranges of reliability and therefore similar magnitudes of influence on the emerging Stokes profiles, and the inclination is the most uncertain parameter from the shown plasma quantities and has the smallest impact on the observed intensity and shape of the Stokes profiles.

In the left part of Fig. 16, two different initial models of atmosphere are shown. The red line corresponds to the average penumbral model, which was finally used as the initial model of atmosphere for all pixels in the field of view; the details about this model are presented in the next section. The second initial model (blue lines) is based on HSRA, where the magnetic field strength was set to constant value of 100 G, the velocity stratification corresponds to the negative values of the velocity stratification of the first model, and the inclination is 1 degree at all atmospheric depths.

These initial models of atmosphere were used to invert the same set of Stokes profiles, which were observed in the narrow part of the second light bridge. Neither the observed profiles nor the synthetic Stokes profiles are shown here, because they fit the observations very accurately and the fits do not differ much between each other.

The resulting models of atmosphere are compared in the right part of Fig. 16. The stratifications of temperature, magnetic field strength, and velocity have very similar shapes. The differences between the stratifications are smaller than the ranges of errors up to the higher layers of atmosphere giving confidence into the reliability of the inversion code SIR. However, the shapes of the stratifications of inclination are different and because of that, there is a discrepancy of inclination values about $10°$ in otherwise trustworthy range of heights from log $\tau = -1$ to log $\tau = -1.8$. As was already pointed out, the radiation is not very sensitive to the changes of inclination and therefore, such discrepancy is possible.

4.4 Parameters of the inversion code SIR

4.4.1 Input parameters

The first step in the inversion process is the computation of the synthetic Stokes profiles. To do that, the input files, which were the same for all inverted points, are needed.

The abundances of various chemical species were quoted by Thevenin (1989). The abundance y of a chemical specie x is given relatively to the number of hydrogen atoms H as $y = 12 + \log(x/H)$. In this scale, the abundance of the hydrogen is evidently 12 and e.g. the abundance of the iron is 7.46. Totally, the abundances of 92 chemical species are included in the SIR code.

The atomic parameters of the neutral iron lines used for the inversion are listed in Tab. 1. The values of central wavelength were taken from the work by Nave et al. (1994), the excitation potential and $\log(gf)$ from the work by Thevenin (1990), and the last two parameters describing the broadening of these lines by neutral hydrogen were computed using the method and code described in the article by Barklem et al. (1998).

As was said in the previous section, the initial model of atmosphere is the same for all inverted points. This model is taken from the work by Martínez Pillet (2000) where it was used as the background model of the penumbral atmosphere in which the horizontal flux tubes were embedded. The stratifications of temperature, magnetic field strength, velocity, and inclination are shown in the left part of Fig. 16 (red lines). Moreover, there are other parameters in the input file. The micro- and macro-turbulence are set to 1 km s^{-1} at all depths. The macro-turbulence is not a free parameter of the inversion and remains constant. The azimuth is 238 degrees everywhere and the values change during the inversion process. The last stratification in the input file corresponds to the electron pressure (Fig. 17), but this parameter is not fitted, because after each iteration step the electron pressure of the already perturbed atmosphere is put into the hydrostatic equilibrium by us-

λ_{lab} [nm]	$\mathrm{EP}_{\mathrm{low}}$ [eV]	$\log(gf)$	atomic transition	α_V	σ [cm^2]
6301.5012	3.65	-0.59	${}^5\mathrm{P}_2 - {}^5\mathrm{D}_2$	0.2428	2.344×10^{-14}
6302.4936	3.69	-1.16	${}^5\mathrm{P}_1 - {}^5\mathrm{D}_0$	0.2406	2.973×10^{-14}

Table 1: The atomic parameters of the neutral iron lines: λ_{lab} is the central wavelength in the air, $\mathrm{EP}_{\mathrm{low}}$ the excitation potential of the lower level, $\log(gf)$ the logarithm of the multiplication of the degeneracy of the level and the oscillatory strength, α_V the velocity parameter, and σ the line broadening cross section.
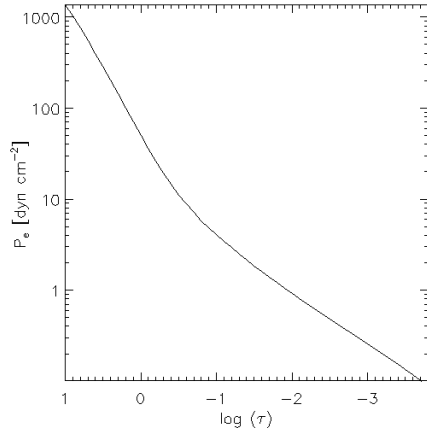
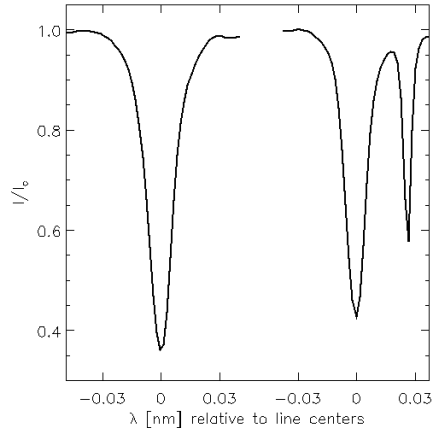Figure 17: The initial stratification of the electron pressure.

Figure 18: The Stokes I profile of the stray light.

ing the equation of state of an ideal gas with variable mean molecular weight to take into account the partial ionisation of the various atomic elements.

The synthetic Stokes profiles can be mixed with the stray light to increase the accuracy of the inversion. The stray-light profile is the same for all inverted points, although the portion of the stray light is a free parameter of the inversion and differs at each pixel. The profile of the stray light was taken from the quiet sun. Therefore, only the I profile, which is shown in Fig. 18, is not equal to zero. However, the exact stray-light profile depends on the location in the sunspot and is generally unknown. For example, close to the umbra, there must be also some stray light of Stokes Q, U, and V profiles. The dependence of the resulting stratifications of plasma parameters on the stray light profile is discussed in Sect. 5.3.2.

4.4.2 The number of nodes

The inversion process is directed by the control file. In this file is described e.g. the possible source file with the stray-light profile, the initial model of atmosphere, the source files for the abundances and atomic parameters, and if the inversion will consider one- or two-component model of atmosphere.

As was already mentioned in the description of the inversion process, the number of cycles and the numbers of nodes for each physical parameter is specified by the user and these numbers are given in this file. The version of the SIR code, which was used in this thesis, does not take the number of nodes as an obligatory value, but as the maximal possible value. A practical example of this can be seen in Fig. 16, where both inversions were directed by the same control file, but the resulting stratification of inclination has in one case two nodes (red line) and four nodes in the second case (blue line), which causes the discrepancy of the inclination values.

44

	The number of nodes for:				
Cycle	T	B	v_{LOS}	γ_{LOS}	ψ_{LOS}
1	2	1	1	1	1
2	3	2	2	1	1
3	9	4	4	2	2
4	9	5	5	4	3
5	9	7	5	5	4

Table 2: The numbers of nodes for temperature, magnetic field strength, velocity, inclination, and azimuth for all cycles.

The number of nodes cannot be arbitrary, because the nodes must be distributed equidistantly in the atmosphere. Therefore, the number of nodes is a function of the total number of depth points. The used initial model of atmosphere, which determines the number of depth points, was defined at 49 optical depths starting at $\log\tau = 1$ and going up in the atmosphere with steps of 0.1 till $\log\tau = -3.8$. Therefore, the number of nodes can be: 0 (the parameter is not inverted), 1 (the parameter is height-independent), 2, 3, 4, 5, 7, 9, 13, 17, 25, and 49. If another number of nodes is specified, the SIR code decreases this number to the first possible value listed above.

Higher number of nodes usually means smaller merit function, although the precise form of equation (11) contains the number of degrees of freedom, which may be used as a "warning key" to remember that the number of nodes cannot be unreasonably large.

The chosen number of nodes corresponds to the expected complexity of the stratification of the appropriate parameter. The aim of this thesis lies mainly in the analysis of the light bridges and penumbra, where the complex stratifications are expected. On the other hand, no breakthrough could be expected in the analysis of the umbra, which photospheric layers are quite simple. Therefore, high numbers of nodes were chosen to cover the possible complexity in the stratification of plasma parameters. The numbers of nodes for the important plasma parameters are listed in Tab. 2, these numbers were used for all inverted points. From this table is also evident that 5 cycles of the inversion process were computed.

In the left part of Figs. 19, 20, 21, and 22 the average Stokes profiles (red lines) are plotted. These average profiles were taken from the areas marked in the lower right part of Fig. 9. The average profiles are inverted and the synthetic Stokes profiles (left part) and stratifications of the temperature, magnetic field strength, velocity, and inclination (right part) are plotted with the blue lines in Figs. 19–22 . The stratifications coming from the inversion are compared with the average of individual stratifications in each
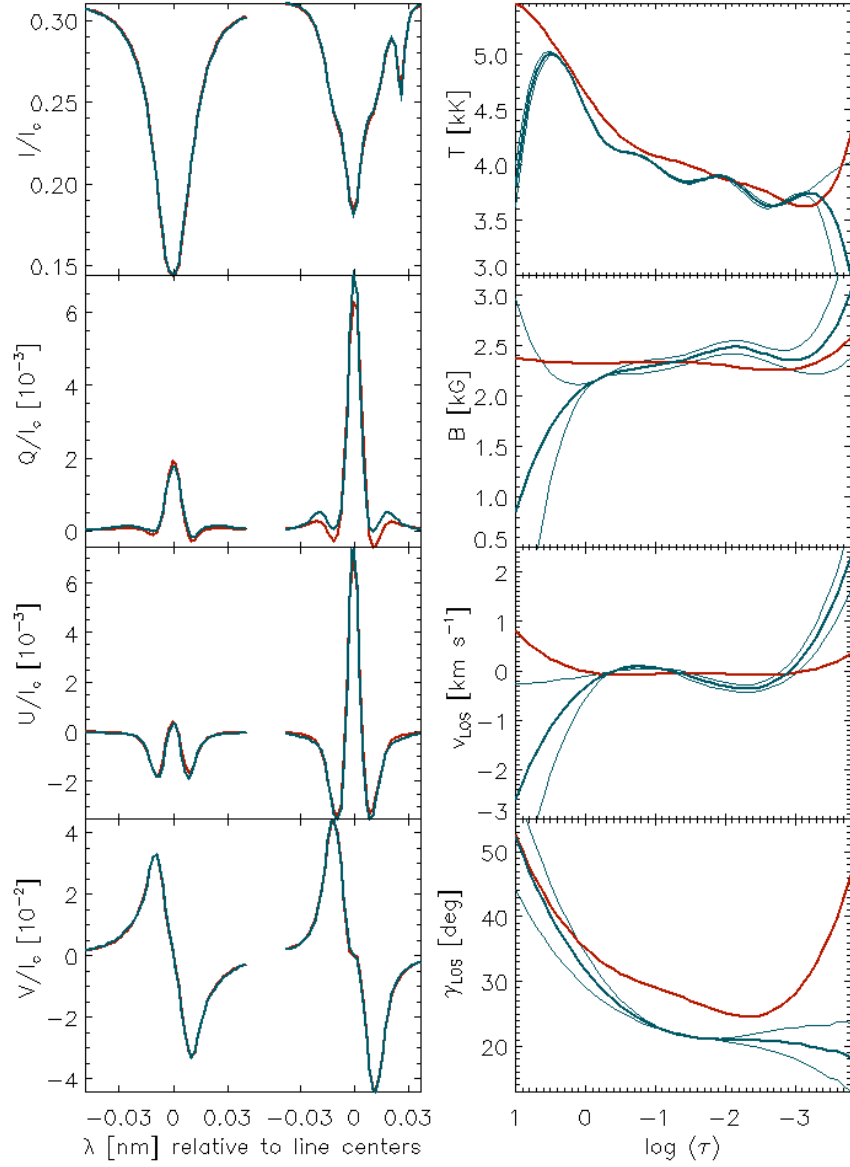
Figure 19: The average umbral profiles (red lines) are inverted and resulting stratifications of the plasma parameters (blue lines) are compared with the average umbral stratifications (red lines).

pixel of the selected areas. From this comparison, the suitable numbers of nodes can be estimated.

It cannot be expected that the average stratifications will be reproduced by the fitted ones, because the inversion process is not linear. However, the stratifications coming from the inversion should not be much more complex
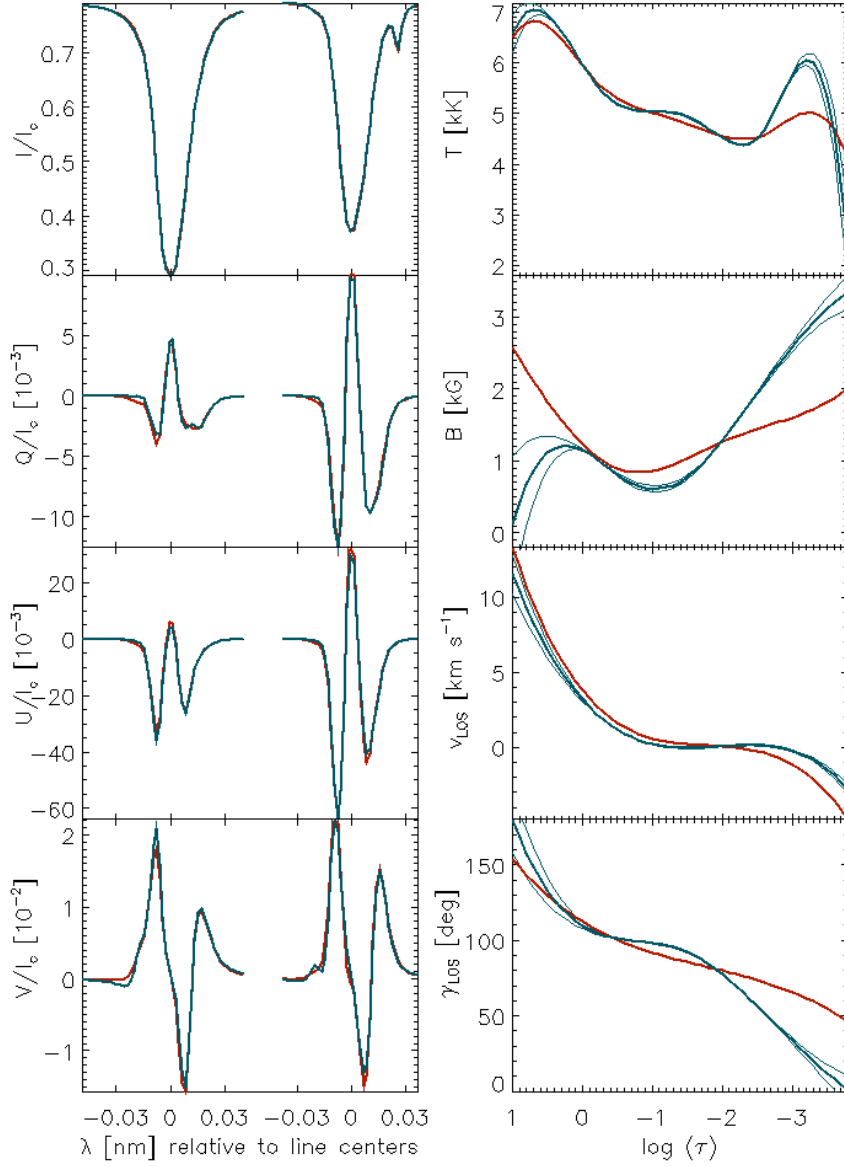
Figure 20: Same as Fig 19, but for average penumbral profiles.

than the average ones, because that would mean that the number of nodes is too high. On the other hand, the average stratification could smooth some interesting characteristics of the atmosphere which occur only in some small part of the area, from which the average is made.

In Fig. 19 the profiles and stratifications from the umbra are plotted. As was expected, the resulting stratifications (blue lines) are much more complex than the average one, because the umbral photospheric layers are
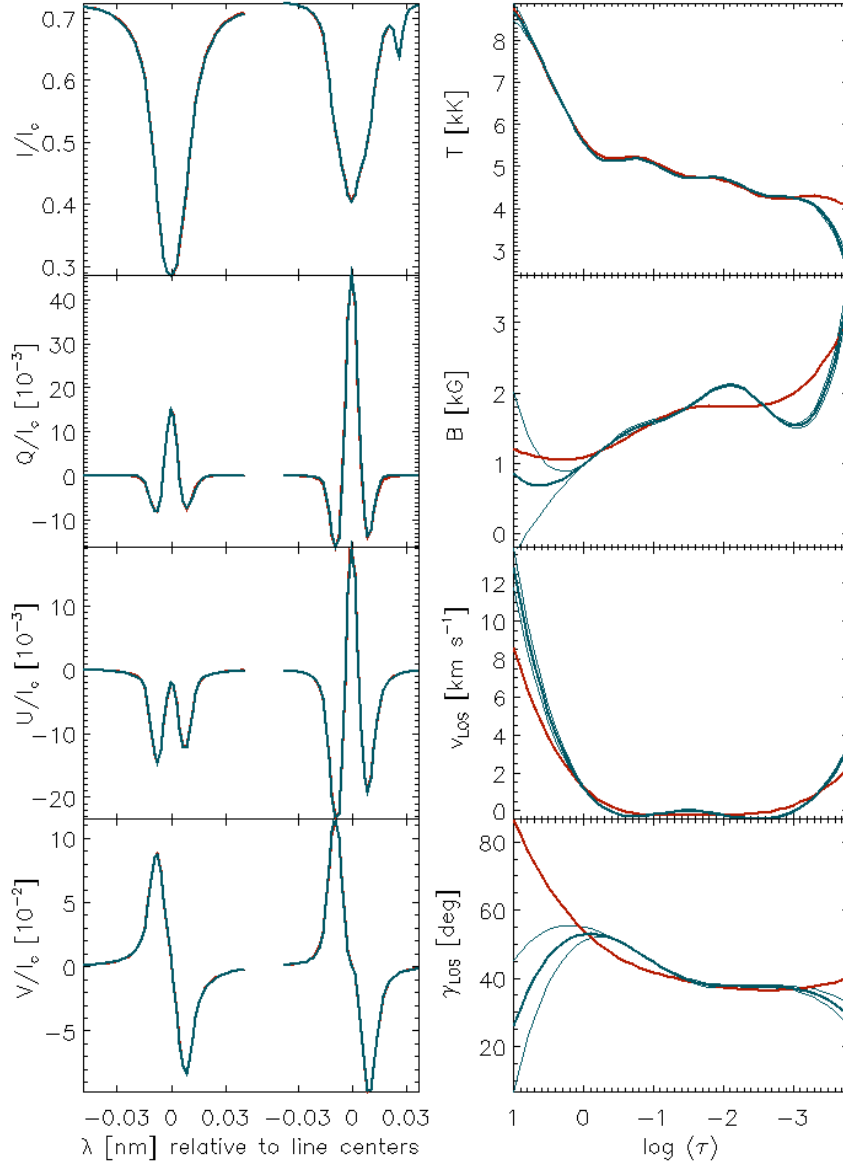
Figure 21: Same as Fig 19, but for average profiles from the narrow light bridge.

almost homogeneous and the chosen number of nodes is inappropriate for the plasma parameter stratifications in this region.

In Fig. 20 the penumbral profiles and stratifications are shown. Although the averages are made only from the limbward part of the penumbra to avoid the different line-of-sight velocities, the profiles from the bright and dark filaments are mixed and some fine differences in plasma stratifications between
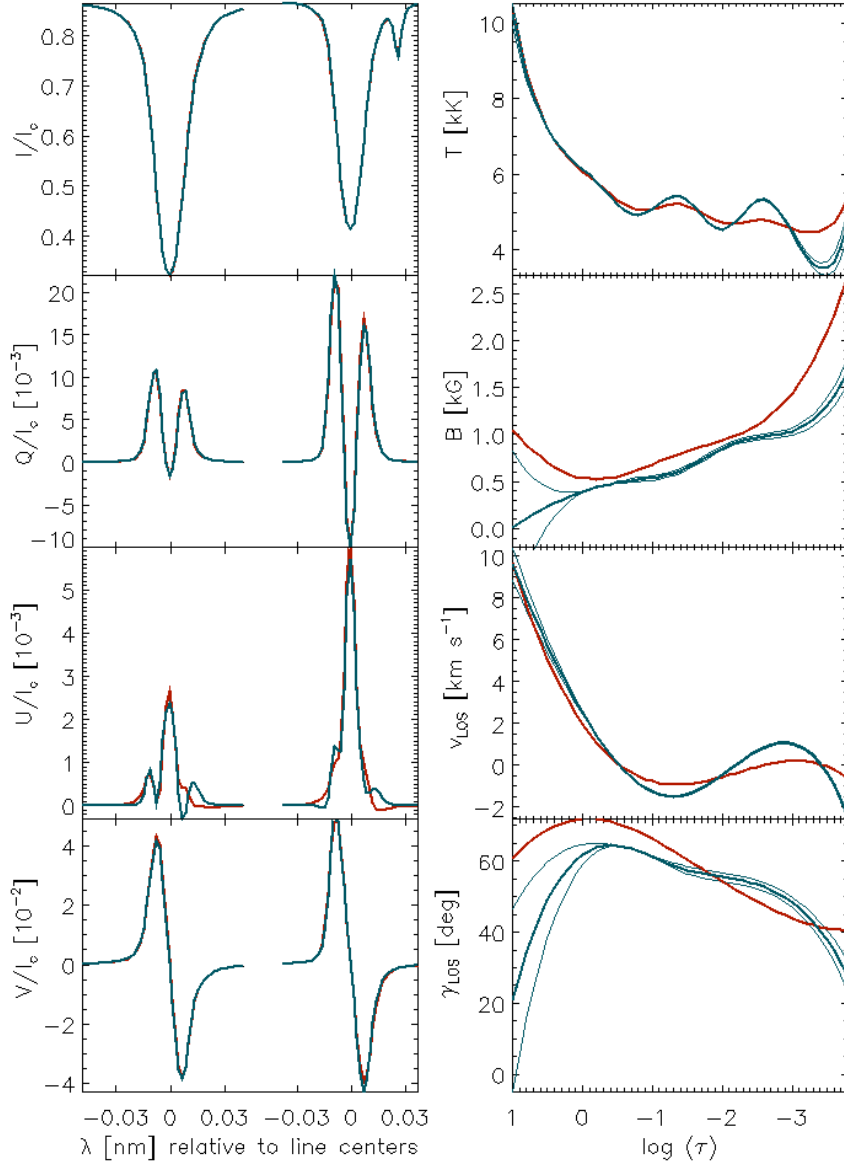
Figure 22: Same as Fig 19, but for average profiles from the broad light bridge.

these two components of the penumbra can be smoothed out. Although the number of nodes seems to be too large for the plasma parameters, except of the velocity, the penumbral stratifications needs a detailed discussion, which is given in Sect. 5.2.

In Figs. 21 and 22 is shown the reason for the high number of nodes for the temperature stratification. It can be seen, that even the average profiles

49

from the light-bridge areas carry some information about the complex temperature stratification there and the fits reproduce correctly the height of temperature enhancements, which origin is discussed in Sect. 5.3. However, the average stratifications of the other plasma parameters seems to be more simple than the inverted ones, i.e. the numbers of nodes are inappropriately high in case of magnetic field strength, velocity, and inclination.

According to the comparison between the average stratifications and the fitted ones, the chosen number of nodes for temperature is needed for the description of the light bridge atmosphere and the number of nodes for velocity is needed in the penumbral atmosphere. It seems, that the numbers of nodes for the magnetic field strength and inclination are higher than it is necessary. However, the conclusions are not based on the individual models of atmosphere, but on the maps of plasma parameters and on the average models of atmosphere from small regions, where the effect of too many nodes is imperceptible and reduced respectively.

4.4.3 Output parameters

There are three output files. The first one contains the synthetic Stokes profiles. The second file corresponds to the resulting model of atmosphere, which corresponds to the altered initial model where three more columns with plasma quantities are added. The last file has the same structure as the file with the atmospheric model, but contains the errors of the plasma parameters.

As the resulting model of atmosphere is the most important, the detailed structure of the file follows. The first line contains three numbers, the macro-turbulent velocity, which is not the parameter of iteration and remains equal to 1 km s^{-1}, the filling factor, which in case of one-component model of atmosphere is equal to 1, and the fraction of the stray light given in percents.

Then 11 columns follow. The first one defines the optical depths in which the magnitudes of the plasma quantities are computed and this column is the same as in the input model of atmosphere. The stratifications of the temperature (T), the electron pressure (P_e), micro-turbulent velocity (v_{mic}), the magnetic field strength (B), the line-of-sight velocity (v_{LOS}), inclination (γ_{LOS}), and azimuth (ψ_{LOS}) are evaluated in columns $2-8$. These columns correspond to the altered initial values of these parameters given in the starting model of atmosphere.

The ninth column contains the geometrical height h in the atmosphere above the unit continuum optical depth. The SIR code takes into account the influence of the plasma parameters on the opacity, thus e.g. the optical depth $\log \tau = -1$ corresponds to the different geometrical height in the umbra and in the penumbra. This parameter does not solve the pixel to pixel fluctuations of the local Wilson depression, because the SIR code expects that $\log \tau = 0$ is equivalent to 0 km everywhere, which is not true

according to the observations. The tenth column contains the gas pressure P_g, which is computed from the temperatures and electron pressures under the assumption of LTE. The last column contains the density ρ.

Some output parameters cannot be directly used and need to be modified. The transverse-field component direction is unsigned, so that there is a $180°$ ambiguity in the azimuth values. In each of the analysed areas, the sum of differences between the azimuths was minimised, and thus the ambiguity problem was solved. The corrected values of azimuth along with inclination of the magnetic field vector coming from the SIR code are evaluated with respect to the line of sight. The transformation of these variables to the local reference frame was made; hereafter, the inclination γ is the angle between the magnetic field vector and the local normal line, and the azimuth ψ is reckoned from the north and increases counterclockwise. Hereafter, the stratifications of the plasma parameters will be plotted with regard to the geometrical height, because this enables to compare the layers in the atmosphere which are in reality closer than layers with the same optical depth.

It was not yet mentioned that one of the input parameters is the heliocentric angle μ. The problem is, that the SIR code is working properly only with this parameter equal to 1, but the correct value for the observations analysed here is around $\mu = 0.91$ (depending on the position in the sunspot). Therefore, the retrieved values of plasma parameters are not evaluated at heights listed in the files with the resulting model of atmosphere, but these heights must be shifted by $\log \mu$, which is around 0.04 for our observations. As this value corresponds roughly to 7 km at the photospheric layers and the shift is almost the same everywhere, this correction of heights is not realised. In the inversion process, only the equation of hydrostatic equilibrium is influenced by the incorrect value of the heliocentric angle. According to Basilio Ruiz Cobo (private communication), this effect is nearly negligible for $\mu = 0.91$.

5 Results

The resulting values of various plasma parameters were obtained at all points in the areas marked on the white-light image shown in Fig. 7. As is described in the previous sections, the retrieved values of plasma quantities are trustworthy at a restricted range of heights. Therefore, the results at six different geometrical heights are shown in Figs. 38, 39, 40, and 41 for the first area and in Figs. 42, 43, 44, and 45 for the second area. All of these figures are shown in the appendix Colour plates. The white contours in these figures correspond to the umbral, the penumbral, and the light bridge boundaries.

The geometrical heights 0, 50, 100, 150, 200 and 250 km correspond to the average optical depths $\log \tau = 0, -0.34, -0.68, -1.02, -1.38,$ and -1.74 respectively. The SIR code sets the geometrical height $z = 0$ km to the optical depth $\log \tau = 0$, i.e. the effect of different temperatures and gas pressures on the opacity is not taken into account at this layer. The geometrical heights of other layers are computed at each of the analysed pixels separately with regard to the local stratification of temperature and gas pressure. Therefore, the same geometrical height corresponds to different values of the optical depth at each pixel and the average values of optical depth must be listed.

The range of uncertainties can be roughly estimated from previous figures, if we know the approximate values of the optical depths corresponding to the shown geometrical heights. The validity of the results can be also estimated from the smoothness of the resulting maps of various plasma parameters, as the values of the plasma quantities at each pixel were computed with no regards to the surrounding pixels (SIR is a one-dimensional code).

The results are discussed in separate sections with regard to the location in the sunspots, i.e. the umbra, the penumbra, and the light bridge. This separation is based on the continuum intensity ($I_{umbra} \leq 0.4 \times I_{max}$, $I_{penum,lb} \geq 0.55 \times I_{max}$) and is marked in Fig. 37 (Colour plates). The average values of the plasma parameters in these areas are summarised in Tab. 3 at heights, which are shown in Figs. 38–45. The first light bridge is separated into the narrow and broad parts according to the contours in the lower left part of Fig. 9.

5.1 Umbra

As was shown by previous studies (see e.g. Westendorp Plaza et al. 2001a and references therein) and as is predicted by all sunspot models, the umbra is the coolest area in the sunspot with the most intense magnetic field. These general characteristics are confirmed by the results also in the case of a highly irregular sunspot, where the umbral cores are separated by the light bridges.

The temperature is decreasing with height in the umbra, as everywhere in the photosphere. This trend is fastest at the low layers as can be seen in

Parameter	z[km]	Umbra	Penumbra	LB (narrow)	LB (broad)
T [K]	0	4850	5837	5593	5829
	50	4565	5398	5239	5386
	100	4330	5218	5142	5193
	150	4210	5085	5014	5114
	200	4132	4902	4811	5013
	250	4012	4731	4674	4874
B [G]	0	2268	1284	1220	918
	50	2198	1085	1371	1070
	100	2163	1019	1520	1199
	150	2163	1071	1632	1274
	200	2162	1188	1704	1312
	250	2133	1299	1740	1352
γ [deg]	0	29	78	38	45
	50	24	72	31	41
	100	21	67	26	37
	150	20	63	24	35
	200	19	59	22	32
	250	19	56	21	30
v_{LOS} [m s^{-1}]	0	135	3235	1090	1770
	50	-35	1630	240	455
	100	-70	745	-165	-185
	150	-40	300	-280	-415
	200	-20	160	-245	-400
	250	-30	140	-225	-325

Table 3: Summary of the average values of temperature, magnetic field strength, inclination, and velocity in different regions of the studied areas.

Figs. 38 and 42 and in Tab. 3. From these figures is also evident that the coolest areas correspond to the darkest parts of the umbra at all heights. This dependence of temperature on the height in the atmosphere and on the continuum intensity is also shown in the upper left part of Fig. 23.
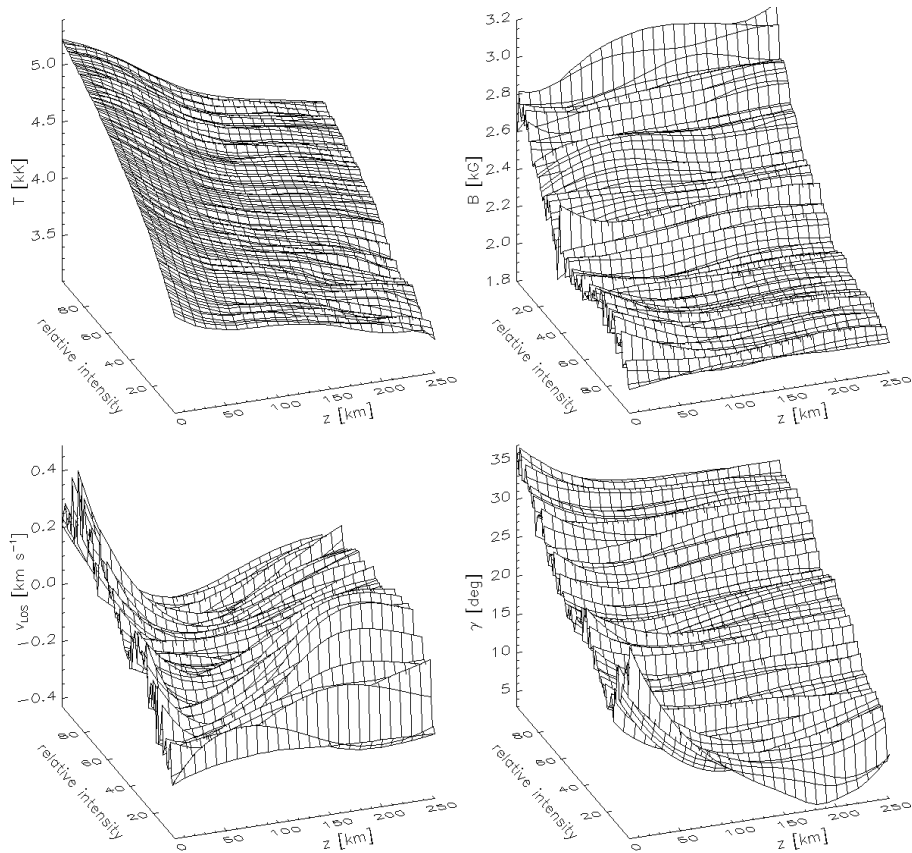
Figure 23: The dependence of temperature (upper left), magnetic field strength (upper right), velocity (lower left), and inclination (lower right) on the height in the atmosphere (x axis) and on the continuum intensity (y axis) in the second umbra.

In the upper right graph of Fig. 23, the same diagram is plotted for the magnetic field strength. The visual impression is similar to the temperature behaviour, but note that the intensity axis has the opposite orientation, thus the darkest parts of the umbra have the strongest magnetic field strength, as can be seen also in Figs. 39 and 43. The average values shown in Tab. 3 decrease with height in the atmosphere, although this trend is negligible if the uncertainties are accounted for at the middle and upper layers. Similar conclusion can be estimated also from Fig. 23, where the decrease in the magnetic field strength is hardly distinguishable. Same results were obtained by Westendorp Plaza et al. (2001a), although he found steeper decrease of magnetic field strength in low layers (1.5–2 G km^{-1}) compared to the average gradient computed from the values in Tab. 3 which is around 1 G km^{-1} between 0–100 km (positive gradients with height mean the decrease of the values with increasing height).

In places of the brightest umbral dots, which can be seen in the first area in Fig. 37, the temperature is higher (Fig. 38) and the magnetic field strength is smaller (Fig. 39) than in the surrounding umbra at geometrical heights 0 km and 50 km. At high layers these small structures disappear as is predicted by all umbral dot models (Parker 1979; Weiss et al. 1990; Wentzel 1992; Degenhardt & Lites 1993a,b) summarised in Sect. 2.3.3. The properties of the umbral dots in the first area were already studied in the article by Socas-Navarro et al. (2004). Therefore, the stratifications of the plasma parameters in these umbral dots are not analysed in this thesis.

The magnetic field is almost vertical in the darkest parts of the first and second umbra (Figs. 40 and 44). The inclination increases with brightness as is shown in the lower right diagram of Fig. 23. This is consistent with the increase in inclination when moving from the darkest central parts to the edges of the umbra. The magnetic field is expanding with the height in the atmosphere, it means that the inclination is increasing along the magnetic field lines. However, the resulting values of the inclination are computed above some fixed position and with the height in the atmosphere different magnetic field lines are sampled by the line of sight and the averaged inclination of these field lines is decreasing as suggest the values in Tab. 3. This decrease in the inclination is restricted only to low layers of the photosphere and the gradient at these low layers is on average $9 \cdot 10^{-2}$ deg km^{-1}, which is much larger than the value found by Westendorp Plaza et al. (2001a) at the outer parts of the umbra. However, the values of inclination are rather uncertain at $\log \tau = 0$, which makes it difficult to rely on them. The nice example for the unlikely behaviour of the inclination can be seen in Fig. 23 for the darkest parts of the umbra as these average stratifications were computed from only two points.

The velocities are close to the zero at all heights in the umbras as can be seen in Figs. 41 and 45 and in Tab. 3. The dependence of velocity on the height in the atmosphere and on the continuum intensity shown in the lower left panel of Fig. 23 suggests that brighter areas exhibit downflows around 200 m s^{-1} and the darkest regions upflows around 200 m s^{-1} in the lowest layers and that the velocity is around 0 at the highest layers. However, small absolute values of velocity reached in the umbras have relatively large uncertainties and the resulting dependence of velocity shown in Fig. 23 have not as smooth behaviour as the other quantities shown there. Therefore, the retrieved behaviour of line-of-sight velocities is not trustworthy and the umbra can be still considered to be at rest.

The description of the umbral structure given above confirms the expected behaviour of plasma quantities there. No surprising or unknown facts are discovered. Therefore, the values of the plasma parameters in the umbra listed in Tab. 3 are hereafter used as the reference magnitudes for the light bridges enclosed by these umbras.

5.2 Penumbra

The average values of plasma quantities from the limbward parts of the penumbras are listed in Tab. 3. These values give us the roughest information about the penumbral structure as they are computed from the whole areas. More detailed information can be seen in Figs. 38–45, where the behaviour of the plasma quantities with regard to the position in the penumbra at six heights is shown, and in Fig. 24, where the continuum intensity is considered. Note that in spite of the umbra, the continuum intensity is not dependent on the position in the penumbra and thus Fig. 24 cannot be interpreted as easily as Fig. 23.

Regarding the irregularity of the sunspot studied in this thesis, the azimuthal averages, which were usually used for the description of the penumbra in previous studies (e.g. Fig 3 taken from Westendorp Plaza et al. 2001a) cannot be created. Moreover, only the parts of the penumbras are observed without the penumbra–quiet sun boundary, and thus the absolute values of plasma parameters, which are highly dependent on the position in the penumbra (that cannot be specified precisely), cannot be compared with previous results. Therefore, the comparison is mainly based on the behaviour of the plasma parameters with the height in the atmosphere and with the distance from the umbra.

5.2.1 General properties

The obtained results are in general in a good agreement with previous studies of the penumbral structure (e.g. Westendorp Plaza et al. 2001a,b; Bellot Rubio et al. 2004; Borrero et al. 2004; Langhans et al. 2005). As can be seen in Figs. 39, 40, 43, and 44 the magnetic field strength is decreasing with the distance from the umbra and becomes more horizontal or even dives back to the sun at some regions far from the umbra. The line-of-sight velocity increases with increasing inclination, i.e. towards the penumbra–quiet sun boundary (Figs. 41 and 45).

From the high-resolution observations is clear, that the structure of the penumbra is filamentary. The widths of the filaments were estimated to be around 160 km (Scharmer et al. 2002) close to their point of origin at the unit continuum optical depth. Also the empirical models (Solanki & Montavon 1993; Martínez Pillet 2000), the theoretical simulations (Schlichenmaier et al. 1998), and the results from the advanced inversion techniques based on the two-component model of atmosphere (Bellot Rubio et al. 2004; Borrero et al. 2004) predict the filamentary structure of the penumbra using the uncombed model. The horizontal flux tubes are embedded in the background field and their diameters are around 100 km (even smaller than the estimates coming from the observations) and therefore well under the resolution limits of the current spectropolarimetric observations (around 500 km
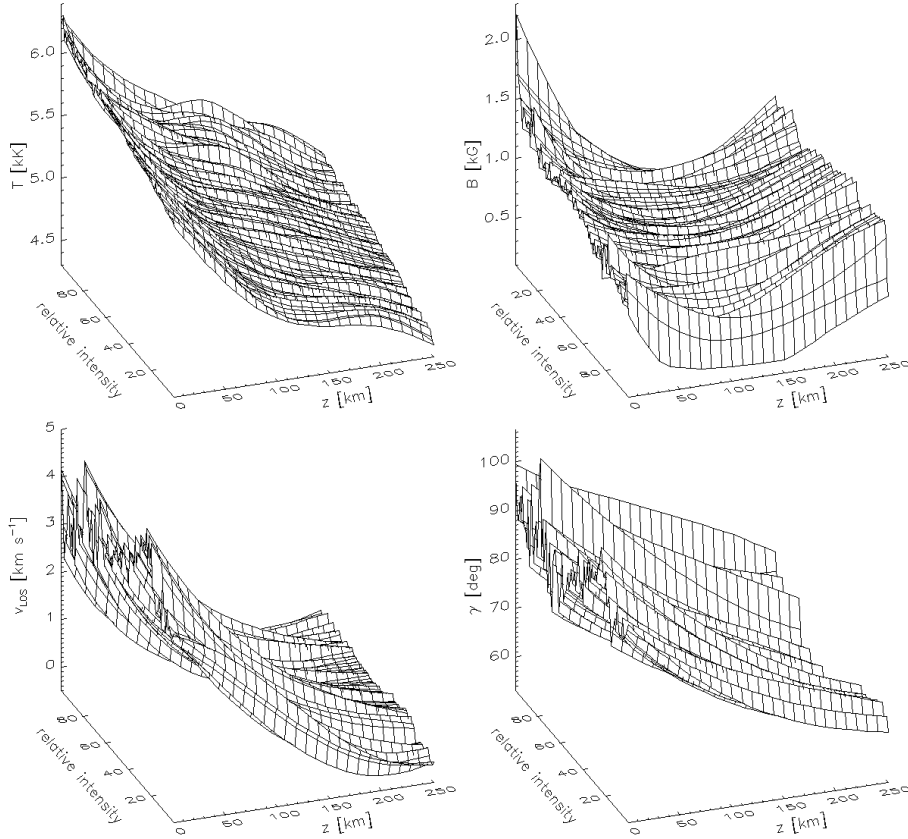
56

Figure 24: Same as Fig. 23, but for the limbward part of the penumbra in the first area.

for measurements analysed in this thesis). However, we see that the resulting maps of the plasma parameters exhibit more or less distinct filamentary structure at all heights with sizes around $1''$ (Figs. 38–45). This fact is consistent with previous observations at lower spatial resolution (Westendorp Plaza et al. 2001a,b; Sánchez Cuberes et al. 2005) and indicates a possible large-scale spatial modulation of the plasma parameters in the penumbra.

The theoretical and empirical models predict, that the flux tubes are positioned in the low layers of the penumbral photosphere and the high layers contain only the background component. With the fine height resolution (that the inversion code possesses), one can expect, that the filamentary structure of the resulting plasma parameters will be restricted only to the low layers. As is said above, this is in the contradict with the results. The best examples of the filamentary structure of the penumbra are the resulting maps of the temperature (Figs. 38 and 42) and the inclination in the second area (Fig. 44). It is clearly shown, that the filaments are narrowest at the lowest layers of the atmosphere and they are diffusing in the case of the

57

inclination and diminishing in the case of the temperature.

There are two explanations for these filaments at high layers. Either they are real or they are artifacts of the inversion code. There are some properties of the inversion code SIR which infirm the verity of such structures. As was shown by Borrero et al. (2004), even the one-component inversion can be used for the analysis of the unresolved structures. It can be expected, that the ratio between the background and the flux tube component is changing from one resolution elements to another in the penumbra and thus influencing the resulting values of plasma parameters. This argumentation can explain the filamentary structure at low layers.

On the other hand, the height resolution of the inversion code SIR seems to be fine enough to reveal the expected sizes of the flux tube, as the atmospheric parameters are evaluated with step of $\log \tau = 0.1$ (corresponds roughly to 15 km at low photosphere). But the exact height resolution is dependent on the number of nodes. Therefore, only the temperature has enough nodes in the analysed region of heights to resolve the layers of the atmosphere which are intruded with the flux tubes and which are not. On the other hand, the inclination has only one node and the magnetic field strength has two nodes in the analysed region of heights (0–250 km) and the values of these plasma parameters are computed by cubic splines at all other heights. It means, that the plasma quantity can be evaluated at the height of the first node, where the flux tube component can prevail at some resolution elements and thus the filamentary structure is retrieved. The second node above this one is already at height, where only the background component is present, and the maps of the plasma parameters are theoretically smooth. As the values of the plasma parameters are computed by cubic splines between these two nodes and the upper values are possibly the same everywhere, then the differences between the filaments should be decreasing. Exactly this behaviour can be seen in Figs. 28 and 29 in Sect. 5.2.3. The mechanism described above also explains why the filaments at high layers of the atmosphere are much more distinctive in the inclination and magnetic field strength maps than in the temperature maps.

Another interesting feature are the differences of the absolute values of plasma parameters between the limbward and discward parts of the penumbra, as can be seen in Figs. 43–45. As the observed areas are highly irregular, these discrepancies can be just apparent. However, Westendorp Plaza et al. (2001a) obtained similar results, i.e. higher values of inclination and line-of-sight velocity in the limbward parts of the penumbra in the case of a regular sunspot. He interpreted these differences as the consequence of the "differential opacity effect", i.e. different geometrical heights are probed on each side of the penumbra at a given optical depth. Martínez Pillet (2000) has shown that the difference in geometrical height would be only a few km and proposed another explanation based on the geometrical configuration of the uncombed field. It is difficult to estimate the influence of this effect

in case of an unconnected and irregular parts of the limbward and discward parts of the penumbra, but the possibility of this effect must be taken into account to avoid wrong conclusions.

The most evident is the discrepancy in the case of the line-of-sight velocity (Fig. 45), which has a simple explanation since this parameter is not evaluated with respect to the local vertical. If the Evershed flow is symmetric, as can be supposed, then the absolute values of the line-of-sight velocities would be the same only if the flow is exactly horizontal. All other values of inclination would mean different projection angles from the limbward and discward parts of the penumbra to the line of sight and thus result into the asymmetry of the velocity values. Using the values of inclination, the component of velocity along the magnetic field lines can be computed, but such process emphasises the values of inclination which are more uncertain than the line-of-sight velocities themselves and is not implemented. Nevertheless, this process is used in Sect. 5.2.3 to explain some characteristics of the line-of-sight velocity fine structure.

Although the plots in Fig. 24 are based on the values from the limbward part of the first penumbra only, they are quantitatively the same as analogous plots from the second penumbra. The most evident behaviour of the plasma parameters with height is the restriction of the line-of-sight velocities to the low layers of the photosphere, as is shown in the lower left part of Fig. 24. This was predicted by the theoretical (Schlichenmaier et al. 1998) and empirical models (Solanki & Montavon 1993; Martínez Pillet 2000), since the Evershed flow is almost horizontal (see e.g. Tritschler et al. 2004, and references therein) and must follow the magnetic field lines. The magnetic field is expected to be horizontal only in the flux tubes, which are also restricted to low layers. However, the behaviour of the line-of-sight velocity corresponds to the model of the embedded flux tube only in the case of general point of view. In Sect. 5.2.3, the results in favour of the model of the rising flux tube are discussed along with the results which are not supporting this model.

To estimate the reliability of the resulting values of velocity, the line-of-sight velocities were computed from the shifts of the Stokes I profile of both lines (Jurčák et al. 2003). In Fig. 46 (Colour plates) are shown the results for the first and second area (left and right columns respectively), whereas the first row corresponds to the line-of-sight velocity derived from the Fe I line at 630.15 nm and the second row to 630.25 nm. Before the penumbral velocities are studied, it must be noted, that the umbral velocities obtained by this method are close to zero as expected.

The results confirm the expected redshift on the limbward part of the penumbra and blueshift on the discward part. The asymmetry between the limbward and discward part of the second penumbra is also present, i.e. higher absolute values of velocity in the limbward part. The position of the maximal and minimal values of the velocity is comparable with the velocity
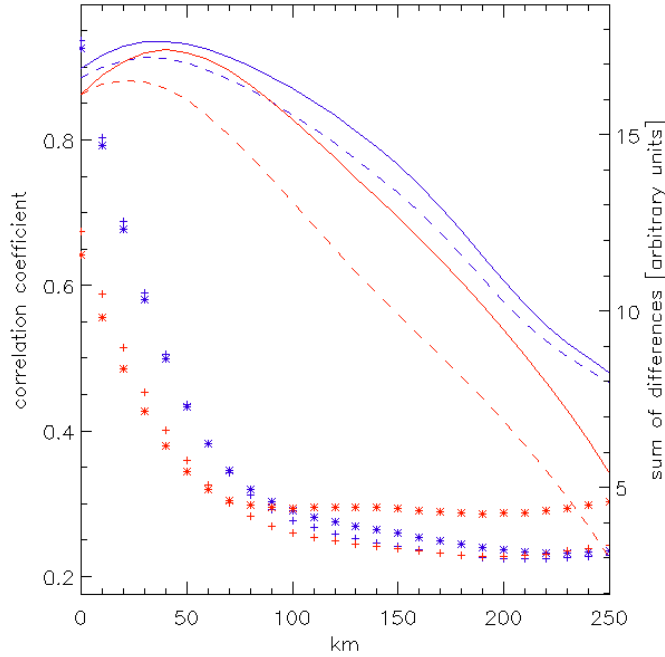
59

Figure 25: The correlation coefficients between the line-of-sight velocities derived from the shifts of Stokes I profiles and velocities obtained by the inversion code SIR (lines) are plotted along with the sum of differences between the absolute values of these velocities (symbols). The blue and red lines (symbols) correspond to the first and second area respectively. Solid lines and plus signs correspond to the Fe I 630.15 nm, dashed lines and asterisks to 630.25 nm.

maps shown in Figs. 41 and 45, although the absolute values of velocity obtained by this method are much smaller than those from the SIR code.

These velocities are computed almost from the whole line wings, and therefore it is impossible to specify the average height which is mainly responsible for the obtained value of the line-of-sight velocity. Therefore, the correlation coefficient between these maps of velocities and those retrieved by the SIR code at studied heights were computed along with the sum of differences between the values. The results are shown in Fig. 25, where the blue and red lines (and symbols) correspond to the first and second area respectively. The solid and dashed lines correspond to the correlation coefficients computed using Fe I 630.15 nm and 630.25 nm respectively. The plus sign corresponds to Fe I 630.15 nm and the asterisk to Fe I 630.25 nm. The maximal correlation coefficients are reached at heights between 20–40 km, but the sum of differences is elevated at these heights. Coming out from this figure, the values of the line-of-sight velocities retrieved from the SIR code are probably overestimated at low layers of the atmosphere and become

reliable at heights around 50 km.

In the upper left part of Fig. 24, the behaviour of the temperature with regard to the continuum intensity and the height in the atmosphere is shown. The dependence of temperature on the continuum intensity is thoroughly discussed in the next section. The temperature decreases on average faster with height in the penumbra than in the umbra, as suggests the temperature gradient computed from the values in Tab. 3, which is higher in the penumbra (4.42 K km^{-1}) than in the umbra (3.35 K km^{-1}). This can be also explained with the presence of the hot flux tubes, which increase the temperature more at the lower layers than in the upper parts of the analysed region.

The behaviour of the magnetic field strength with height is heavily influenced by the presence of the unresolved fine structure. The correlation with continuum intensity is discussed in next section, but regardless the intensity we see (upper right part of Fig. 24), that the magnetic field strength is decreasing with height everywhere and from some geometrical height increasing again. It seems, that the turning point is dependent on the continuum intensity, it is around $z = 100$ km at the darkest parts and roughly 150 km in the brightest parts. To explain this behaviour, the model by Schlichenmaier et al. (1998) is assumed. The rising flux tubes have smaller magnetic field than the background component. In bright areas, these tubes are rising and reaching there higher layers of the photosphere and then they become dark and horizontal, and according to Schlichenmaier et al. (1998) they remain roughly 100 km above the unit continuum optical depth. This is in a good agreement with the behaviour of the magnetic field strength. On the other hand, it would mean that the inclination should be smaller in the bright areas than in the dark ones, because the average inclination of the rising flux tube mixed with the background field should be smaller than the inclination of the lying horizontal flux tube mixed with the background field. In the lower left part of Fig. 24 is shown, that some dark parts of the penumbra have higher inclination than the brightest areas at the lowest layers, but the difference is very small. Moreover, the large uncertainties infirm the values of inclination mainly at lowest layers which are compared here. This problem is again discussed locally in Sect. 5.2.3

The presence of the flux tubes, which are probably restricted only to the low layers, makes it difficult to estimate the characteristics of the background component. Therefore it is hard to say, if the magnetic field strength of the background component is increasing with height or not. Note, that the retrieved increase in the magnetic field strength continues also at higher layers than are those shown in Fig. 24, and thus agrees with Westendorp Plaza et al. (2001a), who found a decrease in the magnetic field strength in the inner penumbra and an increase in the outer penumbra (left part of Fig. 3) and interpreted it as a sign of a canopy structure. The absolute values of the inclination of the magnetic field in the background component

are also unknown, since the presence of the flux tubes at low layers affects the obtained values of inclination at high layers more than it influences the magnitudes of the other plasma parameters (according to the lowest number of nodes for inclination). Following the argumentation about the inclination in the umbra given in Sect. 5.1, the inclination should be decreasing with height as is shown in the lower left part of Fig. 24 even if the resulting stratifications are not influenced by the flux tube component.

The azimuth of the magnetic field is shown only in maps of the magnetic field strength (Figs. 39 and 43). The errors of this parameter are even larger than the errors of the inclination. Moreover, the 180° ambiguity of the azimuth values further infirm the reliability of this parameter. The orientation of the magnetic field corresponds to the orientation of the penumbral filaments. The azimuths in the discward part of the second penumbra seem to be quite unorganised mainly at the low layers, where the uncertainties are largest. The opposite orientation of some of the arrows would be more suitable in this region. This can be ascribed to the method used for the solution of the ambiguity problem, but even if opposite orientation of the magnetic field is considered, the resulting values are not aligned in this region. As only one discward part of the penumbra is analysed, it cannot be said why are the resulting values of the magnetic field azimuth so dispersed only there and what could be the cause for this.

5.2.2   Correlation coefficients

In Fig. 26, the correlation coefficients between the continuum intensity and various plasma parameters in different penumbral regions are shown with regard to the height in the atmosphere. Note, that the main cause for the discrepancy between the values of the correlation coefficients in different areas is the different range of distances of the points in the penumbra from the umbra. The dependence of the correlation coefficients on the position in the penumbra was already pointed out by Westendorp Plaza et al. (2001a) as is shown in Fig. 4 on the correlation coefficient between the magnetic field strength and the inclination.

It is clear that only the temperature has a clear relation to the continuum intensity. Why the other plasma quantities have only a weak relation to the continuum intensity? There are some reasons for the small correlation between the intensity and the plasma parameters. The first argument regards only the temperature. This parameter was computed with the highest number of nodes, so there are some enhancements in the temperature stratifications, which can be seen at some intensities in the upper left part of Fig. 24. These enhancements cause the decrease of the correlation coefficient at the heights in the atmosphere where they are present. Therefore, only the correlation coefficients of temperature in Fig. 26 show oscillatory behaviour with height. Such temperature enhancements can have the same
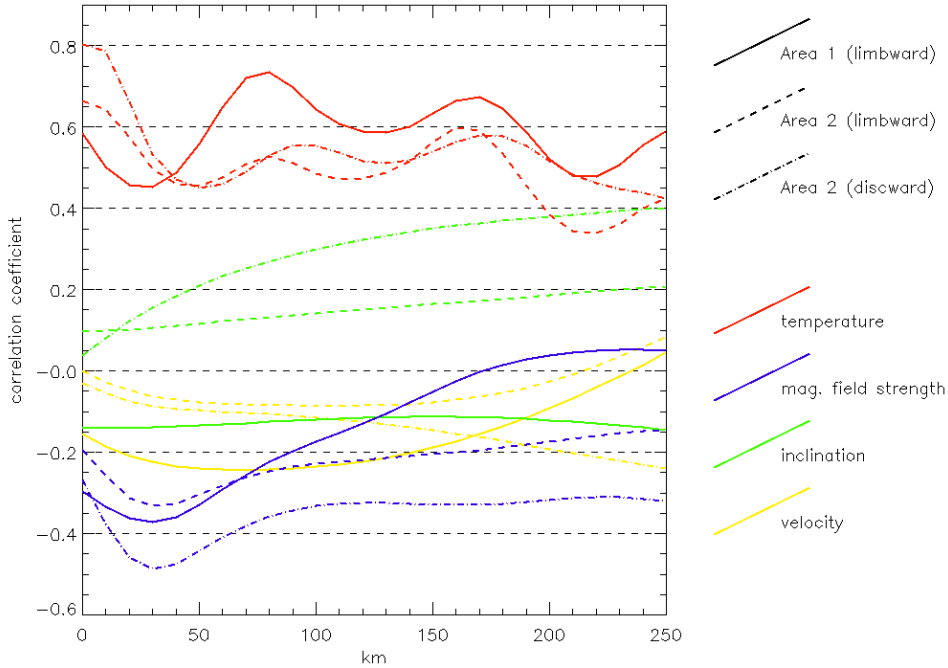
Figure 26: The correlation coefficients between the continuum intensity and temperature, magnetic field strength, inclination, and line-of-sight velocity respectively. The colours of the lines correspond to different plasma quantities and the styles of the lines to the different parts of the penumbra as is explained in the right part of the figure.

reason as the one shown in Fig. 20, i.e. too high number of nodes for this plasma parameter. However, the spatial and height arrangement of these enhancements seems to be organised and they are discussed in the next section.

Other argument regards the correlation coefficients of all studied plasma parameters. It was suggested by Schlichenmaier et al. (1998) that the dark parts of the penumbra consist of two components. Even if the model proposed in their work is not correct, the white-light observations of the penumbra show the appearance of spatially unresolved clusters of penumbral grains with the tail which gradually darkens with the distance from the umbra until it is not recognisable from the surroundings. It can be easily supposed, that the physical conditions in this darkened tail differ from the dark parts of the penumbra where no tails are presented and thus different values of plasma quantities correspond to similar continuum intensities. Also the bright areas can have different plasma conditions, since the areas occupied by slightly darkened bunch of flux tubes and those occupied by the smaller amount of rising flux tubes would have comparable continuum intensities.

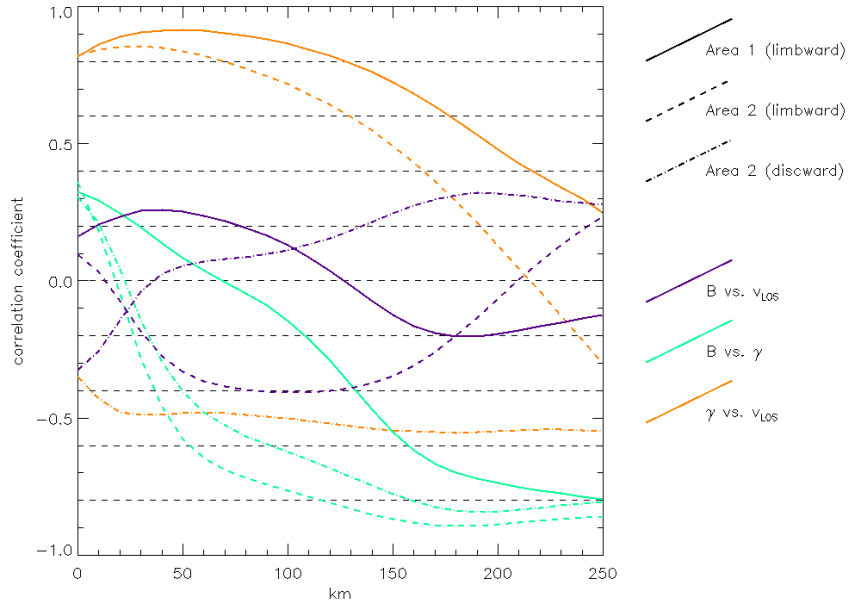Some weak anticorrelation between the continuum intensity and mag-

63

Figure 27: The mutual correlation coefficients between magnetic field strength, inclination, and line-of-sight velocity. The styles and colours of the lines are explained in the right part of this figure.

netic field strength can be found in Fig. 26. This anticorrelation is restricted to low layers of the photosphere in the case of the first penumbra (solid line). It means that the magnetic field is stronger in the darker parts of the penumbra as can be seen in the upper right graph of Fig. 24 (note the inverse orientation of the y axis which indicates the continuum intensity). Similar dependence of the magnetic field strength on the continuum intensity was found be e.g. Beckers & Schröter (1969) and Wiehr (2000), but recent studies by Westendorp Plaza et al. (2001a) (same inversion technique applied on data with moderate spatial resolution) and Langhans et al. (2005) (analysis based on the magnetograms with higher spatial resolution) found stronger magnetic field in bright filaments in contradiction. Our result supports the model of the rising flux tubes computed by Schlichenmaier et al. (1998), as already mentioned in the previous section.

In Sect. 5.2.3, this problem is discussed in more details along with the local dependencies of the inclination and the line-of-sight velocities, which do not show any strong global correlation with continuum intensity. Although, slightly higher values of correlation between the continuum intensity and inclination can be found at high layers of the discward part of the second penumbra.

In Fig. 27 are shown the mutual correlation coefficients between the magnetic field strength, the inclination, and the line-of-sight velocity. These cor-

relation coefficients are not influenced by the argument listed above. Note, that the correlation coefficients that consider the line-of-sight velocity loose their meaning with increasing height, as the velocity is decreasing to zero with height and the uncertainties dominate at high layers.

The most evident is the correlation between the inclination and the line-of-sight velocity in the limbward parts of the penumbras and a weaker anti-correlation in the discward part of the second penumbra. This behaviour fits the expected configuration of rising flux tubes suggested by Schlichenmaier et al. (1998), where the Evershed flow is carried only in the flux tubes. The flow is slowest near the emerging point of the flux tube and becomes faster with increasing distance from this point, where the tube is theoretically horizontal. In our case, the angle between the line of sight and normal to the surface is $25°$. If we suppose the inclination of the rising flux tube to be e.g. $70°$, what is around the minimal value of inclination obtained at low layers, than the projection of the velocity to the line of sight is obtained by multiplying this velocity with factor $\cos 95°$ (0.09) on the limbward side of the penumbra and $\cos 45°$ (0.7) on the discward part. With increasing inclination, this factor is increasing on the limbward side and decreasing on the discward side of the penumbra. If we realise, that the redshifts on the limbward part of the penumbra have positive sign and the blueshifts negative sign, than it results into the strong correlation between the inclination and the line-of-sight velocity on the limbward side and the weaker anticorrelation on the discward side of the penumbra. Note, that the decrease of the coefficients with increasing inclination (i.e. increasing distance from the umbra) on the discward side of the penumbra is more than compensated by the increase of velocity with the increasing distance from the umbra. Similar results were already found by Westendorp Plaza et al. (2001b), i.e. the fastest flow is associated with areas, where the field lines are diving back to the sun.

The anticorrelation between the magnetic field strength and the inclination becomes significant at high layers, i.e. the strong magnetic field is more vertical there. This fact is consistent with the uncombed model of the penumbra, where the background component is stronger and more vertical. This anticorrelation is apparent at high layers, because neither the magnetic field strength nor the inclination have sufficient height resolution to compensate the presence of flux tube at low layers. It must be noted, that the anticorrelation is not obtained at low layers, where the more vertical field can be found also at areas with weak magnetic field (see the next section).

The correlation coefficients between the magnetic field strength and the line-of-sight velocity do not exceed the absolute value 0.4. Moreover, the correlation coefficients of these parameters computed from the limbward parts of the penumbras do not show similar behaviour, which should be opposite to the behaviour of the correlation coefficient from the discward part of the second penumbra like in the case of the correlation coefficient

between the line-of-sight velocity and the inclination. Therefore, the relation between the magnetic field strength and the line-of-sight velocity is discussed only with regard to the fine structure of the penumbra.

5.2.3 Fine structure

In previous sections, some indirect evidences for the flux tubes, which are restricted to low layers of the photosphere and spatially unresolved, are discussed. The general results also support the theoretical model of the rising flux tubes by Schlichenmaier et al. (1998). The local properties of the penumbra are closely studied in this section.

In Figs. 28 and 29, the behaviour of plasma parameters along vertical cuts through the limbward and discward parts of the second penumbra are shown. The colours of lines in the plots of temperature, magnetic field strength, inclination, and line-of-sight velocity correspond to the different heights in the photosphere as explained on the right side of these figures. The dashed black line in all of the graphs corresponds to the continuum intensity along the cuts. On the x axis is shown the horizontal length of the cuts, where the spacing between the minor ticks is 500 km which roughly corresponds to the spatial resolution of our observation. The position of the cuts is marked in the upper right part of these figures, where the arrows correspond to the dashed lines in the graphs of plasma parameters. These lines correspond to local minima and maxima of the continuum intensity and are used as reference points for the orientation in the graphs. The lines are enumerated from left to right, e.g. the second line corresponds to the local maximum of the continuum intensity in Fig. 28 and to the local intensity minimum in Fig. 29.

In the previous section is claimed that the correlation coefficients are decreased because similar values of plasma parameters are reached in areas with completely different continuum intensities. This can be seen in graphs of the inclination in Figs. 28 and 29, where the low values of inclination are found both in the darkest and brightest areas (compare e.g. the second and sixth line in Fig. 28 which corresponds to the intensity maximum and minimum respectively). The magnitude of the fluctuations between bright and dark filaments is decreasing with height, as can be seen in graphs of the magnetic field strength, inclination, and line-of-sight velocity. As is explained in Sect. 5.2.1, the insufficient height resolution for these parameters can be the explanation for the filamentary structure at high layers.

The differences between the two kinds of the dark components (Sect. 5.2.2) are easily seen in graphs of magnetic field strength and inclination. In Fig. 28, the fourth and sixth lines correspond to the deep minima of continuum intensity, the first one being deeper. The inclinations are comparable at high layers of the atmosphere and so are the magnetic field strengths. On the other hand, the low layers of atmosphere exhibit different values
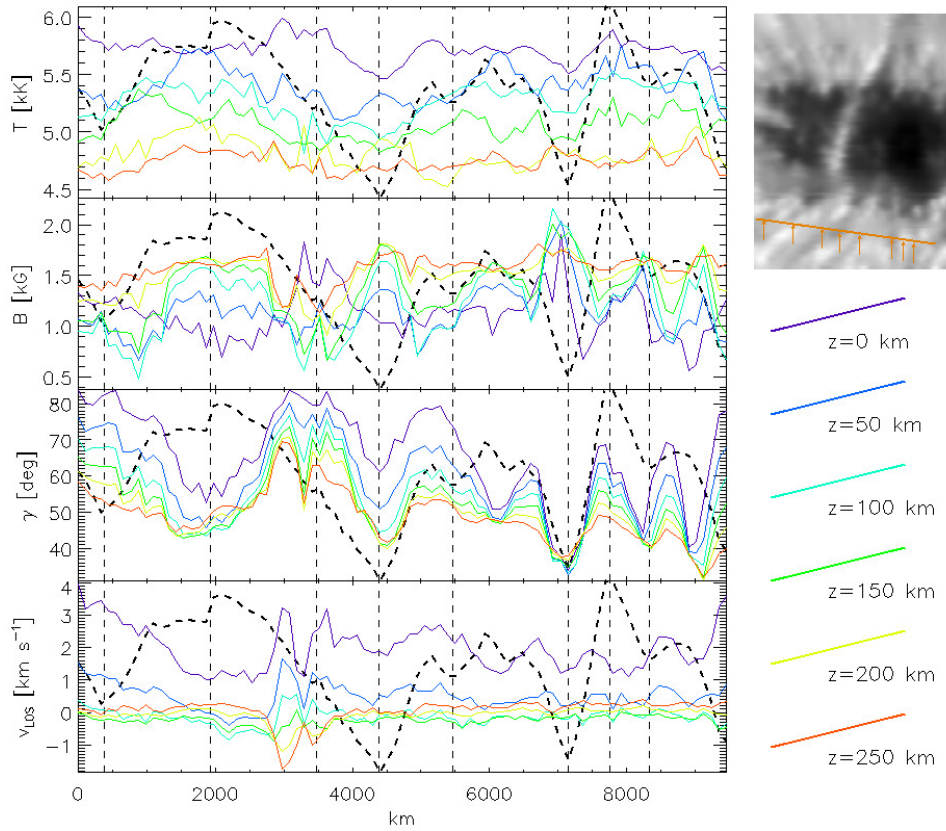
Figure 28: The behaviour of temperature, magnetic field strength, inclination, and line-of-sight velocity along the vertical cut through the limbward part of the second penumbra, which is marked in the upper right part of this figure. Detailed description is given in the text.

of these atmospheric parameters. In agreement with Schlichenmaier et al. (1998), the dark area around 4400 km can be associated with the darkened tail of the flux tube, as the inclination is high and the magnetic field weak at low layers. The background component dominates in the dark region around 7200 km, as the inclination and magnetic field strength are almost the same at all heights in the analysed region of atmosphere. The difference should be observable also in the case of the line-of-sight velocities at low layers. The velocity is high at the first intensity minimum at the geometrical height $z = 0$ km as suggests the models of the flux tubes, but the absolute values of velocity are not trustworthy at this layer. At $z = 50$ km, the line-of-sight velocity is still higher at the first intensity minimum than at the second one, but the difference is only 0.3 km s^{-1} which is only slightly more than the uncertainties at this layer.

No significant example of the darkened tail can be found in the dis-
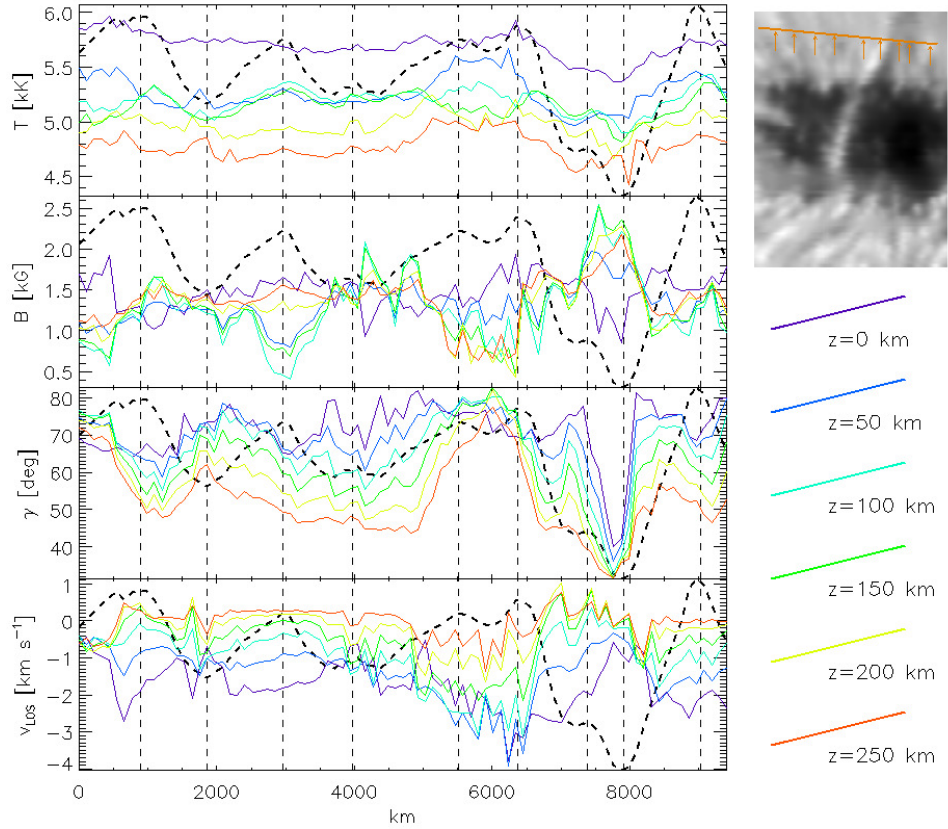
67

Figure 29: Same as Fig. 28, but for the discward par of second penumbra.

cward part of the second penumbra (Fig. 29). This does not mean, that the model is wrong, just that the background and flux tubes components are comparable in the resolution elements inside the dark areas along the cut. The background component dominates in Fig. 29 around the eight line (8000 km), where the small values of line-of-sight velocities and inclinations can be seen at all studied heights and the magnetic field is the most intense there.

This separation of the background and flux tube component enables the comparison with the results obtained by the two-component inversion made by Bellot Rubio et al. (2004) and Borrero et al. (2004). Although the background component is also changing with the distance from the penumbra, the values of inclination smaller than 40° found in areas where the background component dominates corresponds to the values found by Borrero et al. (2004) and Bellot Rubio et al. (2004) (inner penumbra). The magnetic field strength obtained in these areas (around 1800 G) is also in a good agreement with these studies, although the field strength is much more dependent on the position in the penumbra and thus hardly comparable.

68

Regarding the line-of-sight velocity, it is better to look for the increased values of velocity at higher layers, since the values at $z = 0$ km are overestimated, as explained in Sect. 5.2.1. In Fig. 28, it corresponds to the bright areas around 1000, 5000, and 8500 km. In the white-light image of this figure can be seen that these areas correspond to extensions of bright grains. The spatial correspondence between the bright filaments and the flow channels was found also by Hirzberger et al. (2005). All these regions have very similar stratification of all shown plasma parameters. The temperatures at $z = 50$ km and $z = 100$ km are close to each other. The magnetic field strength decreases from $z = 0$ km to $z = 50$ km, than remains almost constant and increases from $z = 100$ km to $z = 250$ km. The inclination is decreasing with height in these areas. Similar behaviour can be found in Fig. 29 around 3000 km and also around 800 km, but not so evidently. These stratifications of plasma parameters correspond to the existence of the flux tubes located around the heights 50–100 km.

In Fig. 28, the second arrow points roughly to the border between the bright grain and some darker background. According to Schlichenmaier et al. (1998), the flux tubes are rising in bright grains. The resulting values of inclination are low and close to each other at all heights. If the flow is carried by the rising flux tube, than the projection to the line of sight would result into the negative values of velocity which can be seen around 2200 km with maximum at the geometrical depth 100 km (in agreement with Hirzberger et al. 2005). On the other hand, such configuration should result into weaker magnetic field at this height which is not confirmed, as the value is comparable with the magnetic field strength at $z = 250$ km.

The area around 3000 km in Fig. 28 was not described earlier on purpose, because very strong and improbable flows were obtained there. Strong flows at highest layers are also obtained in the discward part of the penumbra (Fig. 29 around 6000 km), but this area is closely related to the extension of the light bridge to the penumbra and a strange behaviour can be expected there. Such extension is not observed in the continuum intensity on the limbward part of the penumbra. Therefore, the retrieved stratifications in this area are considered as wrong, also because such strong oppositely oriented flows are highly doubtful.

The last interesting area mentioned in previous paragraph is located in the discward penumbra located around the sixth line in Fig. 29. Although the line-of-sight velocities are significant also at highest layers, no shear in the orientation of the flow is presented and makes the results more trustworthy. From the white-light image is clear, that the area spatially corresponds to the extension of the light bridge to the penumbra. The temperature stratification is not unusual in this region, a smooth decrease with height, only the absolute values of temperature are higher than in the surrounding areas at some layers. The magnetic field is weak in this region, but surprisingly it is decreasing with height and the field strength remains low at high
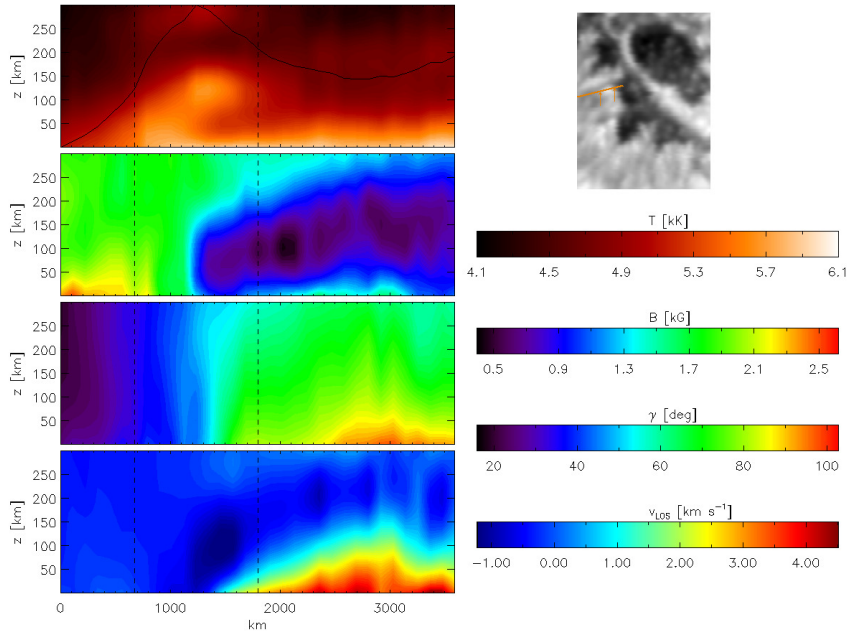
Figure 30: The behaviour of temperature, magnetic field strength, inclination, and line-of-sight velocity in the vertical cut along the bright filament in the limbward part of the first penumbra (marked in the upper right part of this figure). Detailed description is given in the text.

layers. The peculiarity of this behaviour becomes clear, if we compare it with the stratification of magnetic field strength in the light bridges, which is described in Sect. 5.3. The magnetic field is almost horizontal at all layers and the flow velocity is decreasing with height. The formation of this structure must be closely related to the formation of the light bridge, but in the penumbra is moreover influenced by the rising flux tubes.

In Figs. 30 and 31, the vertical cuts through the bright grains are shown. Both figures start in the umbra, cross the grain and continue towards the quiet sun as shown in the upper left part of these figures. The arrows correspond to the dashed lines in the plots of temperature, magnetic field strength, inclination, and line-of-sight velocity (named from top to bottom). The colorbars in the left part of the figures enable to estimate the magnitudes of plasma quantities. The solid black line in the temperature plot corresponds to the continuum intensity along the cut.

We try to interpret the previous results with the model of rising flux tube as was proposed by Schlichenmaier et al. (1998). Although there are other models for the filamentary structure in the penumbra which can explain our results, Figs. 30 and 31 closely resemble the theoretical maps of plasma parameters shown by Schlichenmaier et al. (1998). Therefore, this theoretical
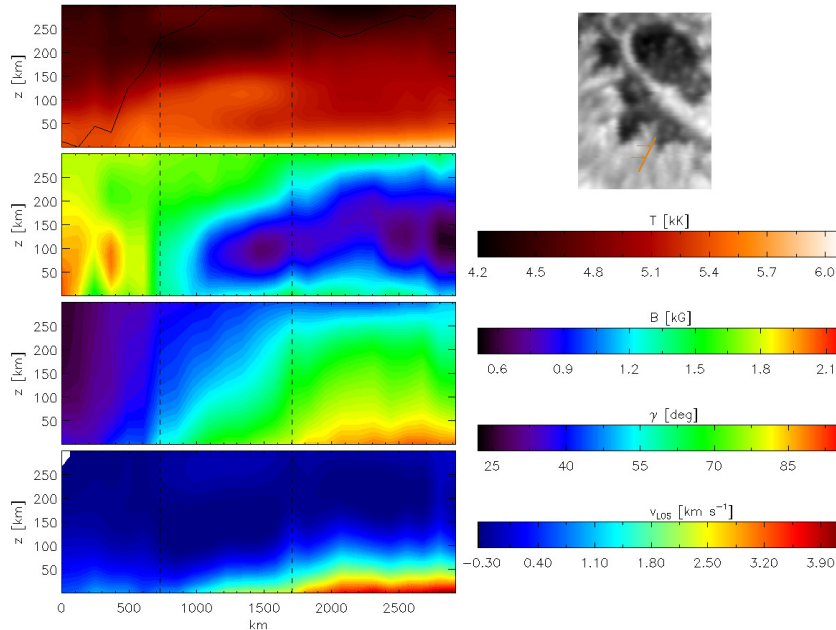
Figure 31: Same as Fig. 30, but for a different bright filament.

model of the filamentary penumbra is preferred for the comparison with our results.

The temperature along the cut shows the rising hot flux tube, which is rapidly cooled down to the temperature of the surrounding plasma and becomes horizontal. However, this cool flux tube can be followed in the plot of magnetic field strength, as the field is weaker inside it. The flux tubes seem much broader in the maps of magnetic field strength than in the temperature maps. This is caused by the different height resolution, i.e. different numbers of nodes for these plasma parameters.

It must be mentioned here that we detect rather a bunch of rising flux tubes than a single one. With our spatial resolution around 500 km a single tube would be unrecognisable. In fact, we observe a part of penumbral atmosphere penetrated by rising flux tubes with filling factor sufficiently high to give their signature to the observed Stokes profiles.

The presence of the flux tube is indistinguishable in the map of the inclination, as the height resolution is lowest for this quantity. In places of the flux tube, which can be estimated from the magnetic field strength map, the inclination reaches values around 70° from 2000 km further. The inclination can be also estimated from the tracing of the weak field in the magnetic field strength map and reaches roughly 80° in this region. The difference of 10° is comparable with the uncertainties of inclination at these layers of atmosphere.

71

Surprisingly, the flux tubes cannot be identified in the maps of line-of-sight velocity, although the height resolution is the same as for the magnetic field strength. Strong velocities are restricted to the lowest layers of the atmosphere, but only in places, where the flux tube is already horizontal (i.e. 2000 km in the case of Fig. 30 and 1800 km in Fig 31). In Fig. 30, the negative velocities (upflows) spatially correspond to the location of the rising flux tube, which is again in agreement with the model by Schlichenmaier et al. (1998).

5.2.4   Conclusions

Three incomplete parts of the penumbra are analysed, where two of them are located on the limbward side of the sunspot. The studied parts of the penumbra are highly irregular, which makes it difficult to compare the absolute values of plasma parameters with previous results, as the magnitudes of the plasma quantities are highly dependent on the position in the penumbra.

Nonetheless, the spatial behaviour of the plasma quantities is in a good agreement with previous studies. The magnetic field becomes weaker and more horizontal with increasing distance from the umbra at all heights. The line-of-sight velocities are in general increasing with increasing distance from the umbra and are restricted to low layers of the atmosphere.

It is shown, that the analysis of the correlation coefficients between the continuum intensity and plasma parameters is difficult, since the dark parts of the penumbra consist of at least two components with completely different plasma behaviour. The clear correspondence is found only between the continuum intensity and the temperature. With agreement with older studies and in contradict with recent analyses, weaker magnetic field is found in brighter areas. Strongest anicorrelation between these two plasma quantities is found in the discward part of the second penumbra, which is on average the closest one to the umbra, and thus the dark parts there correspond mostly to the background component, where the magnetic field is strong, and not to the darkened tail of the bright filaments with reduced magnetic field.

The correlation between the line-of-sight velocity and the magnetic field inclination confirms the results obtained for the first time by Westendorp Plaza et al. (2001b), i.e. the fastest flows are found in regions, where the field lines are diving back towards the solar surface. The anticorrelation between the magnetic field strength and the inclination confirms the uncombed configuration of the penumbral magnetic field.

Although the expected sizes of the penumbral fine structure are well under the spatial resolution of the observations analysed in this thesis, the filamentary structure is detected (Westendorp Plaza et al. 2001a observed similar structures and call them spine/interspine corrugation). It is possible to reveal the unresolved structure even if one-component model of atmo-

72

sphere is used, since the ratios between the filling factors of two (or even more?) components are changing from one pixel to another and thus the average Stokes profiles from these areas are different and result into different stratifications of plasma parameters. The found widths of the filamentary structures are broader than those observed in the direct white-light images as they are smeared due to the lower spatial resolution.

The weaker magnetic field is located in bright grains and in the dark areas which can be traced back as the extensions of the bright filaments. The more vertical field is correlated with either the bright grains or with the dark areas filled with the background component (higher magnetic field strength). All of the results regarding the magnetic field configuration, together with the localisation of the temperature enhancements, favour the model of the rising flux tubes suggested in the work by Schlichenmaier et al. (1998).

Due to the height resolution (depending on the number of nodes), the highest values of inclination are not reached at heights where the flux tube is expected. On the other hand, the line-of-sight velocity has the same height resolution as the magnetic field strength, yet, the maximal values of the line-of-sight velocity are not reached at heights of the flux tube, but at lowest layers, where they are most probably overestimated. However, these maxima of the Evershed flow spatially correspond the location of the horizontal pats of flux tubes. In places of the bright grains, the upflows are observed even in the limbward parts of the penumbra (in agreement with Schlichenmaier et al. 1998). Note that Borrero et al. (2004) found the maximal velocities around $\log \tau = -1$, the result which supports the location of the flux tubes around this height in the penumbra and which is not confirmed by our stratifications of the line-of-sight velocity.

5.3   Light bridges

The configuration of the magnetic field and the temperature properties in the analysed light bridges are discussed in the article by Jurčák et al. (2006). The results presented there are almost the same as those discussed here, although in several cases different methods were used in the data reduction.

5.3.1   General properties

The average values of the plasma parameters in the light bridges are listed in Tab. 3, where the values for the narrow light bridge represent the averages from the light bridge in the second area (LB2) and the narrow part of the light bridge in the first area (LB1, orange contours in Fig. 9). In case of the broad light bridge, the values are computed from the rest of LB1 (red contours in Fig. 9). The general properties of the light bridges can be also estimated from Figs. 38–45. Since the whole light bridges are observed, the absolute values of various plasma quantities are comparable with previous

73

works on light bridges.

Previous results concerning the temperature in the light bridge region were presented in the article by Rüedi et al. (1995), who studied the change in temperature along one cut through the light bridge structure and found a temperature around 6400 K in the LB centre and a difference between the light bridge and the surrounding umbra of around 1500 K (all these values referred to $\tau_{1.56\mu m} = 1$).

The temperature values inferred by the SIR code are on average lower than those in the infrared, which forms deeper in the atmosphere. As can be seen, the temperatures are decreasing with height in the atmosphere as everywhere else reaching the highest values at $z = 0$ km. On average (Tab. 3), the narrow light bridges are only 240 K cooler than the broad light bridge at the unit continuum optical depth, but note that the cental parts of the broad light bridge reach maximal temperatures around 6300 K. The temperature gradient with height and also the average absolute values of temperature are comparable with the penumbra at low layers in the case of the broad light bridge, but the gradient is smaller at high layers as is shown in Tab. 3. On the other hand, the average temperature gradient of the penumbra at high layers is comparable with the narrow light bridges.

Such a coincidence is only apparent, since the temperature stratifications exhibits enhancements shown e.g. in Figs. 32 and 33 in the next section. These temperature enhancements occur at heights around 100–250 km and the typical magnitude is around 200 K, i.e. higher than the magnitude of the temperature enhancements in the penumbra. Around 70% of the profiles inverted in the narrow parts of the light bridges show the bump at a height around 120 km (similar to that seen in Fig. 33). The situation for the broad part of the first light bridge shown in Fig. 32 is different. In this figure, the bump is higher, nearly 210 km. While 32% of the points inside the bridge show this temperature bump, 37% of the points in broad light bridge show a bump at a height of nearly 130 km, as in the case of the narrow light bridges.

In Fig. 38 can be seen that these two different groups of points are spatially organised inside the broad part of the first light bridge. At the geometrical heights $z = 0$ and 50 km, the highest temperatures correspond to the geometrical centre of the light bridge. However, at the geometrical height $z = 100$ km, the temperature enhancements take effect and higher temperatures are found near the border of the broad light bridge. At this height, a cold temperature island is seen in the middle of the bridge. The temperature inside the island is 4850 K, whereas in the bright rim it reaches 5400 K. As we move to high layers, the points with temperature enhancements are observed closer to the centre of broad LB1, closing down the island mentioned before. The bright regions at this height are as hot as before, near 5400 K. At the highest analysed layer ($z = 250$ km, Fig. 38), the cooler island surrounded by the hotter plasma is not clearly distinguishable. The

origin of such a temperature structure is considered to be related to the canopy topology described in Sect. 5.3.4 and is also discussed in Sect. 5.3.5. Also, it is interesting to note that light bridges are known to have brightenings in the chromosphere representing local heating sources (Berger & Berdyugina 2003). The temperature bumps found here may be thought of as the upper photospheric counterpart to these temperature enhancements.

It is well known that the light bridges harbour magnetic fields with lower strengths and more inclined field lines. Beckers & Schröter (1969) found a decrease in the magnetic field strength of 300 G in a weak light bridge as compared to the surrounding umbra and an increase in inclination $\gamma \geq 5°$. Rüedi et al. (1995) found a difference of the magnetic field strength between the umbra and the light bridge around 1000 G and a difference in inclination around 70° in the light bridge centre. Leka (1997), using a Milne–Eddington inversion (which gives the results equivalent to the height of $\log \tau_{5000} = -1.5$, approximately $z = 200$ km), found a range of decreases in B from 300 G to over 1200 G and increased inclinations, usually by at least 10°.

The results presented in this work show a similar behaviour which is shown in Figs. 39 and 43. One of the most striking features is how the light bridges (defined here as the regions with lower field strengths), in both figures, are seen to become narrower as we move to high layers; this is also evident in Figs. 32 and 33. At high layers, the light bridges are less conspicuous as a field strength gap. Additionally, the field strength increases with height. In the centre of the broad light bridge, the field strength can be as low as 100 G at $z = 0$ km and increases to 700 G at $z = 250$ km. Averaged values are given in Table 3. All parts of light bridges show, almost everywhere, the same trend toward increasing field strength with height. Narrower bridges start from a higher average value at $z = 0$ km (1000 G in Fig. 33), but show the same trend.

In order to check if a field free $z = 0$ km atmosphere would be also compatible for narrow light bridges, the inversions of the light-bridge Stokes profiles were performed with the stray-light profiles, which had various degrees of umbral core contributions (thus using stray light with nonzero Stokes Q, U, and V profiles). Notably, the field strength near $z = 0$ km is reduced considerably, to levels smaller than 500 G (the blue line in the field strength stratification in Fig. 33). This shows that a completely field-free $z = 0$ km condition is not achieved for narrow ($1''$ wide) light bridges. The same procedure applied to the broad light bridge shows zero field strength in the range -20–50 km in the photosphere (see Fig. 32). The other influences of the chosen stray-light profile are discussed in the next section.

In agreement with previous authors, we also observed larger inclinations in both light bridges. At the centre of the broad light bridge at $z = 50$ km, inclinations from 40° to 100° are found (Fig. 40). The tendency for the inclination is to decrease from this height upwards, ranging from 30° to 70° at $z = 250$ km. Averaged inclination values are given in Table 3. The same

tendency is observed in the narrow light bridges albeit with more vertical fields.

As shown in Figs. 32 and 33, the stratifications of the inclination are rather uncertain at $z = 0$ km. The $1 - \sigma$ errors are typically $\pm\ 20°$, which makes it difficult to rely on them. Note also that the field strength is quite low in these regions and thus the inclination looses its meaning.

The azimuth of the field vector in the light bridges is distorted from the trend of the outward fanning field set by the dominating umbral core. The field lines point toward the light bridge structure or along the axis of the light bridge (Figs. 39 and 43). This trend is more evident in the broad parts of the first light bridge. It is interesting to mention that Leka (1997), who observed a larger number of light bridges, found an alignment in several cases between the vector field azimuth and the direction set by the light bridge. The azimuth of the magnetic field is closely discussed in Sect. 5.3.4 with regard to the proposed mechanism of the light bridge formation.

As noted in Sect. 2.2, no systematic effects in the velocity structure of the light bridges were found, as both upflows and downflows are observed in these phenomena. As is shown in Tab. 3, the downflows prevail on average in light bridges at low layers and upflows at high layers. The values of the line-of-sight velocity at $z = 0$ km seem to be overestimated like in the penumbra. On the other hand, similar velocity structures are found by comparing Fig. 46 (line-of-sight velocities determined from the shifts of Stokes I profiles) with Figs. 41 and 45 and thus giving confidence to the values of the line-of-sight velocity retrieved by the SIR code at middle layers.

Rimmele (1997) found evidences for the convective movement in the granular light bridges. We calculated correlation coefficients between the continuum intensity and the line-of-sight velocities in the light bridges. The only significant anticorrelation is found in the case of the broad bart of the first light bridge. Anticorrelation is the sign for the convective motions, as the upflows (negative values) are associated with hot (bright) areas and the downflows (positive values) with dark (cool) areas. The correlation coefficient reaches -0.32 and -0.43 for the line-of-sight velocities computed from the shifts of the line cores of Stokes I profile of the Fe I 630.15 nm and 630.25 nm respectively. If the velocities are taken from the SIR code, the anticorrelation is maximal at the highest layers and crosses the value of -0.3 at the height $z = 120$ km in the case of the broad light bridge. The velocities in the light bridges seem not to be restricted only to low layers, and thus the correlation coefficient does not loose its meaning at highest layers unlike the penumbra.

In the narrow parts of the light bridges, the correlation coefficient does not exceed the absolute value of 0.2, if the velocities are taken from the SIR code. The velocities obtained from the Stokes I profiles are not correlated with the continuum intensity in the second light bridge, but there is a relatively strong correlation in the case of the narrow part of LB1; the coefficient

reaches 0.37 and 0.34 for the Fe I 630.15 nm and 630.25 nm respectively.

The results indicate the possible presence of the convective motions only in the broad part of the first light bridge, where the granular structure is most evident in the white-light image shown in Fig. 7. Although the narrow parts of the light bridges also exhibit the granular structure in the white light, there is no correlation with the obtained velocities. But see the following section for the possible influence of the stray light on the retrieved values of the line-of-sight velocities.

5.3.2 Stray light

The possible influence of the chosen stray-light profiles must be discussed before the mechanism of the light bridge formation is suggested. The stray-light problem is the most significant in the light bridges, since these structures are narrow and surrounded by the umbra. Thus, the general assumption that the stray light comes only from the quiet sun is highly improbable in these areas.

To show the influence of the stray-light profile, the inversions of some particular Stokes profiles observed in the light bridges were computed with different stray-light profiles. The examples of the Stokes profiles and corresponding plasma stratifications are shown in Figs. 32 and 33. In the right part of these figures, the observed Stokes profiles (black lines) are fitted by the inversion code, where the initial sets of parameters are the same except of the stray-light profile. In the right part, the resulting stratifications of the plasma parameters are compared.

In Fig. 32, the Stokes profiles obtained in the broad part of the first light bridge are shown. The fit marked with the red lines is obtained by the standard set of initial parameters, i.e. the stray light is taken only from the quiet sun and the stray-light Stokes profiles Q, U, and V are zero (similarly also in Fig. 33). The blue lines are obtained with the stray light mixed with 20% of the profile taken from the close umbra and 80% of the profile from the quiet sun. Higher contamination with umbral stray light caused a rapid increase of the merit function χ^2 and an improbable stratification of plasma parameters. The stray-light factor of the quiet sun profile reaches typically 25% in the broad parts of the light bridge and is only slightly higher (35%) for the stray-light profile contaminated with the umbral profile. The resulting stratifications of the plasma parameters do not change substantially in the broad light bridge.

In the case of the narrow light bridge (Fig. 33), the blue fits and stratifications are obtained by using the stray-light profile only from the surrounding umbra, because there was no significant increase of the merit function in this case. However, the stray-light factor is increasing with increasing contamination with the umbral profile reaching the unreasonably large value of 60% in the case of the stray light only from the umbra, which is much larger
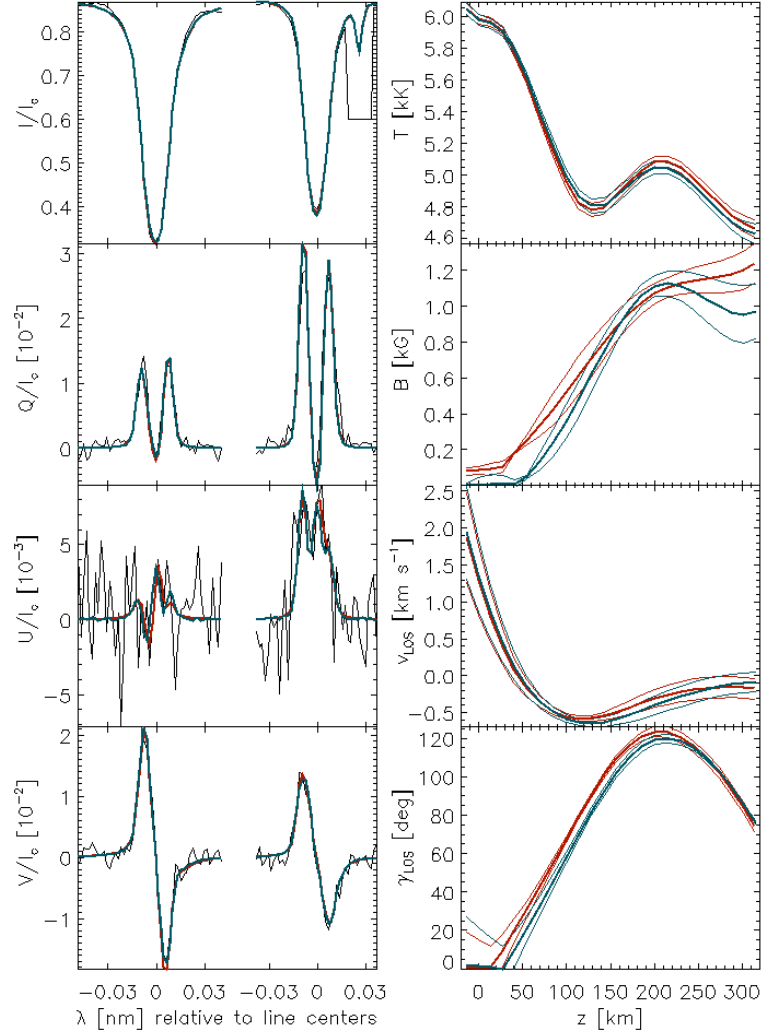
Figure 32: The Stokes profiles observed in the broad part of the first light bridge (black lines in the left part) are fitted by the inversion code with two different stray-light profiles: quiet sun only (red lines) and quiet sun with 20% umbral contribution (blue lines). The resulting fits corresponds to the red and blue profiles in the left part and different stratifications of the temperature, magnetic field strength, inclination, and line-of-sight velocity in the right part.

than the stray-light factor of the standard profile of the stray light (20%).

As is already described in the previous section, the increase in the fraction of the umbral component in the stray-light profile causes a decrease in the magnetic field strength at almost all heights and a slight increase in the formation height of the canopy structure (see Sect. 5.3.4). But the main
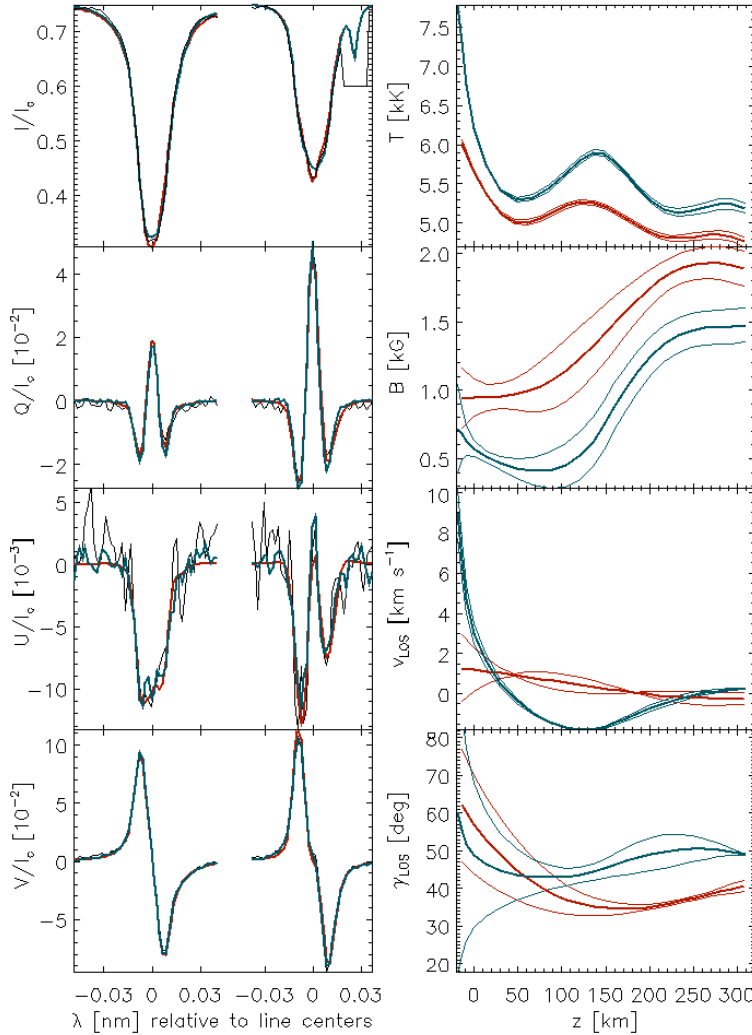
Figure 33: Same as in Fig. 32 but these Stokes profiles were obtained in narrow light bridge in the second area and the blue lines correspond to the stray light from the umbra only.

result, an increase in the field strength with height, remains unaltered. The increase of the umbral component in the stray-light profile also causes a logical increase of the temperature at all heights.

The influence of the stray-light profile on the resulting stratifications of the inclination and/or the line-of-sight velocity seems to be unsystematic. However, in the case of the profiles observed in the narrow parts of the light bridges, similar stratifications of the line-of-sight velocity as those in the broad light bridges are achieved if the stray light contains some portion of the umbral profile (compare the blue stratification of velocity in Fig. 33

79

with the stratifications of this parameter in Fig. 32). The absolute values are different, but closer correspondence can be found with smaller portion of the umbral profile in the stray light. Nevertheless, no conclusions can be based on this finding as these computations were realised only for a few points in the light bridge regions.

The stray-light profile is a very important parameter for the inversion process, but it is impossible even to estimate the right shape of Stokes profiles of the stray light. The examples described above show, that the stray light influences the results mainly in the narrow parts of the light bridges. In the broad part of the first light bridge, small portion of the umbral component in the stray-light profile does not influences the stratifications much (Fig. 32) and higher contamination is improbable, since the inverted Stokes profiles become much worse.

5.3.3 Temperature enhancements and the current densities

The temperature enhancements found in the penumbra are most probably caused by the hot plasma located in the rising flux tubes. However, similar enhancements in the light bridges cannot be related to such structures. In the broad part of LB1, the temperature enhancements create an asymmetric "tunnel" which is seen in Fig. 34. When this structure is followed to the narrower parts of the first light bridge, the "tunnel" becomes narrower and lower. Thus in Fig. 35, the hot plasma at the lowest layers is not as nicely distinguishable from the temperature enhancements that occur at heights around 120 km in the narrow light bridges. The cooler island in the centre of the broad light bridge described in Sect. 5.3.1 is the natural result of the horizontal cuts through the "tunnel" structure.

The only explanation for these temperature enhancements that is suggested here, is related to the Joule heating. The motivation for this concept is based on the geometrical configuration, where the temperature enhancements correspond to the areas with fastest changes of the magnetic field strength and orientation. Such changes produces the increased values of the current density, which is proportional to the Joule heating.

The z component of the current density vector $\mathbf{J}$ can be computed from the inferred values of B_x and B_y:

$$\mu J_z = (\nabla \times B)_z = \frac{\partial B_y}{\partial x} - \frac{\partial B_x}{\partial y}, \qquad (16)$$

where μ is the magnetic permeability.

The 180° ambiguity of the retrieved values of azimuth of the magnetic field lines causes a problem in determining the correct values of current densities. The method suggested by Semel & Skumanich (1998) is used to compute the current densities in both areas. This method separates the contributions to J_z due to the line-of-sight field and plane-of-sky field. The

sign of the first component is unambiguous and the sign of the plane-of-sky component is specified by the user as explained below. In Figs. 47 and 48 (Colour plates) are shown the resulting maps of current densities in the first area for the geometrical heights $z = 50$, 100, 150, and 200 km. The map at $z = 0$ km is not shown , because, as noted before, the errors in azimuth and inclination are too high there. The difference between these figures is that Fig. 47 represents the largest possible current densities allowed by the data and Fig. 48 the smallest ones. Similarly, Figs. 49 and 50 (Colour plates) correspond to the maximal and minimal current densities in the second area respectively. The largest current densities are obtained, if the sign of the plane-of-sky component is the same as the sign of the line-of-sight component. The minimal current densities are obtained with opposite signs of the two components. Note that the polarity of the current density changes in the light bridges between Figs. 47 and 48 and similarly between Figs. 49 and 50. This means, that the ambiguous plane-of-sky contribution to J_z has largest absolute value. The maximal current densities are computed only to estimate the maximal possible Joule heating. On the other hand, the minimal values of J_z represent more realistic configuration of the magnetic field.

Because the full atmosphere is inferred, one should be able to compute the full vector **J**. But this step is non-trivial and will not be taken in this thesis, because both J_x and J_y involve partial derivatives with respect to the height z. But the z scale is inferred by SIR assuming hydrostatic equilibrium stratification, which holds only along field lines. At photospheric heights, the plasma beta (the ratio between the gas and magnetic pressure) is not small and a force-free situation is hardly justifiable. Under such conditions the stratification will deviate from hydrostatic equilibrium making the z scale uncertain. A full derivation of the **J** vector must wait until a model with an assumed MHD configuration is constructed (see the discussion about the Wilson depression in Sect. 2).

Leka (1997) performed the first measurements of electric currents in light bridges. The importance of these currents is that they provide a quantitative measurement of the disruption of the normal topology of the magnetic field in sunspots. She found typical values in a set of bridges ranging from 40 to 100 mA m^{-2}. These currents are larger by as much as a factor of 10 than the normal values found in the umbra. Low-resolution magnetograms also find typical values not higher than a few times 10 mA m^{-2} (Georgoulis & LaBonte 2004). In Table 4 we provide the mean maximal and minimal absolute values in the narrow and broad light bridge along with the average values of current densities in the umbra. Typical errors of these averages are around 5 mA m^{-2}.

The light bridges show the mean values that are very much in the same range as those found by Leka (1997) at heights around 50 km. As is mentioned above, Leka (1997) used the Milne–Eddington inversion which gives

z [km]	Umbra$_{min}$	The current densities in:		Umbra$_{max}$		
		Broad LB$_{min}$	Narrow LB$_{min}$		Broad LB$_{max}$	Narrow LB$_{max}$
50	27	50	62	41	91	122
100	14	32	35	26	76	91
150	8	23	23	19	67	64
200	7	24	14	18	65	37

Table 4: The average current densities reached in the umbra and the broad and narrow light bridge. The minimal and maximal values of J_z allowed by the data are shown.

the results equivalent to the height of approximately $z = 200$ km, where only the maximal possible current densities reach the values comparable with her results. The narrow parts of the light bridges show mean currents that are much stronger than those in the broad light bridge, which is caused by the current-free area in the centre of the broad light bridge. But current peaks are similar in all parts of the analysed light bridges, rarely exceeding values of ± 250 mA m^{-2} and ± 120 mA m^{-2} for the maximal and minimal current densities respectively. These peaks are found more often at the low layers than above $z = 150$ km level (see the locations of strong currents in Figs. 47–50). At high layers, the umbra shows mean currents that are smaller than 20 mA m^{-2}, also in agreement with Leka (1997).

The existence of increased vertical currents (and most likely horizontal, too) suggests that Joule heating may be enhanced in these regions. Using maximal current densities, we computed mean values of Joule heating J_z/σ, where σ is the electric conductivity. We use the approximate expression for determining σ (see Kopecký & Kuklin 1969) $\log \sigma = 15 + 0.93 \log(P_e/P_g)$, where P$_e$ (P$_g$) is the electron (gas) pressure computed by SIR.

The maximal estimate of Joule heating is about 10^{-3} erg s^{-1} cm^{-3}. This energy should contribute to the radiative losses (the divergence of the radiative flux, Priest 1982) in the light bridge region. The magnitude of the radiative losses, which were calculated only from the z-component of the radiative flux, was estimated to be 10^4 erg s^{-1} cm^{-3}. This is seven orders higher than the Joule heating contribution. Thus, at first sight one would not consider Joule heating as linked to the temperature enhancements. However, two considerations must be taken into account in this regard. First of all, the spatial resolution of around 500 km is still inadequate for resolving relevant physical scales, as the presence of a current sheet would require. Second, we only estimate the vertical component of the electric currents. This may be the smallest of all the three components of the current vector. One might
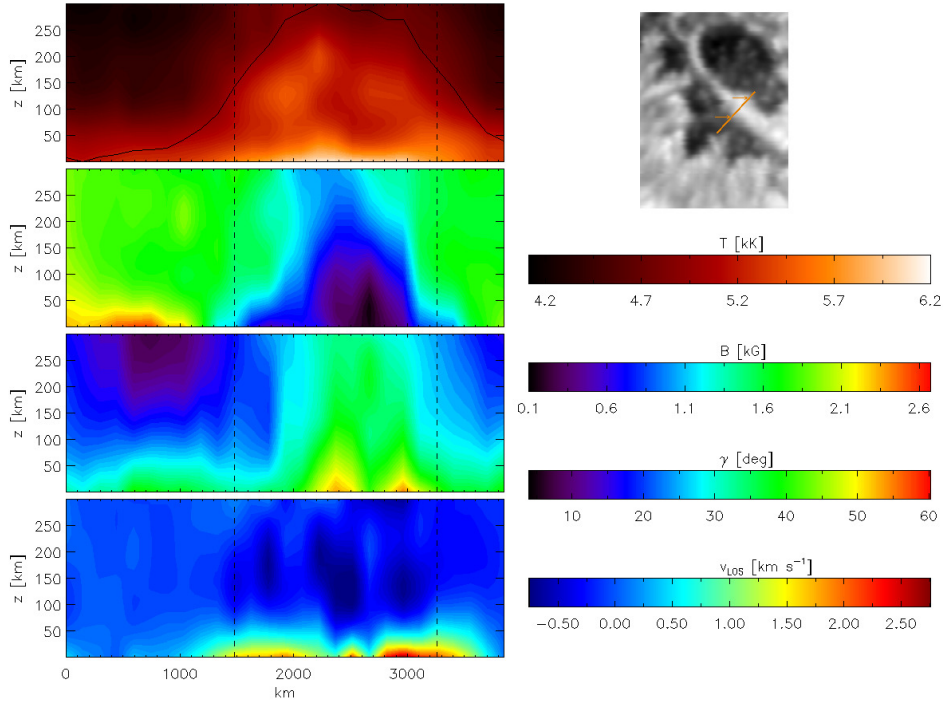
Figure 34: Same as Fig. 30, but the cut is made through the broad part of the first light bridge.

think that the two umbral cores on each side of LB are like close thick vertical flux tubes. These structures are known to have electric currents that lie basically in a plane perpendicular to the axis of the flux tube and distributed either throughout the whole volume or in a thin current sheet (Jahn 1997). Thus the vertical component that we see is most probably a small perturbation of the mostly horizontal current surrounding the flux tubes. In this case we would be heavily underestimating the amount of Joule heating. A proper account of this aspect can only be made using an MHD model of a light bridge that estimates the total electric current from the jumps in the various magnetic parameters found in this work (along the lines of Hamedivafa 2003).

5.3.4 Canopy structure

A magnetic canopy above the light bridges has already been suggested by Leka (1997), although her model of the atmosphere gives no stratification of plasma parameters with height. The basic idea behind introducing the canopy structure above a light bridge is that if the field-free (or weak-field) plasma intrudes into the sunspot umbra, the umbral magnetic field fans out over such a region until it is blocked by the magnetic field of the opposite
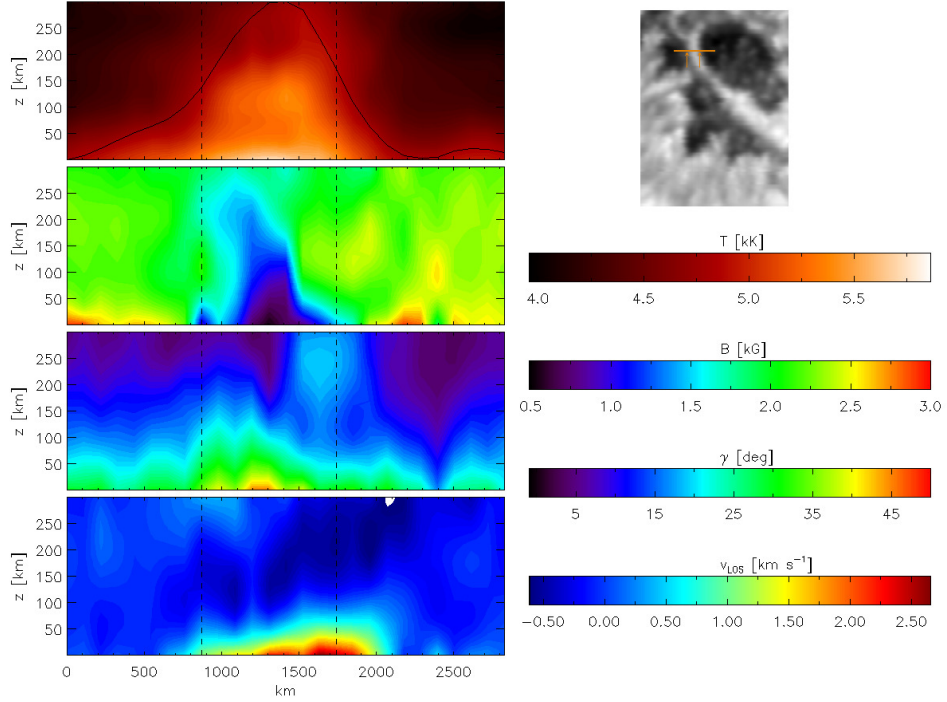
Figure 35: Same as in Fig. 30, but for the narrow part of the first light bridge.

part of the umbra and forced again in the vertical direction. In Fig. 36, the illustration of such a canopy structure is shown.

It is seen in Figs. 39 and 43 that the magnetic field strength is weak in the lowest layers in all parts of the light bridges. The area filled with the weak-field plasma is contracting with height. This means that the broad part of the first light bridge reaches at $z = 250$ km a similar width to the narrow part of this light bridge at $z = 0$ km. The narrowest parts of the light bridges are almost indistinguishable at $z = 250$ km. The same effect can be seen in Figs. 34 and 35, where are shown the vertical cuts through the broad and narrow parts of the first light bridge respectively.

The inclination maps (Figs. 40 and 44) give a similar visual impression to the magnetic field strength maps. Generally, the inclination decreases with height in all parts of the light bridges, and in the narrow parts it acquires values that are similar to those in the surrounding umbra (seen also Figs. 34 and 35).

The arrows in Figs. 39 and 43 indicate the magnetic field azimuth. The case represented in Fig. 36 is a simplistic, 2D scenario that becomes more complex in real sunspots. In particular, the field lines do not necessarily have to meet as nicely as depicted in our 2D picture. This is seen in the
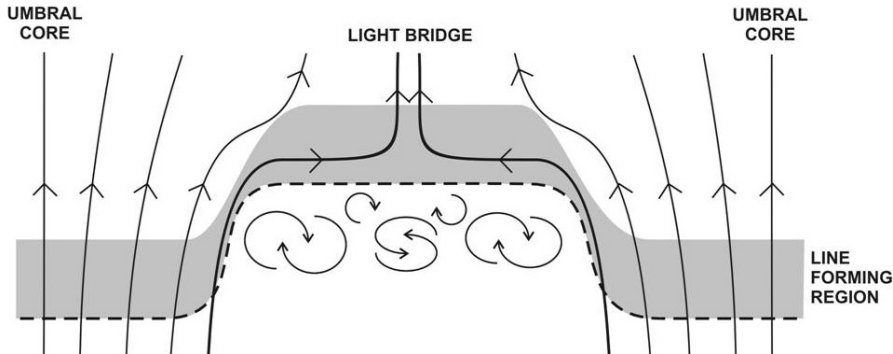
Figure 36: Schematic view of the magnetic canopy above LB.

light bridges studied here. In both cases, we observe the light bridge surrounded by well-defined umbral cores. The distortion introduced into the field azimuth by the light bridges causes the field lines to point toward the light bridge from both surrounding umbras or along the axis of the light bridge at low layers and resembles the situation shown in Fig. 36. This distortion does not disappear with height only at the broad part of the first light bridge. The azimuth directions in narrow light bridges are dominated by the spread of field lines dictated by the dominating umbral core at the highest layers.

The presence of this canopy structure has to create disruptions in the magnetic field and therefore higher values of J_z. The highest values of current densities can be expected at the border between the magnetic field of the umbra and the field-free plasma in the light bridge. This is what one can see in Figs. 47, or 48, where the maximum currents do not coincide with the central part of the broad light bridge, but with its boundaries. The currents are negligible in the centre of this part of LB1 at this spatial resolution and resembles the areas of cool island in the temperature maps (Fig. 38). The areas, where the temperature enhancements are retrieved, spatially correspond to the areas with highest current densities.

The facts presented in the previous paragraphs are in a good agreement with the diagram in Fig. 36, i.e. the vertical cuts through the broad and narrow parts of the first light bridge shown in Figs. 34 and 35 respectively resemble the expected behaviour of the plasma quantities in the proposed canopy structure shown in Fig. 36. We can assume that the only difference between the narrow and broad parts of LBs is the height of emerging field-free plasma. In the narrow parts of LBs, the field-free plasma reaches low layers of the line-formation region. In the case of broad LBs, it penetrates through the line-formation region, and the width of field-free plasma region decreases with height. It is important to note here that by using umbral stray light we found that the magnetic field in the lowest layers of narrow

85

LBs can be decreased significantly.

Similar structure of the light bridge is also described in the article by Spruit & Scharmer (2006), which is concentrated on the structure and origin of the penumbral fine structure. They describe the bright filaments in the penumbra as the tops of field-free gaps and interpret the light bridges as a wider version of the same effect. Our results support this configuration of magnetic field only in the light bridges.

The retrieved stratifications of the line-of-sight velocity are the only problem as they exhibit relatively fast downflows at lowest layers. It was already noted, that the amplitudes are not trustworthy at these layers, but in the case of the canopy structure created by the field-free gas intruding the umbra, one would expect at least slow upflows in the light bridges, i.e. the change of sign of the obtained values of the line-of-sight velocity at the lowest layers. Such upflows are retrieved on average only at the geometrical height $z = 100$ km and above and also in the maps of velocity retrieved from the shifts of the Stokes I profiles of the iron lines.

5.3.5 Conclusions

Two strong light bridges in a complex irregular sunspot were observed spectropolarimetrically. For the first time, the stratification with height of the plasma parameters is presented. The changes in temperature, magnetic field strength, and inclination in the light bridges agree well with previous studies of these phenomena. The line-of-sight velocities retrieved by the SIR code in the light bridges are comparable with previous studies only at high layers, where they resemble the maps of velocities obtained from the shifts of the Stokes I profiles.

The magnitudes of maximal temperature in the centre of the broad light bridge at the geometrical height $z = 0$ km are comparable with the photospheric temperatures of the quiet sun. The local enhancements in the temperature stratification are found in about 60% of the points inside LBs. This can be seen in Fig. 32 around $z = 200$ km and in Fig. 33 around $z = 120$ km. The spatial and height distribution of these enhancements is shown in Fig. 34. Taking into account the very small uncertainties in temperature calculated by the inversion code and the magnitudes of these enhancements, we believe that these enhancements are not artifacts of the inversion method but real phenomena.

The retrieved results confirm not only the lower magnetic field strength in the light bridges, but show strong gradients with height too. The magnetic field strength in the umbra decreases with height (1 G km^{-1}), while in the light bridges it rapidly increases with gradients reaching -4.7 G km^{-1}. The field is very weak especially in the broad light bridge at $z = 0$ km, but is nearly equal to that of the umbra at $z = 250$ km in the narrow light bridges. Also the inclination shows considerable changes with height. The magnetic

86

field is very inclined at low levels (especially in broad LB1), but at high layers it has a similar inclination to the one in the surrounding umbra (especially for the narrow light bridges). The resulting stratification of a magnetic field vector with height indicates the presence of a magnetic canopy above the field-free or weak-field plasma that forms both light bridges. We stress that this work has indeed found, for the first time, field-free regions in the broad part of the first light bridge and an evidence of similar conditions in narrower light bridges.

The light bridges are regions with enhanced vertical electric currents. We have derived the highest currents found in non-δ spots (up to 150 mA m^{-2} in maps of the minimal current densities). This is most probably due to the relatively high spatial resolution achieved by our observations. But even these currents cannot account (through Joule heating) for the temperature enhancements found by the inversion code. As pointed out before, better resolution and an estimate of the full $\mathbf{J}$ vector is fundamental for resolving this issue. This is important in the context of the ubiquitous brightness enhancements observed in the chromosphere by TRACE (Berger & Berdyugina 2003). These authors found that the light bridges have chromospheres that are magnetically heated as they are constantly pervaded by brightenings in the 1600 Å images. This band forms in a temperature range from 4000 K to 20 000 K, that is, from the upper photosphere to the transition region between the chromosphere and corona. Thus our temperature enhancements may be related to these chromospheric brightenings. Their physical origin can be linked to the canopy topology also found in this work. As explained above, this topology can be very complex in 3D, harbouring field lines that meet at large angles, where a reconnection can occur.

The line-of-sight velocity in the light bridges exhibits both downflows and upflows at all heights. Strong downflows and average values of the velocity retrieved at $z = 0$ km infirm the reliability of this parameter at this height. Nonetheless, evidences for the convective motions in the broad part of the light bridge are found on the basis of velocities retrieved by the SIR code at high layers and also of velocities determined from the shifts of the Stokes I profiles. It is also interesting to note that convective motions in the light bridges are very dynamic, so one can see the boundaries between the umbral cores and light bridges in constant change (Berger & Berdyugina 2003). Accordingly, the canopy structure above is subject to constant readjustment, which in turn can form the required heating source. From an observational point of view, the combination of uninterrupted chromospheric TRACE observations and high-spatial resolution spectropolarimetric data from the Japanese-led solar-B mission (launch 2006) represents our best opportunity to gain further insight into this problem.

6   Summary

The irregular leading sunspot in the active region NOAA 8990 was observed with the La Palma Stokes Polarimeter attached to the spectrograph of the 0.5 m Swedish Vacuum Solar Telescope. The resulting spatial resolution around 500 km is one of the best available nowadays for the full-Stokes polarimetry. Two areas containing the umbral cores divided by the light bridges and surrounded by the penumbra were scanned in the magnetically sensitive lines Fe I 630.15 nm and Fe I 630.25 nm.

The Stokes Inversion based on Response functions technique was used on these data. All four Stokes profiles were inverted, yielding three-dimensional information about the plasma quantities in these areas. We have confirmed that the results obtained by the inversion code SIR are trustworthy in a broad range of heights.

The resulting stratifications of the plasma parameters are almost independent on the initial model of atmosphere and the noise does not influence the retrieved model of atmosphere significantly. However, the resulting models of atmosphere are dependent on the stray-light profile, which is changing from pixel to pixel and it is impossible to determine it properly. The results are most dependent on the stray-light profile in the narrow parts of the light bridges, but the main finding discovered in these areas remains unaltered.

No surprising facts are retrieved in the parts of the irregular umbras analysed here. The darkest parts of the umbras correspond to the most intense magnetic field, which is the most vertical there. Although the obtained values of the line-of-sight velocity are reaching maximal absolute values around 200 m s^{-1} at the unit continuum optical depth (the geometrical height $z = 0$ km), the umbra can be still considered to be at rest, since these values are comparable with the uncertainties of this plasma parameter at this height.

The observation of only incomplete parts of the penumbra disables the comparison of the absolute values of plasma parameters, as they are heavily dependent on the position in the penumbra. However, the general results confirm the previous findings of the penumbral structure. The magnetic field becomes weaker and more horizontal with increasing distance from the umbra-penumbra boundary. The line-of-sight velocities are restricted to low layers of the analysed region of heights and the absolute values of the velocities are increasing with increasing distance from the umbra.

The general results suggest the existence of the unresolved fine structure in the penumbra, since the obtained maps of plasma parameters exhibit spine/interspine corrugation which is only loosely correlated with the filamentary structure observed in the direct white-light image. Our results support the uncombed configuration of the magnetic field in the penumbra, which was suggested by Solanki & Montavon (1993) and Martínez Pillet (2000). This configuration consists of the background field (stronger and

more vertical) interlaced with the flux tubes (weaker and horizontal magnetic field). As the expected diameters of the rising flux tubes are around 100 km, they are spatially unresolved. However, the found spine/interspine corrugation can be explained by the various filling factors of the flux tubes in the resolution elements of our observations. The regions where either the background or the flux tube component prevails are distinguishable in maps of the resulting plasma parameters. Significant portion of the flux tube component in the resolution element results into weaker magnetic field there and the inclination is dependent on the continuum brightness of this pixel, i.e. more brighter areas have more vertical field. The prevailing background component is characterised by the strong and the most vertical magnetic field observed in the penumbra. These results together with the localisation of the temperature enhancements strongly support the model of the rising flux tubes computed by Schlichenmaier et al. (1998).

The retrieved values of the line-of-sight velocities do not reach the maxima at heights, where the flux tubes are expected as suggests the empirical model by Martínez Pillet (2000). However, these maxima of the Evershed flow spatially correspond to the location of the horizontal parts of flux tubes. In places of the bright grains, the upflows are observed even in the limbward parts of the penumbra (in agreement with Schlichenmaier et al. 1998).

In this thesis, the stratifications of the plasma parameters in the light bridges are analysed for the first time. It is shown that the known facts as the increased temperature, lower magnetic field strength, and higher inclination in the light bridges are dependent not only on the width of the light bridge, but also on the height in the photosphere.

The temperature enhancements are found in the light bridges, with magnitudes around 200 km. The height of formation of these enhancements is dependent on the width of the light bridge and on the position in the light bridge creating a "tunnel" like structure in the broad part of the first light bridge. We try to interpret these enhancements as the consequence of the Joule heating, because they spatially correspond to the areas between the magnetic field of the umbra and the field-free plasma in the light bridge, where highest current densities can be expected. However, even the maximal possible values of the current densities (and proportionally of the Joule heating) are too low to explain the temperature enhancements. However, the effect of Joule heating could be larger if also the x- and y-component could be taken into account.

As mentioned above, the decrease of the magnetic field strength in comparison with surrounding umbra is heavily dependent on the height in the photosphere. The magnetic field strength in the umbra decreases slowly with height, while in the light bridges it rapidly increases. The field is very weak especially in the broad light bridge at the unit continuum optical depth, but it is nearly equal to that of the umbra at the highest layers in the narrow light bridges. Also the inclination shows considerable changes with height.

89

The magnetic field is very inclined at low levels, but at high layers it has a similar inclination to that in the surrounding umbra (especially for the narrow light bridges). The resulting stratifications of the strength and orientation of the magnetic field indicate the presence of a magnetic canopy above the field-free or weak-field plasma that forms both light bridges. Similar signatures of the magnetic canopy structure were found above umbral dots by Socas-Navarro et al. (2004).

The line-of-sight velocity in the light bridges exhibits both downflows and upflows at all heights. Evidences for the convective motions in the broad part of the light bridge are found on the basis of velocities retrieved by the SIR code at high layers and also of velocities determined from the shifts of the Stokes I profiles.

References

Barklem, P. S., Anstee, S. D., & O'Mara, B. J. 1998, Publications of the Astronomical Society of Australia, 15, 336

Beckers, J. M. & Schröter, E. H. 1969, Sol. Phys., 10, 384

Beckers, J. M. & Schröter, E. H. 1968, Sol. Phys., 4, 303

Bello González, N., Okunev, O. V., Domínguez Cerdeña, I., Kneer, F., & Puschmann, K. G. 2005, A&A, 434, 317

Bellot Rubio, L. R. 1999, in A user quide to SIR

Bellot Rubio, L. R., Balthasar, H., & Collados, M. 2004, A&A, 427, 319

Berger, T. E. & Berdyugina, S. V. 2003, ApJl, 589, L117

Börner, P. & Kneer, F. 1992, A&A, 259, 307

Borrero, J. M., Solanki, S. K., Bellot Rubio, L. R., Lagg, A., & Mathew, S. K. 2004, A&A, 422, 1093

Buurman, J. 1973, A&A, 29, 329

Chen, H.-R., Chou, D.-Y., & TON Team. 1997, ApJ, 490, 452

Choudhuri, A. R. 1986, ApJ, 302, 809

Choudhuri, A. R. 1992, in NATO ASIC Proc. 375: Sunspots. Theory and Observations, 243–257

Cowling, T. G. 1957, Magnetohydrodynamics (Interscience, New York)

Degenhardt, D. 1991, A&A, 248, 637

Degenhardt, D. & Lites, B. W. 1993a, ApJ, 404, 383

Degenhardt, D. & Lites, B. W. 1993b, ApJ, 416, 875

del Toro Iniesta, J. C. 2003, Introduction to Spectropolarimetry (Introduction to Spectropolarimetry, by Jose Carlos del Toro Iniesta, pp. 244. ISBN 0521818273. Cambridge, UK: Cambridge University Press, April 2003.)

Dere, K. P., Schmieder, B., & Alissandrakis, C. E. 1990, A&A, 233, 207

Evershed, J. 1909, MNRAS, 69, 454

Georgakilas, A. A. & Christopoulou, E. B. 2003, ApJ, 584, 509

Georgoulis, M. K. & LaBonte, B. J. 2004, ApJ, 615, 1029

Gingerich, O., Noyes, R. W., Kalkofen, W., & Cuny, Y. 1971, Sol. Phys., 18, 347

Hale, G. E. 1908, ApJ, 28, 315

Hamedivafa, H. 2003, A&A, 407, 761

Hirzberger, J., Bonet, J. A., Sobotka, M., Vázquez, M., & Hanslmeier, A. 2002, A&A, 383, 275

Hirzberger, J., Stangl, S., Gersin, K., et al. 2005, A&A, 442, 1079

Jahn, K. 1989, A&A, 222, 264

Jahn, K. 1992, in NATO ASIC Proc. 375: Sunspots. Theory and Observations, 139

Jahn, K. 1997, in ASP Conf. Ser. 118: 1st Advances in Solar Physics Euroconference. Advances in Physics of Sunspots, 122

Jahn, K. & Schmidt, H. U. 1994, A&A, 290, 295

Jurčák, J., Sobotka, M., & Martínez-Pillet, V. 2003, in ESA SP-535: Solar Variability as an Input to the Earth's Environment, 109–112

Jurčák, J., Sobotka, M., & Martinez Pillet, V. 2006, A&A, in press

Kjeldseth-Moe, O. & Maltby, P. 1969, Sol. Phys., 8, 275

Kneer, F. 1973, Sol. Phys., 28, 361

Kopecký, M. & Kuklin, G. V. 1969, Sol. Phys., 6, 241

Koza, J. 2003, the doctoral thesis Modelovanie časového vývoja slnečnej fotosféry

Landi Degl'Innocenti, E. & Landi Degl'Innocenti, M. 1985, Sol. Phys., 97, 239

Langhans, K., Scharmer, G. B., Kiselman, D., Löfdahl, M. G., & Berger, T. E. 2005, A&A, 436, 1087

Leka, K. D. 1997, ApJ, 484, 900

Lites, B. W., Bida, T. A., Johannesson, A., & Scharmer, G. B. 1991, ApJ, 373, 683

Lites, B. W., Elmore, D. F., Seagraves, P., & Skumanich, A. P. 1993, ApJ, 418, 928

Lites, B. W., Skumanich, A., & Scharmer, G. B. 1990, ApJ, 355, 329

Martens, P. C. H., Hurlburt, N. E., Title, A. M., & Acton, L. W. 1996, ApJ, 463, 372

Martínez Pillet, V. 2000, A&A, 361, 734

Martínez Pillet, V., Collados, M., Sánchez Almeida, J., et al. 1999, in ASP Conf. Ser. 183: High Resolution Solar Physics: Theory, Observations, and Techniques, 264

Martínez Pillet, V., Trujillo Bueno, J., & Collados, M. 2001, in ASP Conf. Ser. 236: Advanced Solar Polarimetry – Theory, Observation, and Instrumentation, 133

Martínez Pillet, V. & Vazquez, M. 1993, A&A, 270, 494

Meyer, F. & Schmidt, H. U. 1968, Z. Ang. Math. Mech., 48, T218

Murphy, G. A. 1990, NCAR Cooperative Thesis No. 124

Nave, G., Johansson, S., Learner, R. C. M., Thorne, A. P., & Brault, J. W. 1994, ApJS, 94, 221

Neukirch, T. & Martens, P. C. H. 1998, A&A, 332, 1075

Nordlund, A. & Stein, R. 2005, in preparation

Osherovich, V. A. 1982, Sol. Phys., 77, 63

Pahlke, K.-D. & Wiehr, E. 1990, A&A, 228, 246

Parker, E. N. 1975, Sol. Phys., 40, 291

Parker, E. N. 1979, ApJ, 234, 333

Pizzo, V. J. 1986, ApJ, 302, 785

Priest, E. R. 1982, Solar magneto-hydrodynamics (Dordrecht, Holland ; Boston : D. Reidel Pub. Co. ; Hingham,), 74P

Rimmele, T. R. 1994, A&A, 290, 972

Rimmele, T. R. 1995a, A&A, 298, 260

Rimmele, T. R. 1995b, ApJ, 445, 511

Rimmele, T. R. 1997, ApJ, 490, 458

Rimmele, T. R. 2004, ApJ, 604, 906

Rüedi, I., Solanki, S. K., & Livingston, W. 1995, A&A, 302, 543

Ruiz Cobo, B. 1998, Ap&SS, 263, 331

93

Ruiz Cobo, B. & del Toro Iniesta, J. C. 1992, ApJ, 398, 375

Ruiz Cobo, B. & del Toro Iniesta, J. C. 1994, A&A, 283, 129

Sanchez Almeida, J. & Lites, B. W. 1992, ApJ, 398, 359

Sánchez Cuberes, M., Puschmann, K. G., & Wiehr, E. 2005, A&A, 440, 345

Scharmer, G. B., Gudiksen, B. V., Kiselman, D., Löfdahl, M. G., & Rouppe
   van der Voort, L. H. M. 2002, Nature, 420, 151

Scharmer, G. B., Pettersson, L., Brown, D. S., & Rehn, J. 1985, Appl. Opt.,
   24, 2558

Schatzmann, E. 1965, in IAU Symp. 22: Stellar and Solar Magnetic Fields,
   337

Schlichenmaier, R., Jahn, K., & Schmidt, H. U. 1998, A&A, 337, 897

Schlichenmaier, R. & Schmidt, W. 2000, A&A, 358, 1122

Schlüter, A. & Temesváry, S. 1958, in IAU Symp. 6: Electromagnetic Phe-
   nomena in Cosmical Physics, 263

Schmidt, H. U. & Wegmann, R. 1983, in Dynamical Problems in Mathe-
   matical Physics, 137

Schmidt, W. & Balthasar, H. 1994, A&A, 283, 241

Schmidt, W., Hofmann, A., Balthasar, H., Tarbell, T. D., & Frank, Z. A.
   1992, A&A, 264, L27

Schmidt, W. & Schlichenmaier, R. 2000, A&A, 364, 829

Semel, M. & Skumanich, A. 1998, A&A, 331, 383

Shine, R. A., Title, A. M., Tarbell, T. D., et al. 1994, ApJ, 430, 413

Simon, G. W. & Weiss, N. O. 1970, Sol. Phys., 13, 85

Sobotka, M. 1989, Sol. Phys., 124, 37

Sobotka, M. 1997, in ASP Conf. Ser. 118: 1st Advances in Solar Physics
   Euroconference. Advances in Physics of Sunspots, 155

Sobotka, M. 2003, Astronomische Nachrichten, 324, 369

Sobotka, M., Brandt, P. N., & Simon, G. W. 1999, A&A, 348, 621

Socas-Navarro, H., Pillet, V. M., Sobotka, M., & Vázquez, M. 2004, ApJ,
   614, 448

Solanki, S. K. 2003, A&A Rev., 11, 153

Solanki, S. K. & Montavon, C. A. P. 1993, A&A, 275, 283

Solanki, S. K., Rueedi, I., & Livingston, W. 1992, A&A, 263, 339

Solanki, S. K. & Schmidt, H. U. 1993, A&A, 267, 287

Spruit, H. C. 1981, in The Physics of Sunspots, 98–103

Spruit, H. C. & Scharmer, G. B. 2006, A&A, 447, 343

Stanchfield, D. C. H., Thomas, J. H., & Lites, B. W. 1997, ApJ, 477, 485

Steiner, O., Pneuman, G. W., & Stenflo, J. O. 1986, A&A, 170, 126

Thevenin, F. 1989, A&AS, 77, 137

Thevenin, F. 1990, A&AS, 82, 179

Title, A. M., Frank, Z. A., Shine, R. A., et al. 1993, ApJ, 403, 780

Tritschler, A., Schlichenmaier, R., Bellot Rubio, L. R., et al. 2004, A&A, 415, 717

Tritschler, A. & Schmidt, W. 1997, A&A, 321, 643

Wegmann, R. 1981, in Numerical Treatment of Free Boundary Value Problems, 335

Weiss, N. O., Brownjohn, D. P., Hurlburt, N. E., & Proctor, M. R. E. 1990, Monthly Notices Royal Astron. Soc., 245, 434

Wentzel, D. G. 1992, ApJ, 388, 211

Westendorp Plaza, C., del Toro Iniesta, J. C., Ruiz Cobo, B., et al. 2001a, ApJ, 547, 1130

Westendorp Plaza, C., del Toro Iniesta, J. C., Ruiz Cobo, B., & Pillet, V. M. 2001b, ApJ, 547, 1148

Wiehr, E. 2000, Sol. Phys., 197, 227

Wiehr, E., Knoelker, M., Grosser, H., & Stellmacher, G. 1986, A&A, 155, 402

Wiehr, E., Koch, A., Knoelker, M., Kueveler, G., & Stellmacher, G. 1984, A&A, 140, 352

Wittmann, A. 1971, Sol. Phys., 20, 365

Zhao, J., Kosovichev, A. G., & Duvall, T. L. 2001, ApJ, 557, 384
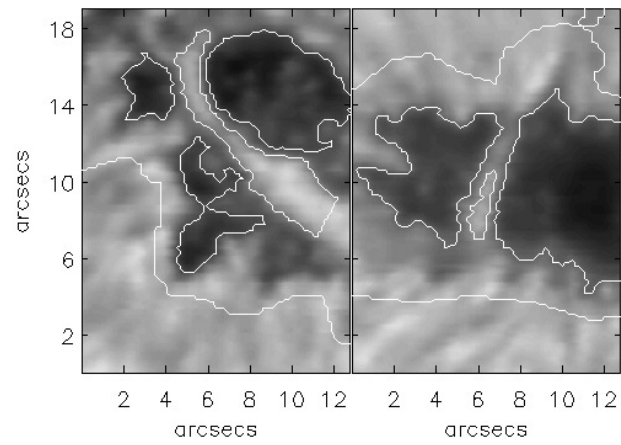
Colour plates

Figure 37: Continuum image with contours, which correspond to the umbral, penumbral, and light bridge boundaries. Similar to Fig. 9, but with the same proportions as the following figures with resulting plasma parameters.
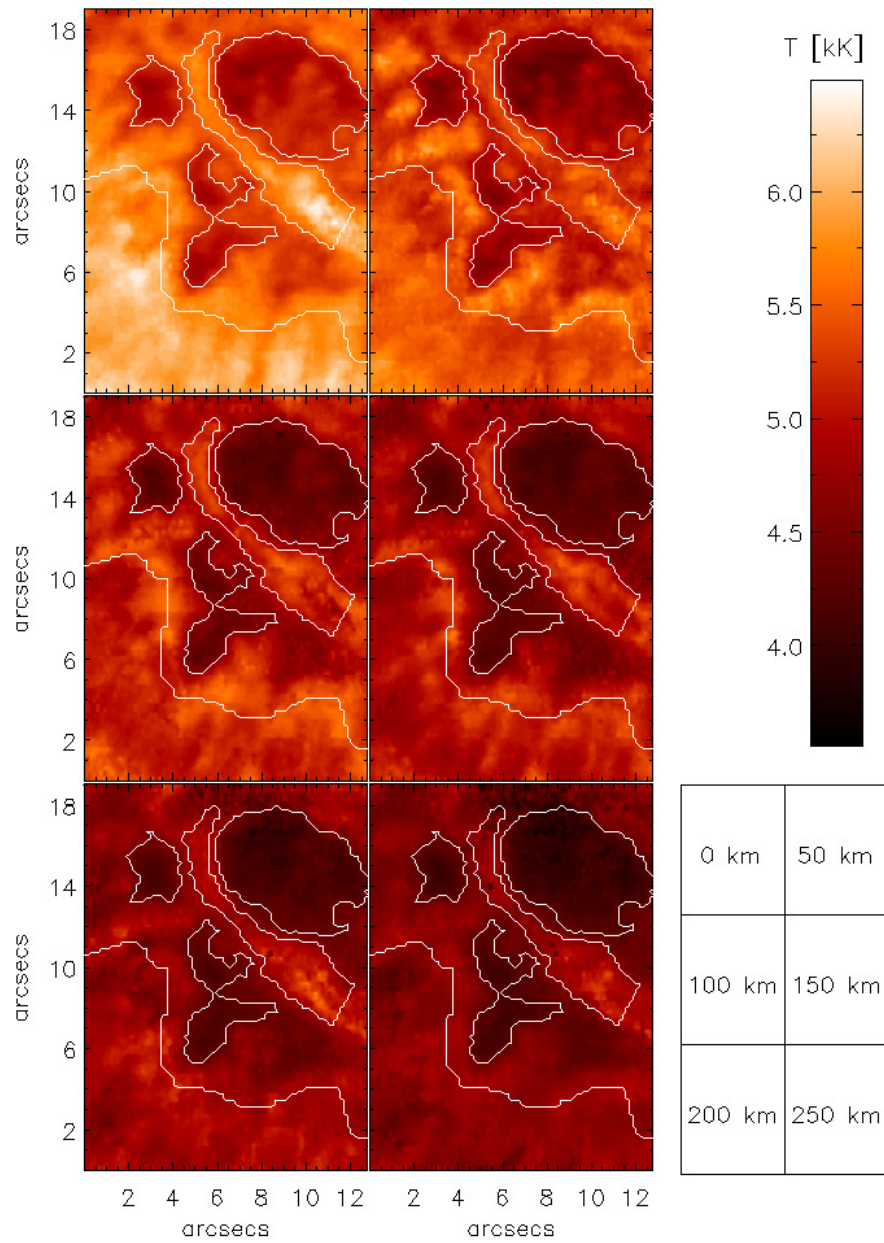
Figure 38: The resulting maps of temperature for area 1. The white contours correspond to the umbral, penumbral, and light bridge boundaries. The heights given in km are the geometrical heights above the unit continuum optical depth.
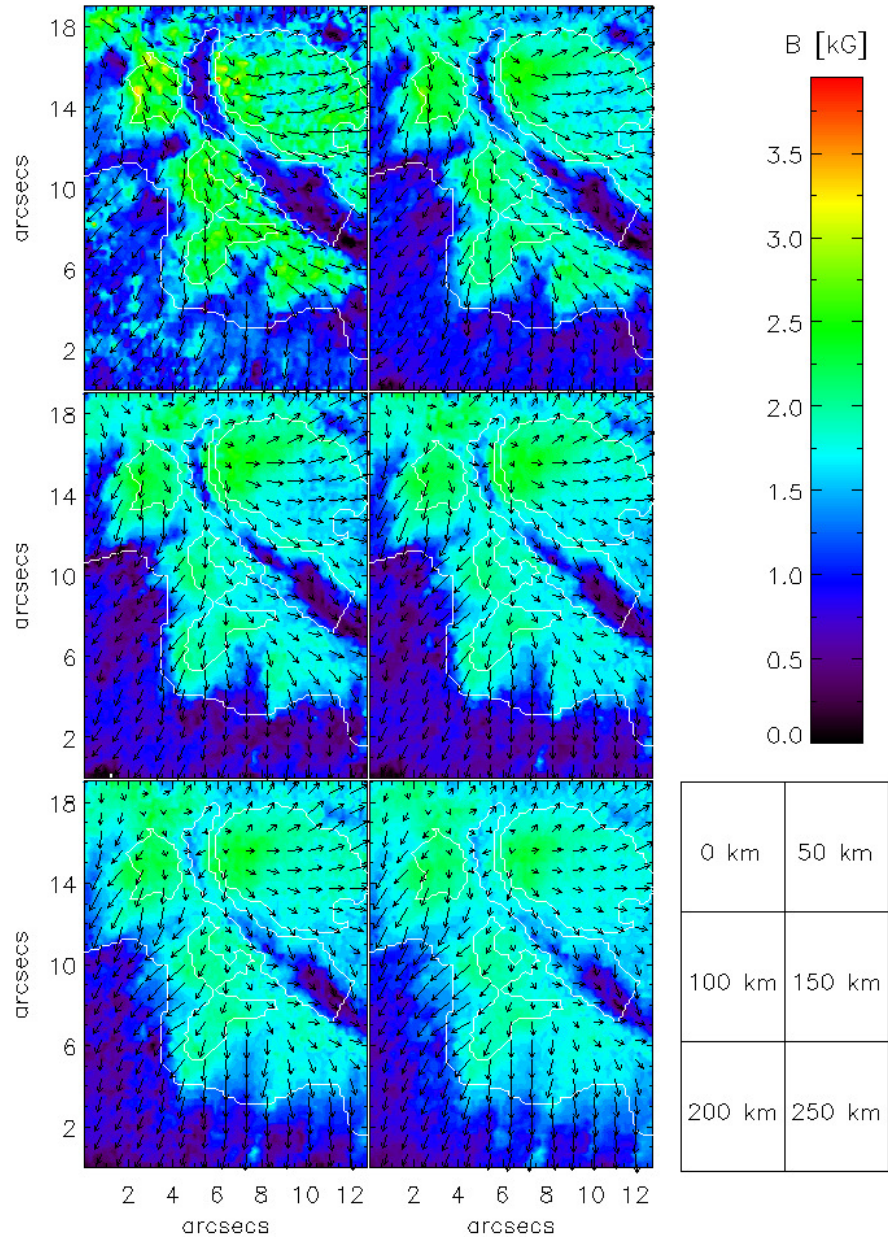
Figure 39: The resulting maps of magnetic field strength for area 1, where the black arrows indicate the projection of **B** to the solar surface. Otherwise same as in Fig. 38.
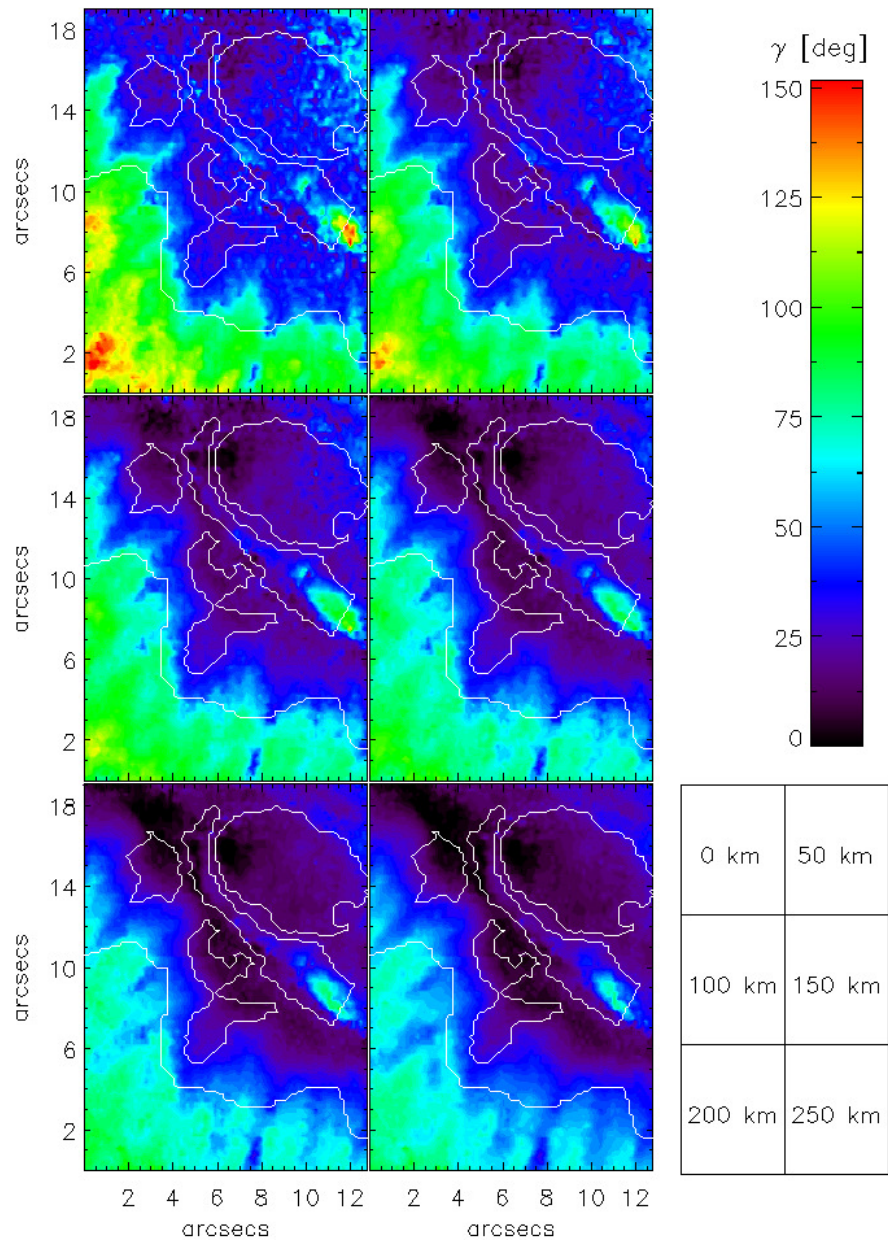
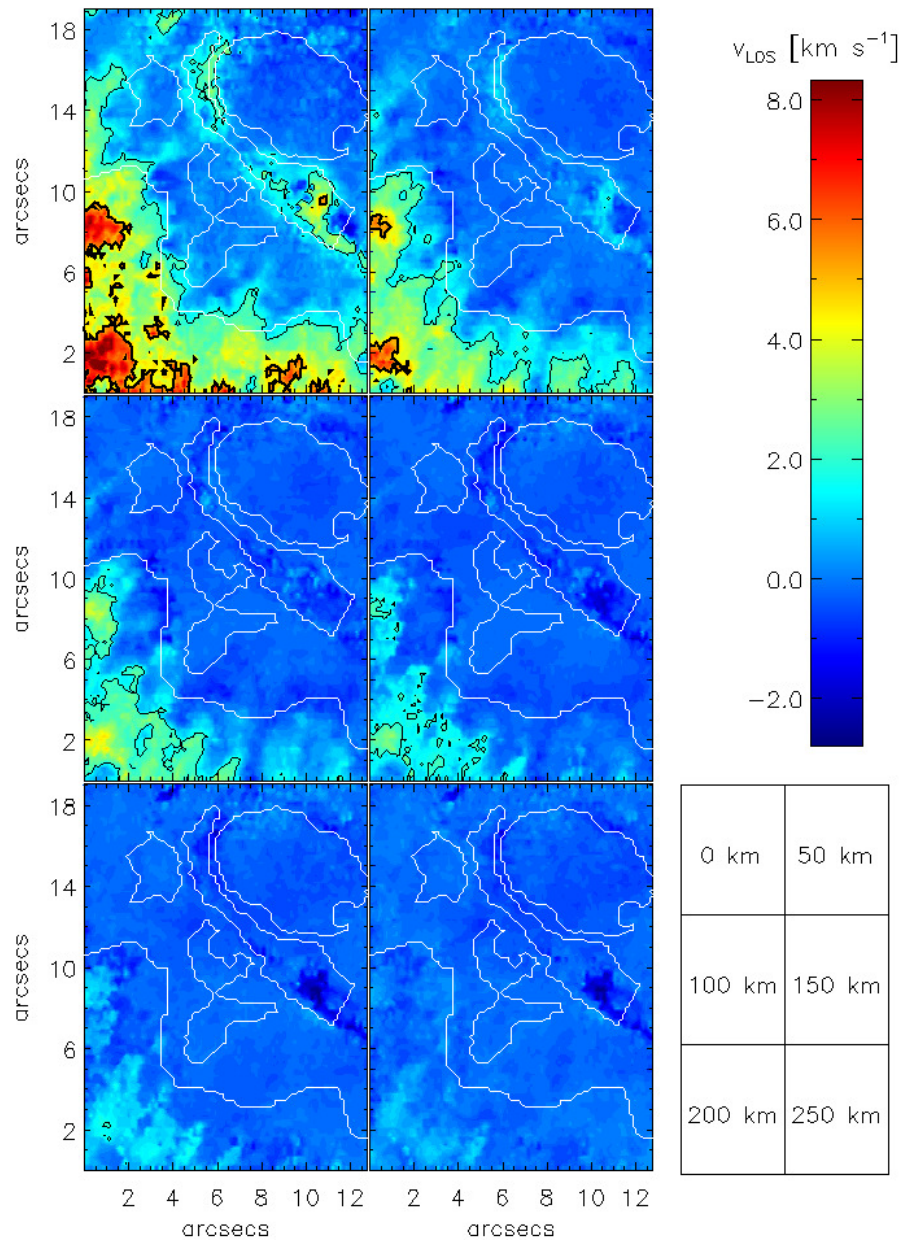Figure 40: The resulting maps of inclination for area 1. Otherwise same as in Fig. 38.

Figure 41: The resulting maps of line-of-sight velocity for area 1. The thin black contours enclose the areas with downflows faster than 2 km s^{-1} and the thick black lines the areas with downflows stronger than 5 km s^{-1}. Otherwise same as in Fig. 38.
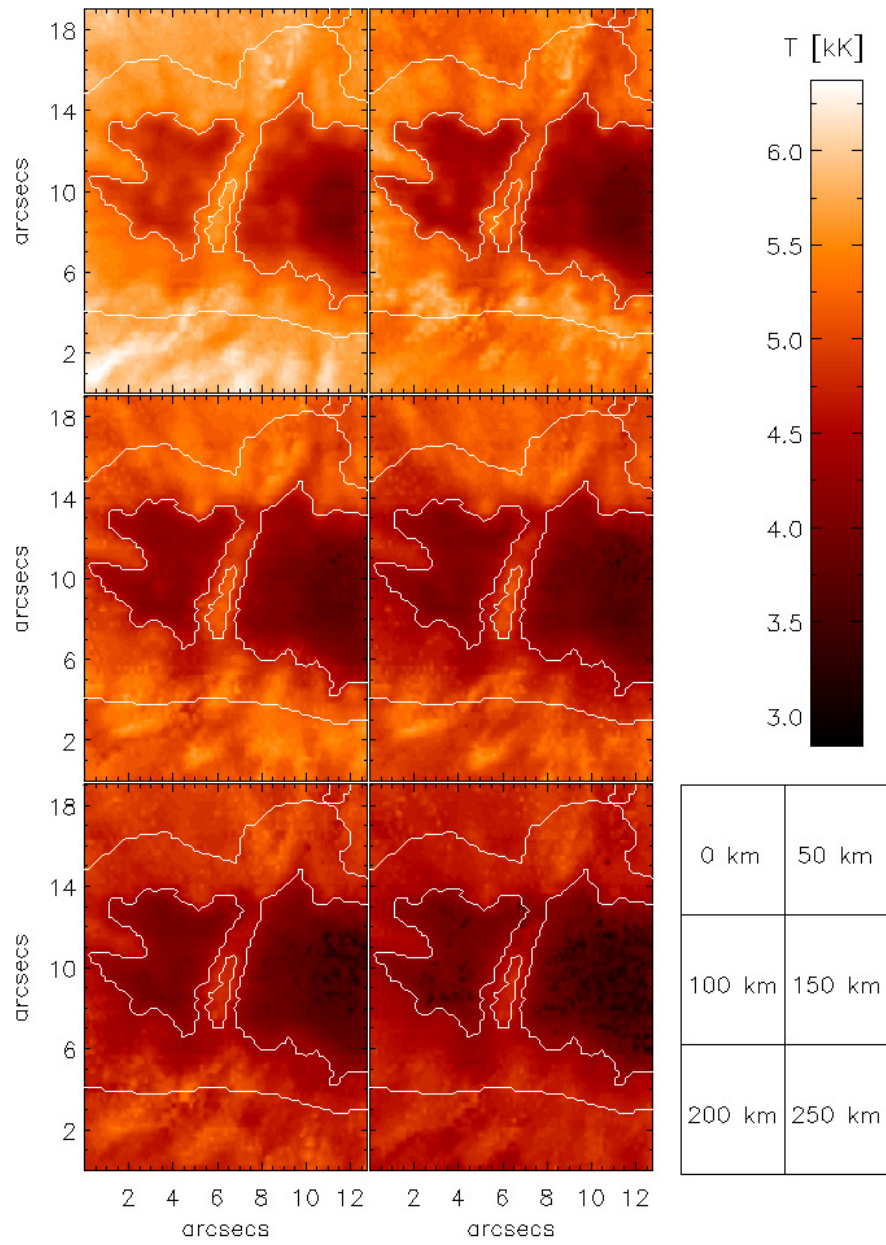
Figure 42: Same as Fig. 38, but for area 2.